UNIVERSITÀ DEGLI STUDI DI FIRENZE

DIPARTIMENTO DI FISICA

DOTTORATO DI RICERCA IN FISICA

Measurement of W pair production cross section with the L3 detector at LEP2

Tesi di Dottorato di Ricerca in Fisica di

Alessandro Buffini

Relatore	Dott.	Raffaello D'Alessandro
Relatore esterno	Prof.	Guy Coignet

XI Ciclo di Dottorato

Coordinatore Prof. Valerio Tognetti

Firenze, 30 Dicembre 1998 Anno Accademico 1997/1998

Contents

Introduction

Since 1989 the electron-positron storage ring LEP[1] has been operational at CERN. It is located near Geneva and it is, at present, the largest electron-positron collider in the world.

The main reason for building this collider was to test and verify the predictions of the present theory of electroweak interactions proposed in the sixties by S.L. Glashow, A. Salam and S. Weinberg [1], (Standard Model). In this framework matter consists of fermions with bosons mediating their interactions; in this model the electromagnetic force is carried by a massless photon while the weak interaction is transmitted via three massive gauge bosons which are the neutral Z and the charged W^+ and W^- bosons.

This theory is based on a underlying local gauge symmetry and a neutral particle, the Higgs boson, is included in order to break this symmetry spontaneously and give masses to the $W^\pm$ and Z gauge bosons and to the fermions.

The predictions of the Z and $W^\pm$ bosons were experimentally confirmed first by the discovery of the neutral currents in 1973 by the Gargamelle collaboration [2, 3], then by the direct observation of the $W^\pm$ and Z particles in 1983 by the UA1 and UA2 collaborations [4, 5] at the proton-antiproton collider $Sp\bar{p}S$ at CERN.

From 1989 till 1995 LEP was set at a centre of mass energy of about 91 GeV, which corresponds to the mass of the Z, and collected about four millions hadronic decays of the Z boson for each of the four experiments[2] located at LEP. This has allowed a very precise determination of the Z boson properties such as its mass and decay widths, as well as several high precision tests of the Standard Model.

After a short intermediate phase at a centre of mass energy between 130 and 140 GeV, LEP energy was gradually increased beyond the W boson pair production threshold, thus allowing the study of the properties of this boson in detail (this second phase is called LEP2 to distinguish it from the first phase called LEP1).

The properties of the W boson are the subject of this thesis, in particular the W pair production cross section in e^+e^- annihilation has been measured using the data collected by the L3 experiment in 1997 at a centre of mass energy of 183 GeV.

Moreover, during the work for this thesis, a new method of analysis has been studied and developed in order to increase the selection efficiency and so reduce the statistical error of a cross section measurement.

The experimental setup used for this measurement, that is the LEP collider and the

---

[1] **L**arge **E**lectron **P**ositron collider.

[2] ALEPH, DELPHI, L3, OPAL.

L3 detector, will be described in chapter 1. In the second chapter I will describe the main physical processes that occur at LEP2 with particular attention to the W pair production; some theoretical aspects will also be treated here. Chapter 3 will be devoted to a study of the performance of the reconstruction program especially in what concerns particle identification algorithms. A new method of analysis developed in order to decrease the statistical error in a cross section measurement will be described in detail in chapter 4. The selections of all possible final states of the W pair decays and the cross sections measurement are presented in chapter 5. Finally chapter 6 contains the study of possible causes of systematic error regarding the cross section measurements and the conclusions.

In this thesis, as it is common in particle physics, I will use the convention $\hbar = c = 1$ to define the system of units; energies, masses and momenta are therefore measured in electron volts (1 eV = $1.602 \cdot 10^{-19}$ J).

Chapter 1

The LEP storage ring and the L3 experiment

1.1 LEP

With its 27 Km of circumference, LEP is the world's largest circular e^+e^- collider; it is located near Geneva on the French-Swiss border (fig. 1.1).

Electrons and positrons are delivered to LEP by the system of accelerators shown in fig. 1.2.

Electrons and positrons are produced and accumulated in the LPI (Lepton Pre-Injector) complex consisting of a linear accelerator (LIL, 600 MeV) and the electron-positron accumulator (EPA). The beams are then transferred to the PS (Proton Synchrotron), where their energy is increased up to 3.5 GeV. The final stage of pre-acceleration takes place in the SPS (Super Proton Synchrotron), which also delivers protons for the fixed target experiments at CERN.

The electrons and positrons are then injected into LEP with an energy of 23 GeV, each type grouped in eight equidistant bunches ($\sim$10 μm height, $\sim$1 cm length and $\sim$150 μm width) circulating in opposite directions and with about $5 \cdot 10^{11}$ particles per bunch. Once injected they are then accelerated to the set value of the machine (i.e. 90 GeV).

LEP consists of eight straight and eight curved sections which are symmetrically arranged in the shape of an octagon. Inside four of the eight straight sections the beams, once they have reached their maximum energy, are brought to collision every 22μs in the points where the four experiments ALEPH [6], DELPHI [7], L3 [8], OPAL [9] are located.

In the curved sections of the ring 3368 dipole magnets are installed in order to bend the beams and keep the electrons and positrons on their orbit. Due to the bending in these sections the particles suffer from synchrotron radiation; the radiated energy depends on the particle energy E and the radius of curvature R as E^4/R; this is the reason of the huge dimensions of the collider. Radio frequency (RF) cavities, installed near the L3 and OPAL experiment, supply the energy for the final acceleration of the beams and for the compensation of the energy loss due to the synchrotron radiation.

Until the final energy is reached the electron and positron beams are separated in the interaction points by electrostatic separators, while a system of quadrupole magnets allows focusing and transversal adjustment of the beams during the collisions.

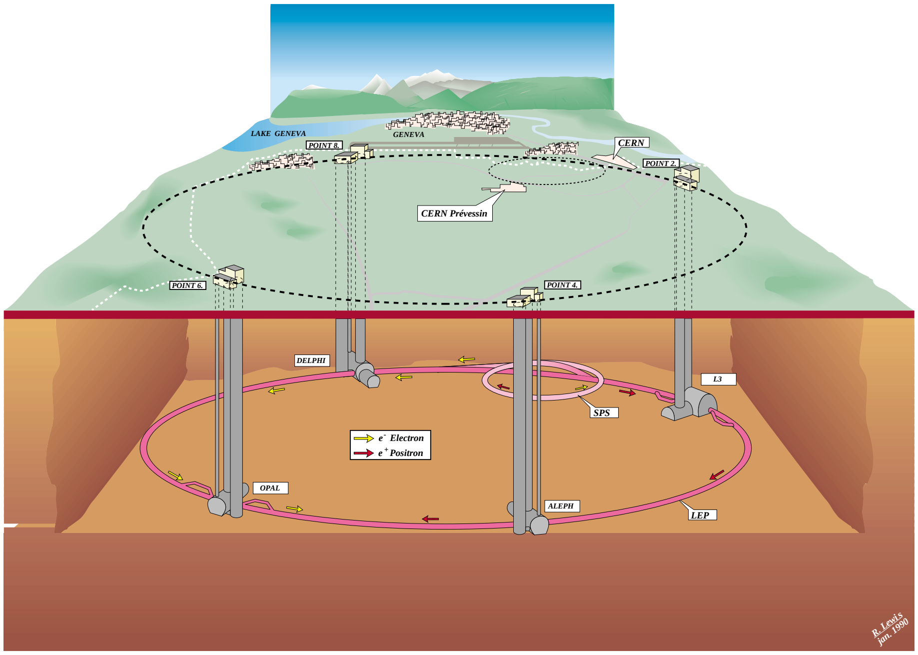

Figure 1.1: View of the LEP tunnel and of the four LEP experiments.

From its inauguration in 1989 to 1995, LEP operated at a centre of mass energy, $\sqrt{s}$, close to 91.2 GeV; in late 1995 the energy was increased to 130 GeV and later that year to 136 GeV. In 1996 the W pair production threshold was reached with a centre of mass energy of 161 GeV and at the end of that year the energy was increased further to 172 GeV. In 1997, with an energy of 183 GeV, also the threshold for Z boson pair production had been reached.

At LEP1 energies, normal conducting cavities were used. At LEP2 since the centre of mass energy is more than twice higher, 240 super-conducting cavities were installed gradually from 1995 to the winter shutdown 1996/1997 in order to compensate for the additional synchrotron radiation loss. In 1998 the centre of mass energy has been further increased to 189 GeV.

1.1.1 Luminosity

An important parameter of the collider is the "luminosity" which represents the rate of the e^+e^- interactions per unit surface and has to be maximized in order to have as many particle interactions as possible. It is defined by the following formula:

$$\mathcal{L}_s = \frac{N_{e^-} N_{e^+} n_b f}{4\pi\sigma_x\sigma_y} \tag{1.1}$$

where $N_{e^\pm}$ is the number of $e^\pm$ per bunch, n_b the number of bunches per beam, f the revolution frequency of a bunch and σ_x and σ_y are the vertical and horizontal size of the beam.

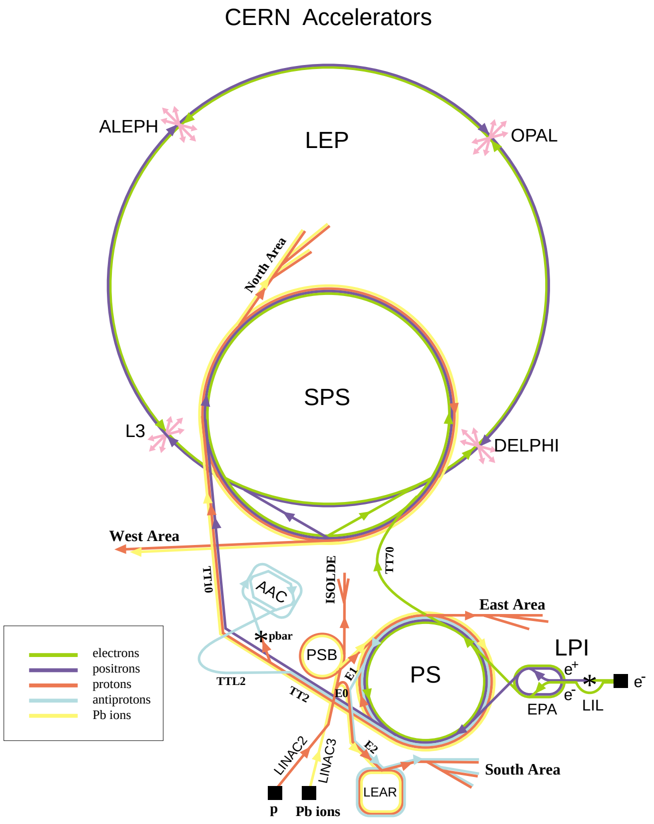

LEP: Large Electron Positron collider
SPS: Super Proton Synchrotron
AAC: Antiproton Accumulator Complex
ISOLDE: Isotope Separator OnLine DEvice
PSB: Proton Synchrotron Booster
PS: Proton Synchrotron

LPI: Lep Pre-Injector
EPA: Electron Positron Accumulator
LIL: Lep Injector Linac
LINAC: LINear ACcelerator
LEAR: Low Energy Antiproton Ring

Figure 1.2: LEP and the pre-accelerator system at CERN.

In the following text only the integrated luminosity $\mathcal{L}$, obtained by integrating eq. 1.1 over the time interval of data taking, will be used. As we will see later (sec. 1.2.7), it is up to the single experiments to measure as accurately as possible the integrated luminosity.

1.1.2 Beam energy

At LEP1 the beam energy was measured via the resonant depolarization of a transversally polarized beam [11], with an error of about 1 MeV [12]. At beam energies above 60 GeV machine imperfections cause resonances which destroy the polarization, therefore LEP is forced to calibrate the beam energy around the Z boson resonance and then extrapolate the results to higher energies [13].

Two devices are available to perform the extrapolation: the ”nuclear magnetic resonance” probes (NMR), which measure the changes of the local magnetic fields, and the “flux loop”, several electrical loops that, inserted into the magnets, measure a current in presence of a change in the magnetic field strength of the bending dipoles in the ring.

The NMR probes and the flux loop measurements were calibrated at 45 GeV and 50

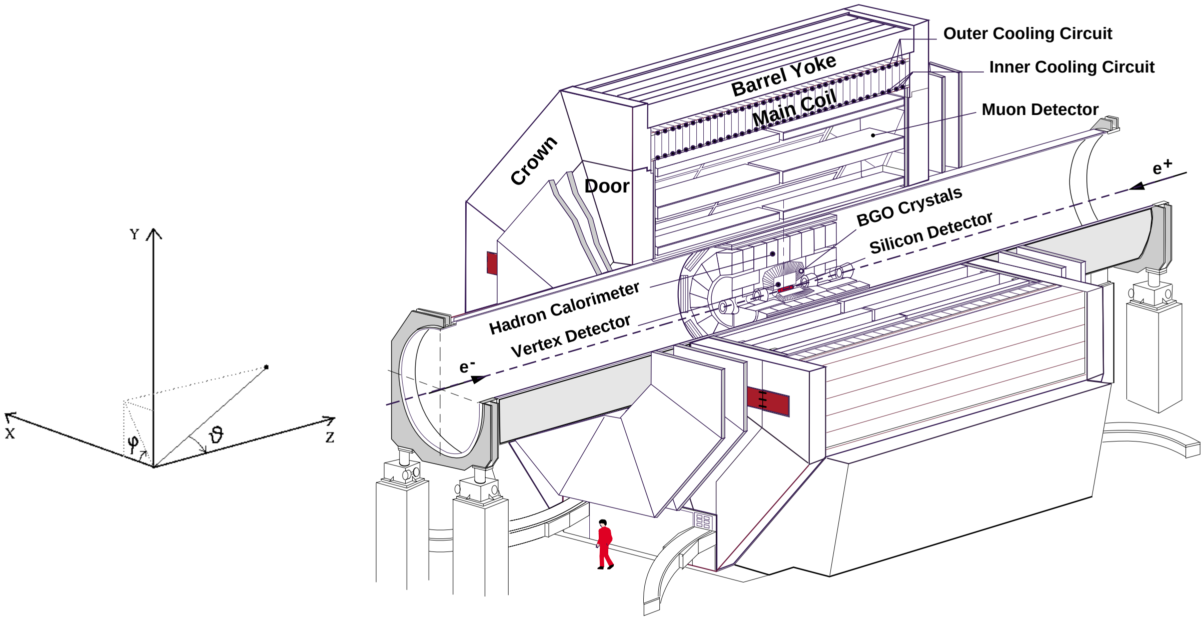

Figure 1.3: Perspective view of the L3 detector.

GeV with the resonant depolarization procedure. As the two measurements are independent, they permit to cross check the extrapolation. As a result for the data at the W boson pair production threshold, the measure of the centre of mass energy was 161.31±0.05 GeV. The result of the measurement for the data taking at the end of 1996 was 172.13 ± 0.06 GeV[1]. The energy measured for the data taking of 1997 was 182.68 ± 0.05 GeV[2]. The errors on the energies are almost entirely due to the error assigned to the extrapolation [10].

1.2 The L3 experiment

The L3 detector [8] is located 50 m underground (fig. 1.1) in one of the four interaction points of LEP. It is a multi-purpose detector with (fig. 1.3, 1.4) a central part, called “barrel”, which has a cylindrical symmetry around the beam axis, and a set of “endcaps” elements in the forward and backward directions, thus covering about 99% of the solid angle.

The barrel part consists (fig. 1.5) of the microvertex detector, the vertex chamber, the electromagnetic calorimeter, the hadron calorimeter and the muon filter. The barrel lies inside a, 32 m long and 4.45 m diameter, steel support tube.

The muon spectrometer, constituted by three concentric layers, is mounted outside the support tube and inside an octagonal shaped solenoidal magnet that provides a magnetic field of about 0.5 T parallel to the beam axis.

---

[1] Luminosity averaged energy of data recorded at 172.32 GeV, the majority, and 170.31 GeV.

[2] Luminosity averaged energy of data recorded at 181.70 GeV, 182.72 GeV, the majority, and 183.79 GeV.

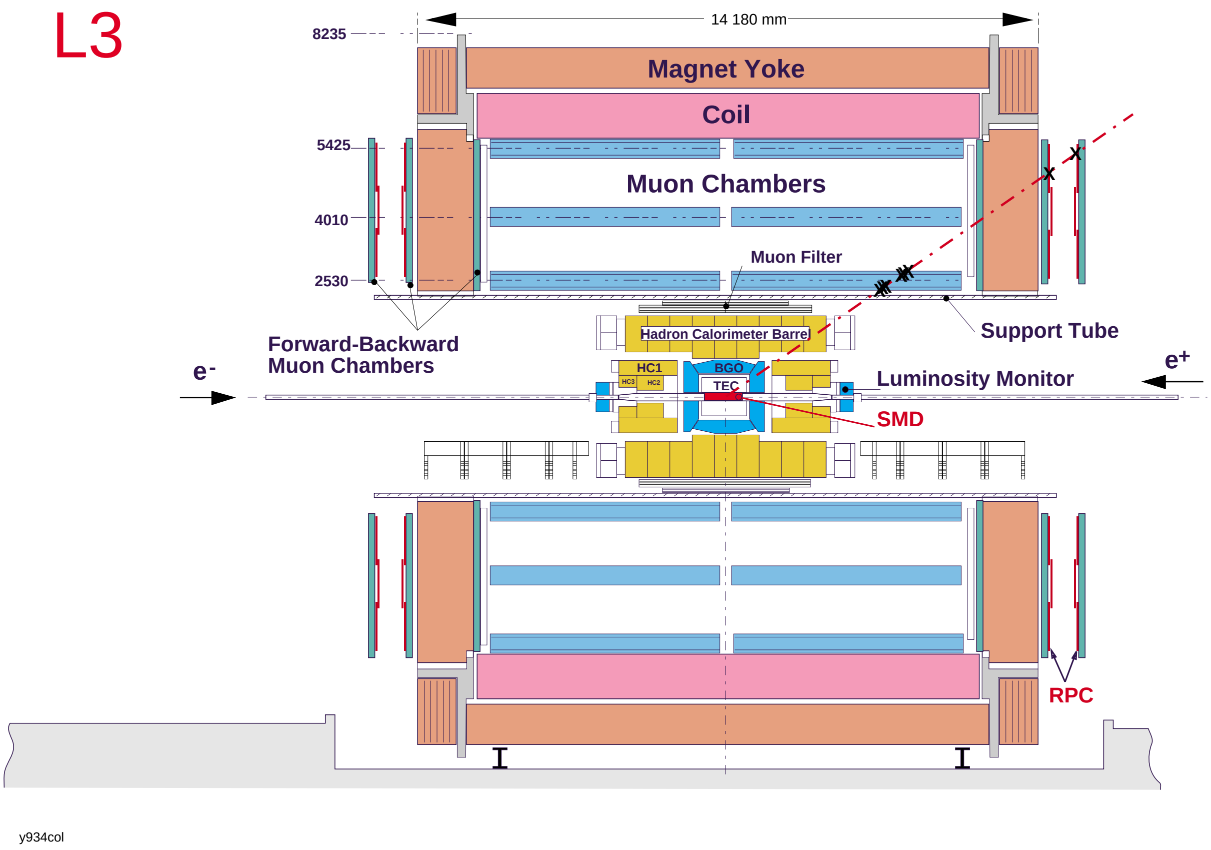

Figure 1.4: Side view of the L3 detector.

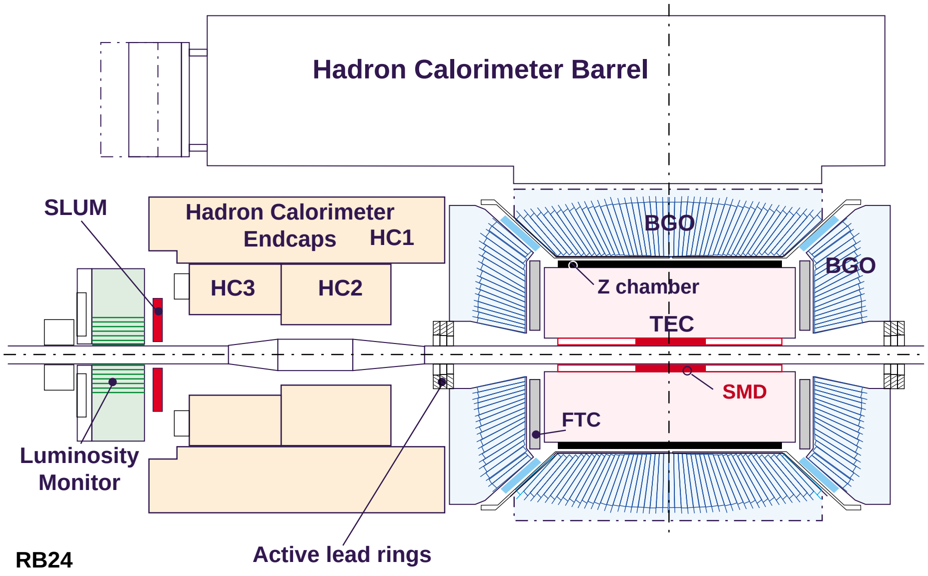

Figure 1.5: Side view of the inner part of the L3 detector.

The endcap elements consist of the hadron calorimeter, the electromagnetic calorimeter, the active lead ring and the forward muon chamber. Moreover two electromagnetic low angle detectors, called "luminosity monitors", are placed at 2.9 m upstream and downstream from the interaction point.

The L3 detector is the largest of the four LEP experiments with a length of 14 m and a diameter of 16 m.

In fig. 1.3 it is also shown the L3 coordinate system with the origin at the interaction point; the z axis is along the beam direction, the y axis, orthogonal to the LEP collider plane, points up while the x axis points towards the collider centre; ϑ is the polar angle and φ the azimuthal one.

In the following sections the different components will be described in more details.

1.2.1 The central tracking system

SMD The silicon microvertex detector (SMD) [14] is the innermost part of the central tracking system of L3 (fig. 1.5). It is composed of two double coordinate readout silicon detector layers, ~ 300 μm thick and ~ 30 cm long, located near the interaction point at a radius of 6.4 and 7.9 cm respectively. It covers a $29.4^\circ \leq \vartheta \leq 150.6^\circ$ angular region with both layers ($24.5^\circ \leq \vartheta \leq 155.5^\circ$ using only the innermost) and is used for a precise measurement of charged particle tracks and secondary vertices.

The resolution is 7 μm in the $r - \varphi$ plane and 14 μm in the $r - z$ plane [14].

TEC The time expansion chamber (TEC) [15] is used, together with SMD, for the measurement of charged particles momenta.

It is about 1 m long and reaches a radius of 31.7 cm, thus covering a $25^\circ \leq \vartheta \leq 175^\circ$ angular region. It consists of two concentric, cylindrical wire chambers with the wires parallel to the beam direction.

Both the inner and the outer chambers use the time expansion principle [16], reaching an average spatial single wire resolution of 50 μm and a double track resolution of 650 μm; the resolution on the transverse momentum is $\Delta \mathrm{p_t}/\mathrm{p_t^2} = 0.022/\mathrm{GeV}$.

Z chamber The TEC is surrounded by two cylindrical proportional chambers called the Z detector (fig. 1.5). It is used to improve the Z position measurement of a charged track respect to the measurement obtained by the TEC alone. The Z chamber has an angular coverage ϑ from 45° to 135° and measures a single track with a resolution of 320 μm in z (the double track resolution is 10 mm).

1.2.2 The electromagnetic calorimeters system

ECAL The electromagnetic calorimeter (ECAL) [8] consists of about 11000 bismuth germanium oxide (BGO) crystals used both as showering and detecting medium to precisely measure the energy and position of electrons and photons. It is subdivided in two symmetric half-barrels and endcaps.

The barrel part contains 7860 crystals and covers the $42° \leq \vartheta \leq 138°$ angular region; the endcaps contain 1536 crystals each, and extend the angular coverage to $11° \leq \vartheta \leq 38°$ and $142° \leq \vartheta \leq 169°$.

The crystals have the shape of a truncated pyramid with a front face of 2cm x 2cm, a rear face of 3cm x 3cm and a length of 24 cm (corresponding to 21 radiation lengths), and point in the direction of the vertex.

The BGO scintillation light is detected using two photodiodes per crystals (which are insensitive to the magnetic field of 0.5 T inside the magnet) glued to the back plane of each crystal. To ensure a good resolution over the full spectrum from 100 MeV to 100 GeV the readout is organized in two separate chains optimized for high energy and for low energy measurements respectively.

The BGO resolution is $\sim 5\%$ at 100 MeV and less than 1.5% at higher energies; the measured spatial resolution for energy deposits greater than 2 GeV is $\sim$ 2 mm.

EGAP In 1996 the gaps present between the ECAL barrel and endcaps ($\sim 4°$) were filled by a new detector, called EGAP or SPACAL [17] ("spaghetti" calorimeter, fig. 1.6). It consists of lead bricks with several scintillation fibers inside and has been installed to improve the energetic resolution of photons and electrons in these regions (before 1996 the particles pointing in these gaps were detected in the first radiation lengths of the hadronic calorimeter located behind).

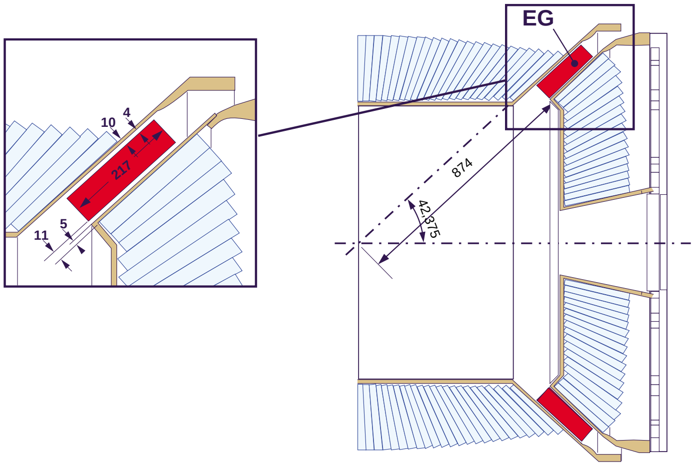

Figure 1.6: Lateral view of the Egap detector.

ALR In 1992 a new detector composed by lead rings interleaved with scintillation plates (thus called Active Lead Ring or ALR) [18] was installed below the electromagnetic endcaps to cover the polar regions $4° \leq (\vartheta, \pi - \vartheta) \leq 9°$ (fig. 1.5). It acts as an electromagnetic calorimeter between the BGO and the luminosity monitors and improves the energy resolution of low angle electrons and photons.

Luminosity monitors The luminosity monitors consist of two BGO calorimeters and two silicon microstrips detectors, located 2.86 m apart from the interaction point and are used mainly for the measurement of LEP luminosity described later in this chapter.

The two calorimeters [8] have an inner radius of 68.2 mm and an outer one of 191.4 mm and cover the 1.4° $\leq (\vartheta, \pi - \vartheta) \leq$ 4.0° polar region and have an energy resolution of $\sim$ 2% at 45 GeV and an angular resolution of 0.4 mrad in ϑ and 0.5 mrad in φ.

The two silicon microstrips detectors (SLUM, fig. 1.5) [19] were installed in front of the two calorimeters in 1993 in order to improve the spatial resolution.

[illegible] counters

The [illegible] system [8, 20] consists of 30 single plastic counters read out on both sides by photomultipliers. They are located between the electromagnetic and hadronic calorimeters (fig. 1.7), covering the polar region 25° $\leq \vartheta \leq$ 155°. This detector is used to trigger hadronic events and to distinguish dimuon events from cosmic ray background, in fact the measured time of flight of a cosmic muon is 5.8 ns while it is nil for the dimuon system $\mu^+\mu^-$, considering the time resolution (< 1 ns) of the scintillation counters.

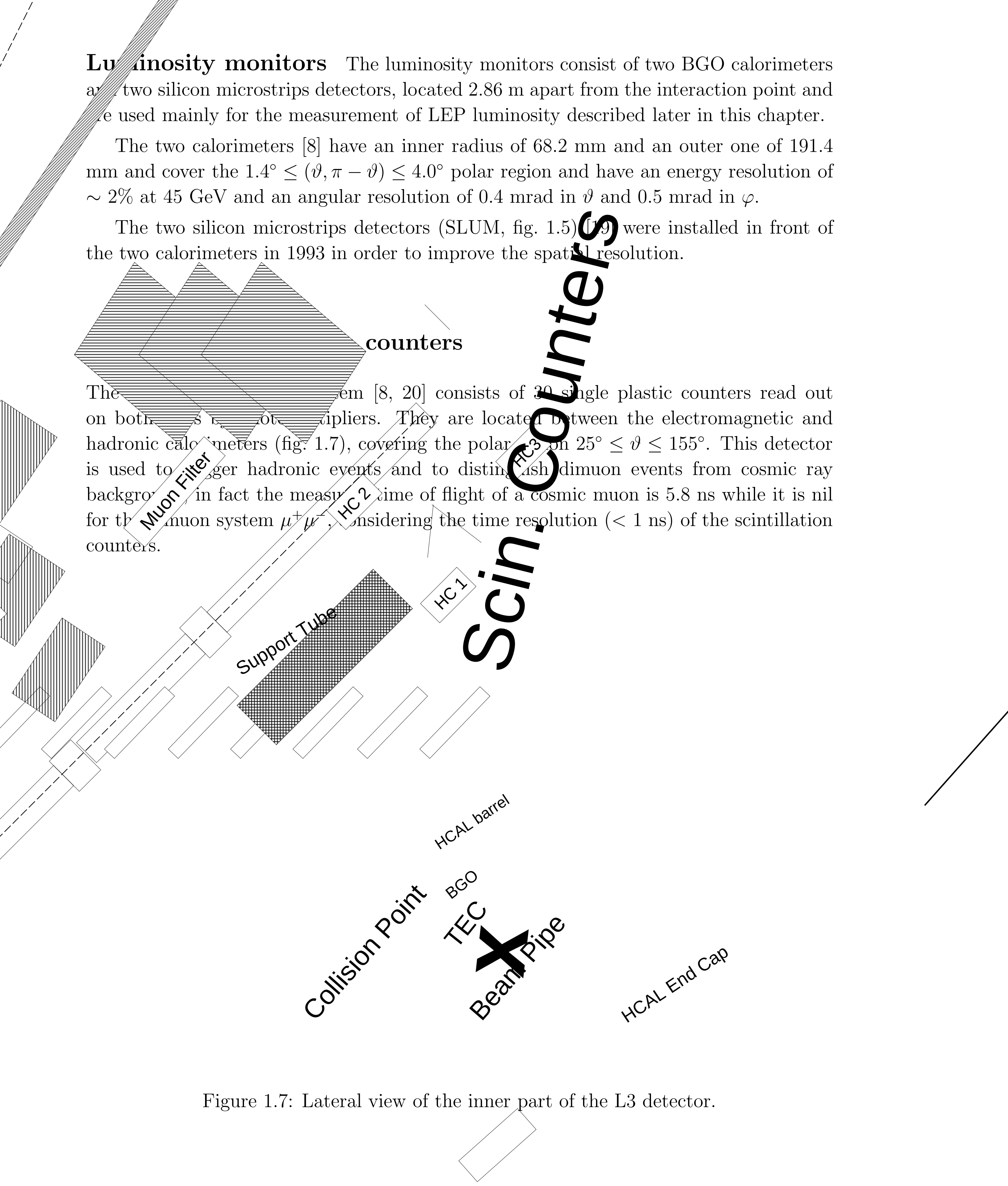

Figure 1.7: Lateral view of the inner part of the L3 detector.

1.2.4 The hadron calorimeter and the muon filter

The hadron calorimeter HCAL [8, 21] is a fine sampling calorimeter made of depleted uranium absorber plates interspersed with proportional wire chambers. It is used to measure the energy and position of hadrons, as well as to block all showering particles so that they do not reach the precision muon detector.

It is divided in a barrel part, composed of 144 towers (9 rings of 16 modules each), that covers the $35° \leq \vartheta \leq 145^0$ region, and a forward-backward part (endcaps) that extends the coverage down to 5.5° (fig. 1.7).

The energy resolution of the hadron calorimeter, together with the other sub-detectors, measured with jets coming from the Z decay, is:

$$\frac{\sigma(E)}{E} = \frac{55\%}{\sqrt{E}} + 8\%$$

where E is expressed in GeV; the angular resolution on jets direction is $\sim 2° - 3°$.

To further increase the hadron blocking power, a muon filter has been installed between the calorimeter and the support tube (fig. 1.7), thus adding ~ 1 interaction length to the ~ 4 of the hadronic calorimeter. It consists of eight octants, each made of six brass absorber plates interleaved with five layers of proportional tubes, thus improving the reconstruction of muon tracks detected by the outer muon chambers.

1.2.5 The muon chambers

The muon detector [8] consists of two ferris wheels, each composed of eight octants, and is located outside the support tube (fig. 1.4). Each octant consists of five precision (P) drift chambers; there are two chambers (MO) in the outer layer, each with 16 signal wires, two chambers (MM) in the middle layer, each with 24 signal wires, and one inner chamber (MI), with 16 signal wires (fig. 1.8).

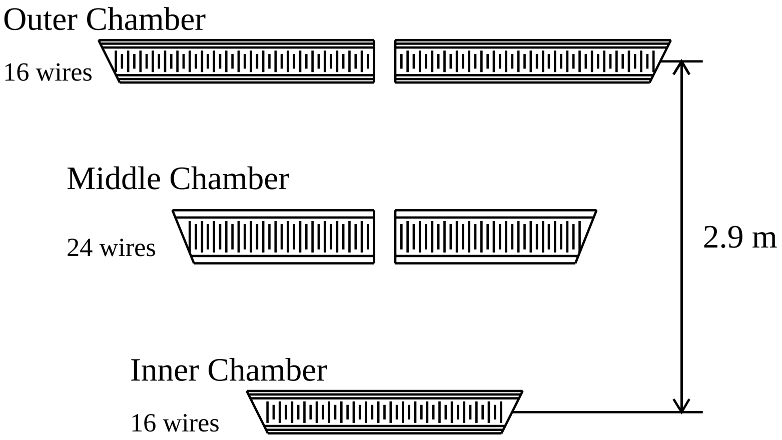

Figure 1.8: View of an octant of the muon detector with its five chambers.

The angular coverage is $44^\circ \leq \vartheta \leq 136^\circ$ for the three layers, while it is $35^\circ \leq \vartheta \leq 145^\circ$ considering just the two innest layers. The wires of the P chambers are parallel to the beam axis, thus they measure the x and y coordinate of the tracks; the muon transverse momentum is extracted from the sagitta of the track (fig. 1.9).

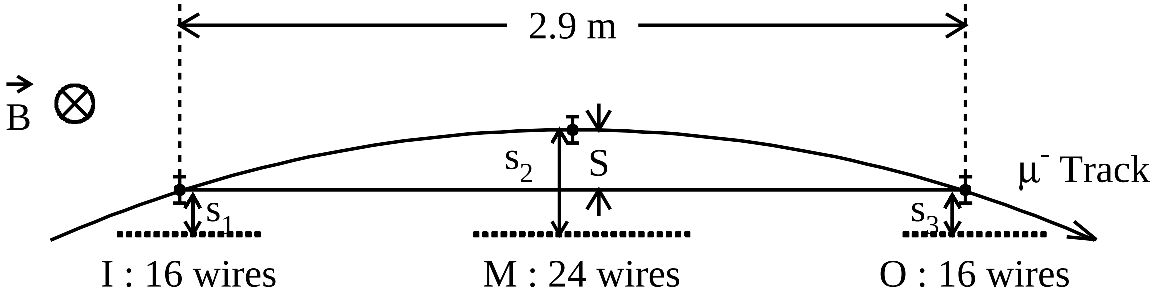

Figure 1.9: The sagitta is used to compute the muon momentum.

The top and bottom covers of the MI and MO chambers consist of drift chambers used to measure the z coordinate (named Z chambers).

The single wire resolution of the P chambers is 200 μm which allows to measure a 45 GeV muon with an error $\delta p_T/p_T$=2.5%. The resolution of the Z chambers is $\sim$ 500 μm.

In 1995 the forward and backward muon chambers were installed (fig. 1.4). They consist of three layers of drift chambers and extend the angular coverage to $24^\circ \leq (\vartheta, \pi - \vartheta) \leq 44^\circ$. This system uses the high return magnetic field, given by the forward and backward steel doors of L3, to curve the low polar angle muons, and thus measure their transverse momentum.

1.2.6 The trigger

Every beam crossing the trigger system [22] has to decide if an e^+e^- interaction has occurred and eventually record the detector signals. In order to reduce the dead time, this decision is taken using a cascade of three trigger levels with intermediate buffering.

The first level has five triggers based on raw informations coming from the calorimeters (electromagnetic and hadronic), the luminosity monitors, the scintillation counters, the muon chambers and the TEC chamber. To ensure good efficiency for each physics channel, these five blocks are logically OR'd to arrive at a decision that is taken in a time less than 22 μs. On a positive result from any of the five, the data are digitized and recorded in buffer memories in less than 500 μs; on a negative result, all the electronic front-ends are cleared for the next beam crossing. The level-1 rate of positive decisions is less than 8 Hz (the rate of beam crossing is $\sim$ 45 KHz), with a dead time caused from the fine digitization of less than 5%.

The main task of the second level trigger is to reject background events selected by level-1, mainly beam gas and beam wall interactions, synchrotron radiation and electronic noise. Level-2 uses the same raw informations of level-1, but can spend more time per event without introducing additional dead time. After level-2 the rate is typically less than 6 Hz.

Level-3 applies about the same level-1 selection criteria to the complete set of digitized data, reducing the output rate to 2-3 Hz.

1.2.7 Luminosity measurement

In section 1.1 the luminosity definition has been introduced. This parameter is essential for the cross section measurement of any physical process; in fact the number of events N_{ev} of a certain physical process is related to the relative cross section σ and to the integrated luminosity[3] $\mathcal{L}$ through the following relation:

$$N_{\mathrm{ev}} = \varepsilon \cdot \sigma \cdot \mathcal{L} \tag{1.2}$$

where ε is the selection efficiency for that process.

The luminosity cannot be determined using the relation 1.1 because the bunch geometry and the bunch overlap during the crossing are not known precisely enough. Therefore it is measured using relation 1.2 for a physical process with a large[4] and extremely well known cross section. At LEP the ideal process for this purpose is low-angle Bhabha scattering; in fact its cross section at low polar angle is very large and it is dominated by the exchange of a photon in the t-channel; thus it is essentially a QED process whose cross section can be computed with high precision.

As already mentioned in section 1.2.2 the luminosity monitors are used for this measurement. A typical Bhabha event shows two energy deposits of $\sqrt{s}/2$ back to back in this detector. The main background comes from beam gas and beam wall interactions and from $\gamma\gamma$ events, described in the next chapter.

For the event selection a fiducial volume in the luminosity monitors is chosen, rejecting events that hit the crystals on the border of the detector (fig. 1.10).

The total cross section of the Bhabha scattering, integrated on the fiducial volume, at first perturbative order, is:

$$\sigma \simeq \frac{16\pi\alpha^2}{s}\left(\frac{1}{\vartheta^2_{\mathrm{min}}} - \frac{1}{\vartheta^2_{\mathrm{max}}}\right)$$

where α is the QED fine structure constant.

The selection efficiency ε is determined applying the same data selection criteria to a Monte Carlo sample obtained simulating the response of the L3 detector to events generated with two Monte Carlo generators: BHLUMI [23] and BABAMC [24]; this second also includes electroweak corrections due to the γ/Z interference.

The systematic errors of the measurement of the luminosity stem from the theoretical error on the cross section computation, from the event selection and from the errors on the

---

[3] In the following I will simply call it luminosity.

[4] In order to have a negligible statistical error respect to the systematic uncertainties.

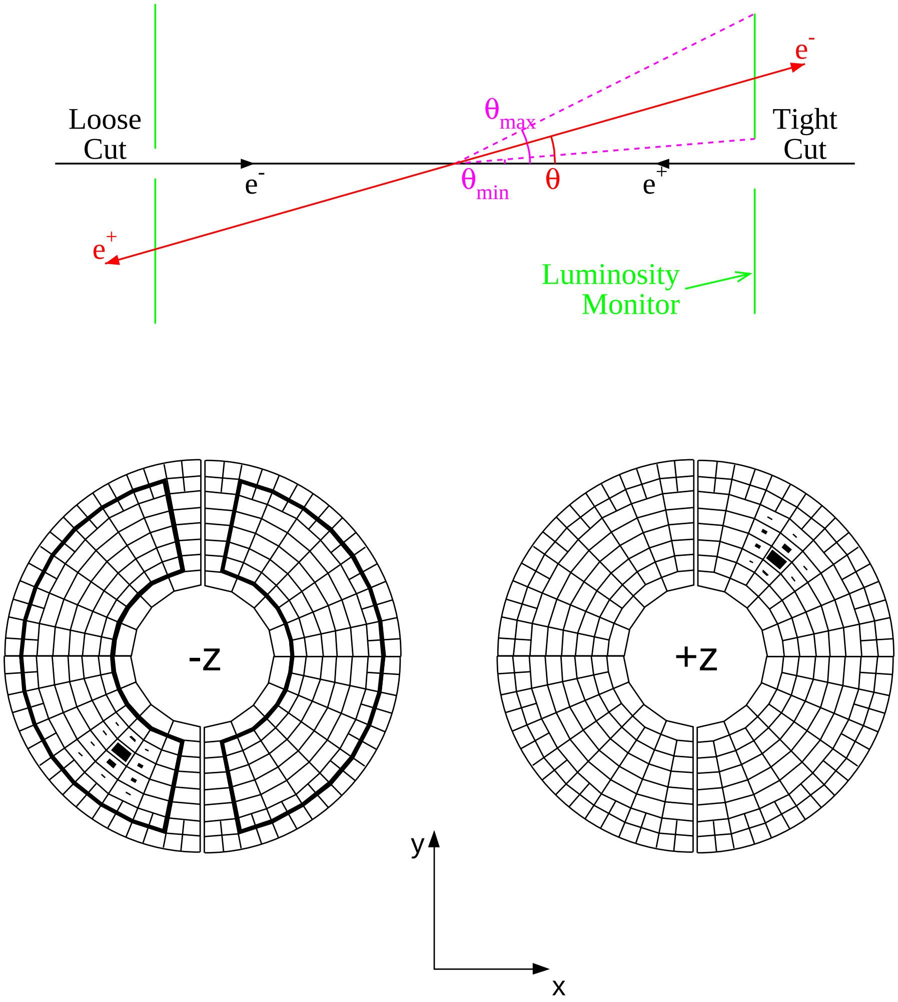

Figure 1.10: Bhabha event selected in the fiducial volume.

simulation. More details of the luminosity measurement in L3 can be found in reference [25].

The results of the measurement of the L3 luminosity at LEP2 with the relative errors are given in the following table [26]:

$\sqrt{s}$ (GeV)	$\mathcal{L}$ (pb^{-1})	$\Delta\mathcal{L}/\mathcal{L}$ (%)
161	10.90	0.6
172	10.25	0.6
183	55.47	0.3

Chapter 2

Physics at LEP2

The extremely accurate measurements of LEP1 have yielded a very detailed understanding of the fermionic interactions within the Standard Model and the parameters of the Z boson.

The intention of the LEP2 phase is to study the bosonic sector of the Standard Model via W pair production. The measurements from these studies will provide us with two very important pieces of informations about the Standard Model.

The primary physics goal of the LEP2 e^+e^- collider is the determination of the W mass, which before LEP2 has only been directly measured at hadron colliders; indirect estimates of the W mass have also been given from a global fit of the Standard Model to the electroweak data from LEP1 and SLC. The expected accuracy in the W mass determination at LEP2 of 30 MeV, comparable to the error on M_W from the global fit, will provide a stringent test of the Standard Model.

Another important piece of information that W pair production will provide is direct evidence[1] of bosonic self-interactions and a precise description of the predicted interactions of W, Z and γ bosons with each other (the so-called triple gauge coupling or TGC) within the Standard Model. These interactions are the most characteristic and fundamental signatures of a non-abelian gauge symmetry; they are described by triple gauge boson vertices ZW^+W^- and γW^+W^- and their accurate measurements are essential for a test of the Standard Model. In this thesis only the aspects related to W pair production cross section and W decay branching ratios will be taken into account.

Parallel to the studies of the W boson physics, LEP2 energies are an ideal opportunity for many new particles searches, in particular for the Higgs boson, in addition to continued studies of the $e^+e^- \to f\bar{f}$ process.

In this chapter I will describe the most important processes that occur at LEP2, in particular I will describe in detail the W pair production and all the physics processes that may constitute a background source to the W pair analysis.

In tab. 2.1 all such processes and the cross sections at $\sqrt{s} = 183$ GeV are listed.

At LEP1 energies the scenario is dominated by the Z resonance (fig. 2.1(a)); as shown in fig. 2.1(b) the typical cross sections of the LEP2 processes are some orders of magnitude lower.

---

[1] The high precision at LEP1 has provided the first evidence for gauge boson contribution via loops constituting an "indirect" evidence for bosonic self-interactions in the Standard Model.

Process	σ (pb)
$e^+e^- \to WW \to f_1\bar{f}_2f_3\bar{f}_4$	15.7
$e^+e^- \to Z/\gamma \to q\bar{q}(\gamma)$	107.5
$e^+e^- \to Z/\gamma \to e^+e^-(\gamma)$	1708
$e^+e^- \to Z/\gamma \to \mu^+\mu^-(\gamma)$	9.2
$e^+e^- \to Z/\gamma \to \tau^+\tau^-(\gamma)$	8.8
$e^+e^- \to e^+e^-e^+e^-$	680.9
$e^+e^- \to e^+e^-\mu^+\mu^-$	606.2
$e^+e^- \to e^+e^-\tau^+\tau^-$	381.7
$e^+e^- \to e^+e^-q\bar{q}$	4016
$e^+e^- \to ZZ \to$ all	0.6
$e^+e^- \to Ze^+e^- \to$ all	3.3
$e^+e^- \to We\nu \to$ all	0.7

Table 2.1: Main processes at LEP2 and relative cross sections (in pb) at $\sqrt{s} = 183$ GeV. The Bhabha process cross section has been calculated with a cut on the electrons polar angles ($\vartheta, \pi - \vartheta > 8^o$). The $\gamma\gamma$ cross sections have been calculated with an invariant mass cut of 15 GeV for the eeqq final state, 3 GeV for eeee and ee$\mu\mu$, and a cut of 4.25 GeV for ee$\tau\tau$ final state (see section 2.2.2).

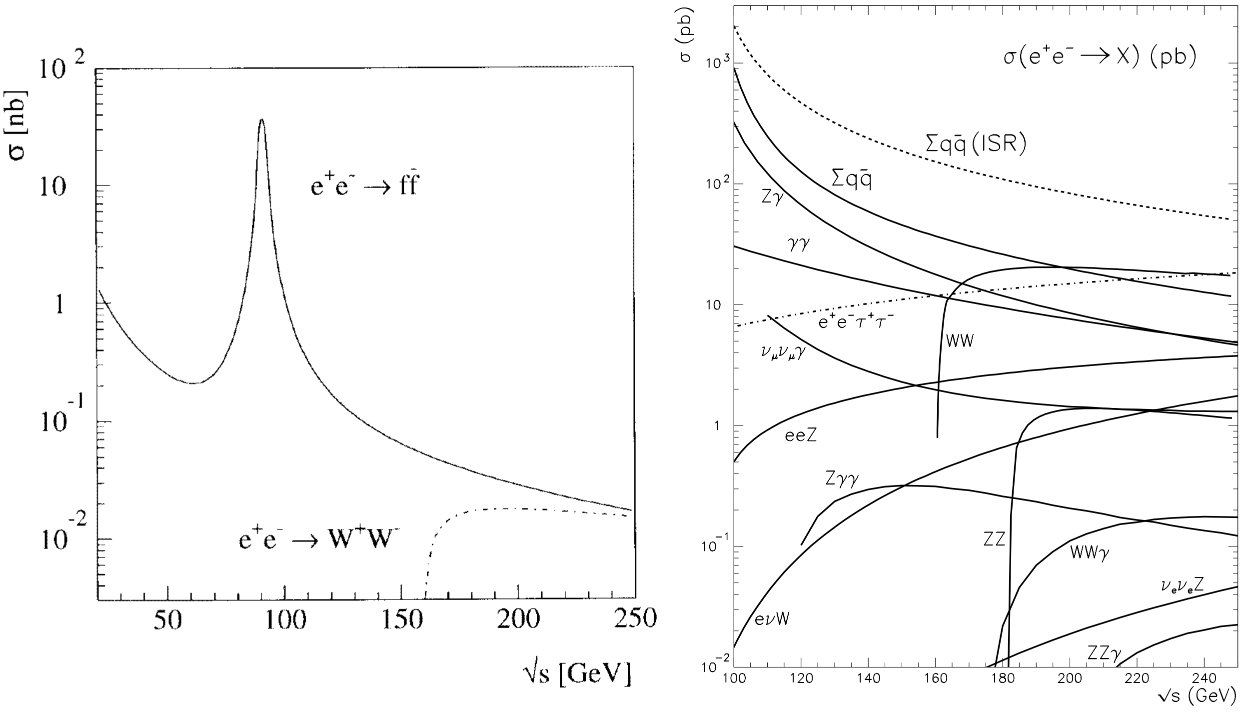

(a) (b)

Figure 2.1: (a) Cross section of the two fermion process at LEP1 and higher energies. (b) Cross sections for some typical processes at LEP2 energies.

2.1 W pair production

At LEP2 W bosons are produced in pairs in the electron-positron annihilation at a centre of mass energy greater than the kinematic threshold $\sqrt{s} = 2\,\mathrm{M_W}$. The decay of each W in a quark pair[2] or in a lepton pair produces a 4 fermions final state:

$$\mathrm{e^+e^-} \rightarrow \mathrm{W^+W^-} \rightarrow 4 \text{ fermions}$$

Depending on the different final states we can distinguish accordingly three topologies[3] (fig. 2.2):

- $\mathrm{W^+W^-} \rightarrow \mathrm{q\bar{q}q\bar{q}}$ hadronic or "four jet" channel
- $\mathrm{W^+W^-} \rightarrow \ell^-\bar{\nu}_\ell \mathrm{q\bar{q}}$ semileptonic channel
- $\mathrm{W^+W^-} \rightarrow \ell^-\bar{\nu}_\ell \ell^+\nu_\ell$ leptonic channel

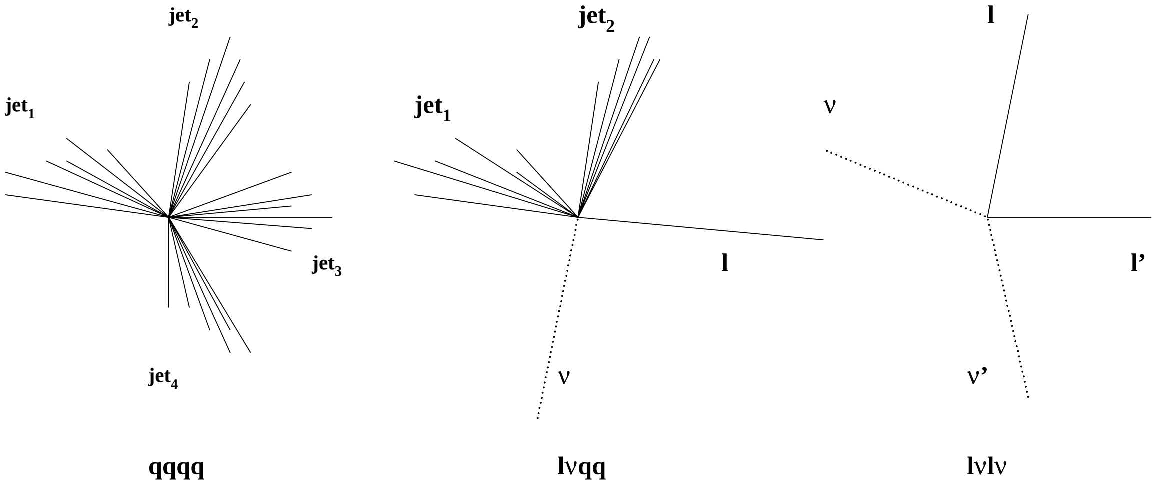

Figure 2.2: The three typical topologies of W pair decay.

In the next section I will introduce some aspects of the theoretical computation of the W pair production cross section; for a more complete description of all the details related to this calculation see ref. [28] and references therein.

I will first consider the production of two W on-shell, that is supposing a nil decay width Γ_W of the W boson, at the lowest order. Then I will describe the two off-shell W production, introducing a $\Gamma_W \neq 0$, still at the lowest order; this step consists in studying the process

$$\mathrm{e^+e^-} \rightarrow 4 \text{ fermions} \tag{2.1}$$

---

[2] Since the mass of the top quark is greater than $\mathrm{M_W}$, decays including the top quark are excluded.

[3] To be exact I should write $\mathrm{q\bar{q}'}$ instead of $\mathrm{q\bar{q}}$ since the two quarks coming from the same W are not of the same flavour but now and in the following text, for simplicity, I will omit the primes and I will indicate with $l\bar{\nu}$ both the pairs $l\bar{\nu}$ and $\bar{l}\nu$.

where only the Feynman diagrams with two resonant Ws are taken into account.

Then I will introduce the radiative corrections to the first order calculation; after that I will discuss the W width and the electroweak and QCD corrections to it.

The last step will be to consider all diagrams that contribute to the reaction 2.1, and not just the ones with a W resonant pair intermediate state, and I will give an operational definition of the cross section for the W pair production process.

2.1.1 On-shell W pair production

In the on-shell approximation, that is neglecting the decay of the W, the process $e^+e^- \rightarrow$ WW is described, at lowest order, by the three diagrams shown in fig. 2.3: the exchange of a γ or Z boson in the s-channel and the ν exchange in the t-channel.

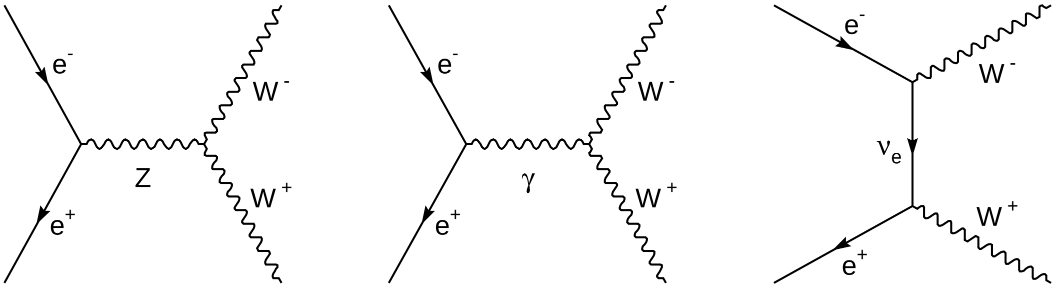

Figure 2.3: The three diagrams responsible for the on-shell W pair production.

The differential and total cross section on-shell, at lowest order (Born approximation) can be calculated analytically; near the threshold, that is for $\beta << 1$, where $\beta = \sqrt{1 - 4M_W^2/s}$ represents the W velocity, we have [29]:

$$\left(\frac{\mathrm{d}\sigma}{\mathrm{d}\Omega}\right)_{\mathrm{Born}} \simeq \frac{\alpha^2}{s}\frac{\beta}{4\sin^4\vartheta_{\mathrm{W}}}\left[1 + 4\,\beta\cos\vartheta\,\frac{3\cos^2\vartheta_{\mathrm{W}} - 1}{4\cos^2\vartheta_{\mathrm{W}} - 1} + \mathcal{O}(\beta^2)\right] \tag{2.2}$$

where ϑ_W is the weak mixing angle and is defined by $\cos\vartheta_{\mathrm{W}} = \frac{\mathrm{M_W}}{\mathrm{M_Z}}$.

In this expression the leading term $\propto \beta$ originates from the t-channel diagram only and is angular independent, while the two s-channels diagrams contribute to the term $\propto \beta^2\cos\vartheta$. As a consequence we expect that at production threshold ($\beta \simeq 0$) the W bosons are produced isotropically; when the centre of mass energy increases the W bosons will be produced more frequently in the forward direction.

Integrating out the angular dependence, the total cross section is then given by:

$$\sigma_{\mathrm{Born}} \simeq \frac{\pi\alpha^2}{s}\cdot\frac{\beta}{\sin^4\vartheta_{\mathrm{W}}} + \mathcal{O}(\beta^3) \tag{2.3}$$

The leading term is entirely due to the t-channel neutrino exchange (all terms $\propto \beta^2$ drop out and the s-channel and the s-t-interference contributions are proportional to β^3). Hence in the threshold region the cross section for $e^+e^- \rightarrow W^+W^-$ is not very sensitive to the couplings of the W to the photon and Z boson.

2.1.2 Off-shell W pair production

So far we have only considered the production of stable W bosons; now we will describe the W bosons as a resonance, with a finite width, and study the process:

$$\mathrm{e}^+\mathrm{e}^- \to W^+W^- \to f_1\bar{f}_2 f_3\bar{f}_4$$

In the lowest order this process is represented by the three Feynman diagrams shown in fig. 2.4.

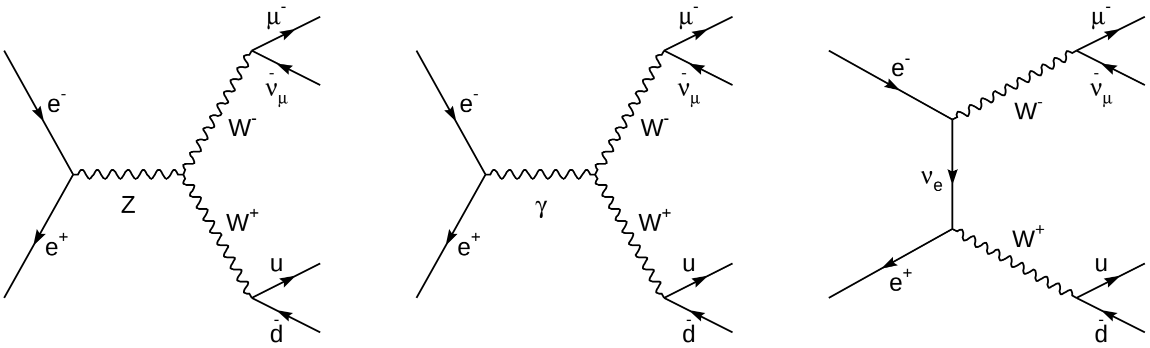

Figure 2.4: The three diagrams contributing, at lowest order, to the $\mathrm{e}^+\mathrm{e}^- \to \mathrm{W}^+\mathrm{W}^- \to \mu^-\bar{\nu}_\mu \mathrm{u}\bar{\mathrm{d}}$ process.

However the full four fermion process does not only proceed through these three doubly resonant diagrams. There are also contributions from other diagrams with the same initial and final state, but different intermediate states. These so-called charged current processes are referred to as CCn, with n denoting the number of contributing diagrams (in this case CC03).

The cross section computation in the off-shell case is much more involved than in the on-shell case, so that also at lowest order it can only be done using numerical integration techniques, either semi-analytical or Monte Carlo.

Semi-analytical approach

In the semi-analytical approach the finite W width in the CC03 cross section calculation is introduced by convoluting two Breit-Wigner densities $\rho(s)$ with the on-shell cross section σ^0_{WW} (analytically computable).

$$\sigma(s) = \int_0^s \mathrm{d}s_1\,\rho(s_1)\int_0^{(\sqrt{s}-\sqrt{s_1})^2} \mathrm{d}s_2\,\rho(s_2)\,\sigma^0_{\mathrm{WW}}(s;s_1,s_2) \qquad (2.4)$$

$$\rho(s) = \frac{1}{\pi}\frac{\Gamma_W}{M_W}\frac{s}{(s-M_W^2)^2+s^2\Gamma_W^2/M_W^2} \qquad (2.5)$$

where s_1 and s_2 are the masses of the two Ws. In the W propagator a variable (s dependent) width has been used[4]:

$$\Gamma_W(s) = \frac{s}{M_W^2}\Gamma_W$$

This semi-analytical approach allows to perform the numeric integration with a good precision and in a reasonable time.

This integration technique is used by the program GENTLE [31] and represents an important benchmark for the Monte Carlo programs.

Fig. 2.5 shows the inclusive cross section both in the on-shell and off-shell approximation as a function of the centre of mass energy, computed using the GENTLE program. The inclusion of a non nil W width has the effect of smoothing the behavior of the cross section near the threshold.

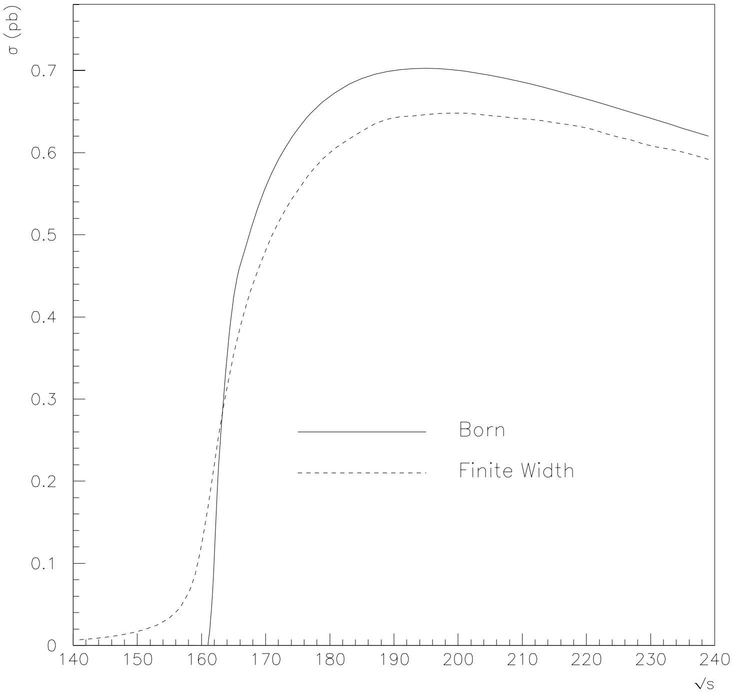

Figure 2.5: Comparison of the W pair production cross sections computed in the on-shell and off-shell approximations.

Monte Carlo approach

In the Monte Carlo approach the cross section for the off-shell W pair production is determined through the Monte Carlo integration of the differential cross section directly computed from the matrix elements.

---

[4] I would want to remark that this parameterization represents a definition of the W mass, similar to the one used for the Z at LEP1. A choice of a W constant width, equally well justified from a theoretical point of view, would imply a different definition of $\mathrm{M_W}$. Anyway numerically the differences between the two definitions are below the expected experimental accuracy [30].

The Monte Carlo technique is slower than the semi-analytical integration, but it has the advantage of calculating the differential distributions of the kinematical variables of the W and its decays. This allows the generation of events that can be used to study the analysis procedures developed for real data, taking into account the experimental effects of the detector.

For the analysis discussed in this thesis we have used the Monte Carlo programs KORALW [32] and EXCALIBUR [33].

2.1.3 Radiative corrections

I will now introduce the radiative corrections to the first order cross section calculation discussed so far.

At LEP1 we were used to distinguish the radiative corrections into QED and weak corrections, but the presence of the charged current at lowest order in $e^+e^- \to W^+W^-$ implies that the corresponding radiative corrections cannot be separated on the basis of Feynman diagrams into electromagnetic and weak contribution in a gauge invariant way [28].

The complete radiative electroweak $\mathcal{O}(\alpha)$ corrections have been calculated by several groups [35, 36] only for the on-shell case. The same calculation for the off-shell W pair production is very involved and so far no complete treatment for the $\mathcal{O}(\alpha)$ corrections is available. In the off-shell case some approximations are hence used, but some terms in the radiative corrections are still missing. However the complete set of $\mathcal{O}(\alpha)$ corrections computed for the on-shell case can be used to estimate the magnitude of these missing terms and the error given by the approximations, with the assumption that the missing terms are of the same order as for the on-shell case.

Using the on-shell calculation as a guide, it is possible to predict some of the largest effects. For example, it has been shown that close to threshold the dominant contribution comes from the Coulomb correction (the long range electromagnetic interaction between the two almost stationary Ws). Also important is the emission of photons collinear with the initial state e^+e^- (initial state radiation, ISR), which gives rise to the logarithmic correction term $\propto \alpha \ln(s/\mathrm{m}_e^2)$. Finally some higher order fermion and boson loop corrections can be taken into account by a particular choice of the electroweak coupling constants.

Each of these effects will be discussed in the following.

Coulomb correction

The Coulomb correction originates from the long range electromagnetic interaction between the two charged Ws in the final state (fig. 2.6).

The Coulomb correction is substantially limited by effects that truncate the range of the interaction, like the off-shellness and the decay of the W boson; in fact this correction would diverge if not screened by the finite width of the W. As a consequence, higher order Coulomb corrections are not important.

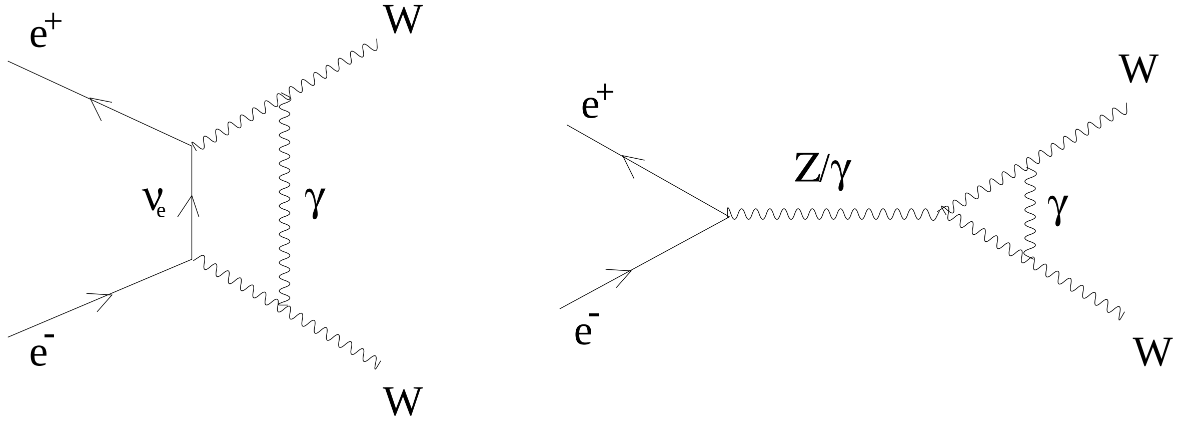

Figure 2.6: Diagrams responsible for the Coulomb correction.

At the lowest order it can be calculated as[5] [37]:

$$\sigma(s) = \int_0^s \mathrm{d}s_1 \int_0^{\left(\sqrt{s}-\sqrt{s_1}\right)^2} \mathrm{d}s_2\, \rho(s_1)\, \rho(s_2)\, \sigma_0(s, s_1, s_2)\, [1 + \delta_c(s, s_1, s_2)]$$

where

$$\begin{aligned} \delta_c(s, s_1, s_2) &= \frac{\alpha}{v} \cdot \left[\pi - 2 \cdot \mathrm{arctg}\left(\frac{|k|^2 - p^2}{2p\,\mathrm{Re}(k)}\right)\right] \\ v &= \frac{4p}{\sqrt{s}} = 2\sqrt{1 - \frac{2s(s_1+s_2) - (s_1-s_2)^2}{s^2}} \\ k &= \sqrt{-M_W(E + i\Gamma_W)} \quad , \qquad E = \frac{s - 4M_W^2}{4M_W} = \frac{s}{4M_W} \cdot \beta \end{aligned}$$

The $\delta_c(s, s_1, s_2)$ expression is inversely proportional to v, the average velocity of the W bosons in their centre of mass system, hence the effects of the Coulomb corrections are particularly large close to the threshold, where the two Ws are essentially at rest, and where it produces a 6% increase in the off-shell WW cross section. However also at higher energies the exchange of a soft photon has visible effects as shown in fig. 2.7.

Initial state radiation (ISR)

Another important correction comes from the emission of collinear photons from the incoming e^+ and e^-, also known as Initial State Radiation (ISR).

ISR lowers the available centre of mass energy for the W pair production and consequently lowers the CC03 cross section (fig. 2.7). Furthermore the subsequent boost of the centre of mass frame of the Ws also smears out the W production angular distribution. The energy distribution of the radiated photons is shown in fig. 2.8, as predicted by the KORALW generator, at $\sqrt{s}$=183 GeV.

---

[5] Same notation as in eq. 2.4

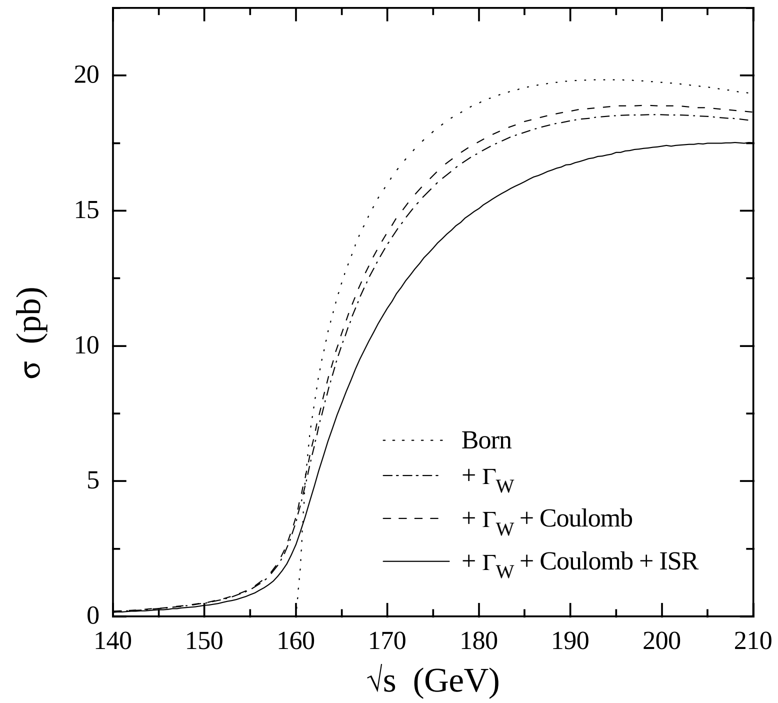

Figure 2.7: Influence of W width, Coulomb correction and initial state radiation (ISR) in the CC03 cross section.

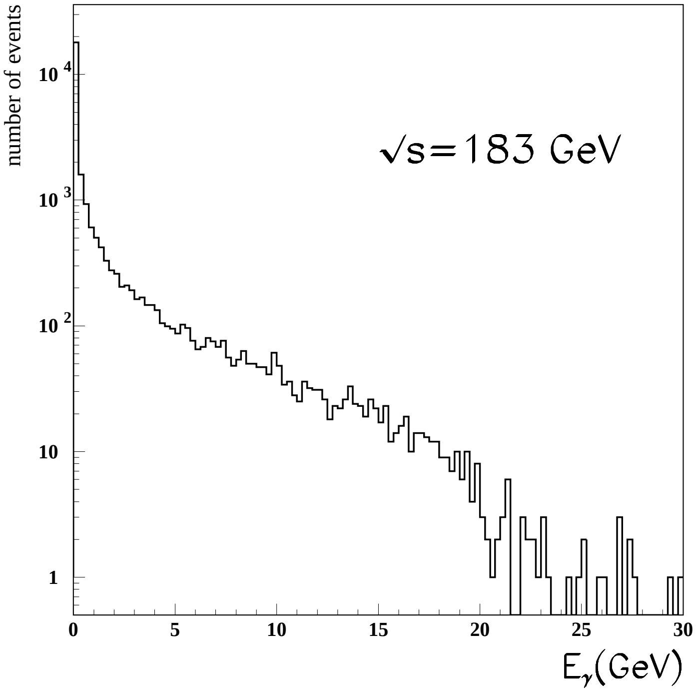

Figure 2.8: Energy distribution of the photons radiated in the initial state (ISR) in the $e^+e^- \rightarrow WW$ process, as predicted by KORALW.

In the off-shell case a complete $\mathcal{O}(\alpha)$ calculation of this correction is not available, therefore people have turned towards approximate descriptions which include the leading effects up to the second order.

In GENTLE and EXCALIBUR programs the IRS is implemented using the "structure function" method [39], taken over from QCD, where the corrections are calculated by convoluting the lowest-order cross section with the appropriate structure function:

$$\sigma(s) = \int_0^1 \int_0^1 \mathrm{d}x_1 \, \mathrm{d}x_2 \, \Phi(x_1) \, \Phi(x_2) \, \sigma_0(x_1, x_2, s)$$

where $\sigma_0(x_1, x_2, s)$ is the non radiative cross section and the function Φ represents the energy distribution of a fermion after radiation; an expression of the function Φ can be found in [38].

The actual implementation of ISR is done by first generating a centre of mass energy according to the function Φ, and then constructing the complete event in the rest-frame. The event is then boosted in the laboratory frame to compensate for the momentum of the emitted photons.

This technique does not take into account the radiation off the Ws and the fermions in the final state, and its interference with the initial state radiation.

The order of these missing corrections is estimated to be about 2% [28], comparing the off-shell case to the on-shell one, where these corrections have been calculated. This constitutes the greatest uncertainty on the total theoretical cross section computation.

Moreover, since in this approach the photon energy spectrum is integrated from the start, the Monte Carlo generators that use this technique, like EXCALIBUR, can only generate hard photons with nil transverse momentum (p_T=0), that is collinear with the z axis.

A completely different approach to the ISR calculation is possible if a MC numerical integration technique is used instead of the semi-analytical computation. This is the case with the YFS[6] exponentiation technique [40] used by the KORALW generator.

This method allows the summing of all the soft photons (non detectable) and the exclusive generation of an arbitrary number of hard photons with non nil transverse momentum ($p_T \neq 0$); this is extremely useful for the simulation of the actual experimental cuts.

This technique also takes into account the photon radiation off the intermediate Ws.

The final state radiation (FSR), that is the radiation from the final state fermions, is supplied in the KORALW generator by the PHOTOS package [41]. The algorithm in PHOTOS provides the complete kinematic information in the splitting $f \to f'\gamma$; one problem arising when generating FSR from on-shell final state fermions is that energy-momentum in the splitting is not conserved. PHOTOS solves this problem by generating FSR for the process P$\rightarrow$ $f\bar{f}'$ for the decaying particle P ensuring energy-momentum conservation through a rescaling in the rest frame of the decaying particle. Consequently PHOTOS can only generate FSR for fermions coming from decays of unstable particles, that is our case, where the fermions are produced by the W decay.

---

[6] Yennie-Frautschi-Suura.

The precision of the YFS technique is limited by the absence of complete $\mathcal{O}(\alpha)$ corrections and is estimated to be about 2%, like the semi-analytical method [42].

Improved Born approximation

The dominant part of the electroweak corrections (apart from photon radiation) can be included by introducing effective couplings in the Born level expressions. This is referred to as the "Improved Born Approximation".

In the Standard Model three parameters are sufficient to parametrize the electroweak interactions, and the conventional choice is $\{\alpha, G_\mu$[7]$, M_Z\}$ since these are the three which are measured most accurately. In this case the value of M_W is a prediction of the model. Since the expression of M_W, because of the radiative corrections, depends on the top quark and the Higgs mass, a measurement of M_W provides a constraint on these masses.

However the set $\{\alpha, G_\mu, M_Z\}$ is not the best choice to describe WW production. The reason is that any variation of M_W has to be accompanied by an adjustment of the charged and neutral weak couplings; beyond leading order this is a complicated procedure.

A more appropriate choice of parameters for LEP2 is the set $\{M_W, G_\mu, M_Z\}$ (called G_μ-scheme), since in this case the WW cross section and all the other observables are directly computed as a function of M_W which is a free parameter of the model and can be varied without affecting the other parameters. For example the electroweak corrections in the on-shell Born expressions 2.2-2.3, predominantly originating from the running of α, can be easily accounted for by parameterizing that expression in terms of G_μ and M_W instead of α and $\sin^2\vartheta_W$; using the relation:

$$\sin^2\vartheta_W = \frac{\pi\alpha}{\sqrt{2}\, G_\mu\, M_W^2}$$

we see that the dominant t-channel neutrino exchange contribution to the Born cross section (eq. 2.3) depends only on the parameters M_W and G_μ.

QCD corrections

A complete calculation of the QCD corrections is not presently available. In a first approximation these corrections are taken into account by adding a so-called naive correction factor to the W hadronic decay:

$$\Gamma_{\mathrm{W}\to\mathrm{q\bar{q}}} = \Gamma^{\mathrm{EW}}_{\mathrm{W}\to\mathrm{q\bar{q}}} \cdot \left(1 + \frac{\alpha_s(M_W^2)}{\pi}\right)$$

where Γ_W is the width without any QCD correction (EW stands for electroweak), and where α_s is the QCD strong coupling constant whose value at $\sqrt{s} = M_W$ is $\alpha_s(M_W^2) \simeq 0.123$ [28].

As a result also the total width of the W changes in:

$$\Gamma^{\mathrm{tot}}_{\mathrm{W}} = \Gamma^{\mathrm{tot,EW}}_{\mathrm{W}} \cdot \left(1 + \frac{2\alpha_s(M_W^2)}{3\pi}\right)$$

---

[7] Fermi coupling constant whose value is well known from the muon decay time measurement.

and consequently the total cross section is increased and the effective branching ratios of W to hadrons and leptons are changed, as we will see in section 2.1.4. The main diagram responsible of the QCD corrections is shown in fig. 2.9.

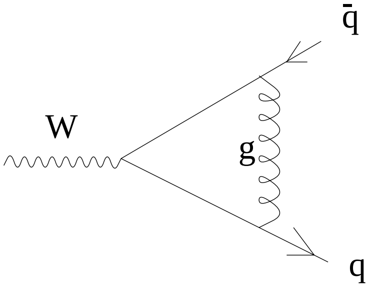

Figure 2.9: Main diagram of the QCD correction at Γ_W.

Interconnection effects

At LEP2 energies the distance between the W^+ and W^- decay vertices is smaller than 0.1 fm, less than the typical hadronization distance which is about 1 fm. Therefore if the Ws decay hadronically, the decay products may interact with each other during the hadronization process; the effects due to these interactions are called "interconnection effects". We can distinguish two different physical effects: colour reconnection and Bose-Einstein correlation.

In the first of these effects, the colour reconnection, the possibility of the hadronization process between two quarks coming from different Ws, as shown in fig. 2.10, is taken into account.

Several models, very different from each other, have been proposed to describe this effect [43, 44], that is supposed to be important for the measurement of M_W, but should be negligible for the cross section measurement [44].

The Bose-Einstein (BE) effect is related to the possibility that, if both Ws decay hadronically, coherence effects between identical low-momentum bosons (mostly pions) coming from different Ws may be present, due to BE correlation. Since the BE effect favours production of identical bosons close in phase space, one would expect the softest particles from each W to be dragged closer to each other, thus reducing the momentum of the Ws.

2.1.4 The width of the W boson

The width of the W boson is a very important parameter for the study of W pair production at LEP2. It determines the magnitude of the off-shell cross section (eq. 2.4) and the branching ratios for the different final states.

The Γ_W measurements pre-LEP2 have a large error: $\Gamma_W = 2.08 \pm 0.07$ GeV [45], while theoretically it can be computed with high precision.

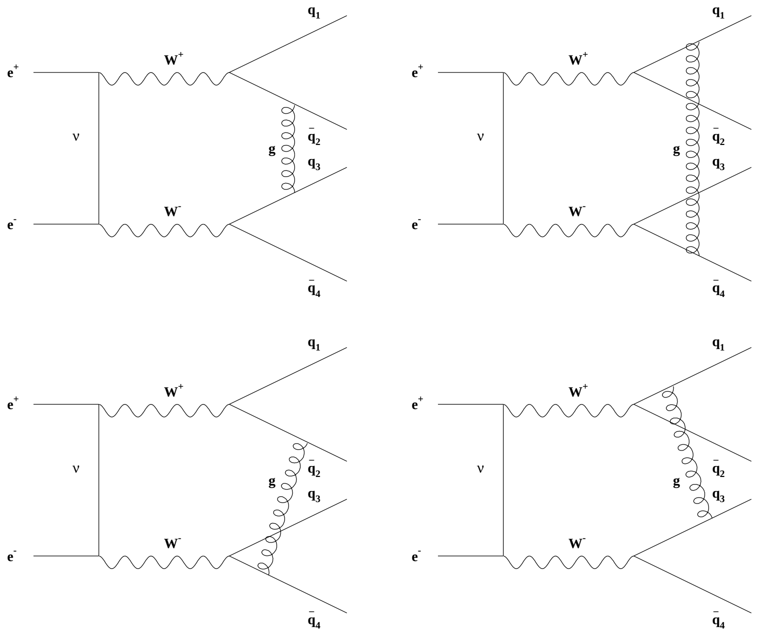

Figure 2.10: Diagrams representing the colour reconnection.

The W boson width is the sum of the partial widths for the hadronic and leptonic decays for which the sum of the decay product masses is less than the W boson mass. This excludes all decays involving the top quark [28]:

$$\Gamma_W = \sum_{\substack{i=1,2\\ j=1,2,3}} \Gamma_{W_{\mathrm{u_i d_j}}} + \sum_{i=1,2,3} \Gamma_{W_{\ell_i \nu_i}}$$

The masses of fermions in the decay of an on-shell W boson are small compared to M_W. Therefore these masses are neglected in the calculation of the partial widths.

The individual hadronic and leptonic contributions can be written, at lowest order, in the following way:

$$\Gamma^{\mathrm{Born}}_{W_{f_i f_j}} = N_c^f \, \frac{\alpha}{6} \, \frac{M_W}{2\sin^2\vartheta_W} \, |V_{ij}|^2$$

where N_c^f is the colour factor, which is 3 for hadronic decays and unity for leptonic decays; V_{ij} is the CKM[8] matrix element ij for the quark sector ($V_{ij} = \delta_{ij}$ for the leptonic sector).

In the formulae given above, α and $\sin^2\vartheta_W$ are sensitive to the electroweak corrections. In the improved Born approximation these corrections are taken into account by rewriting the widths in terms of G_μ and M_W. In the hadronic channel, QCD corrections are taken into account by the naive factor (section 2.1.3).

The W boson partial and total widths can then be expressed as:

$$\Gamma_{W_{\ell_i \nu_i}} \quad = \quad \frac{G_\mu M_W^3}{6\sqrt{2}\pi}$$

---

[8] Cabibbo-Kobayashi-Maskawa.

$$\Gamma_{W_{\mathrm{u}_i\mathrm{d}_j}} = \frac{G_\mu M_W^3}{2\sqrt{2}\pi}|V_{ij}|^2\left(1+\frac{\alpha_s(M_W^2)}{\pi}\right)$$

$$\Gamma_W = \frac{3G_\mu M_W^3}{2\sqrt{2}\pi}\left(1+\frac{2\alpha_s(M_W^2)}{3\pi}\right)$$

The comparison of the improved Born approximation with the complete set of corrections shows an agreement better than 0.6% (tab. 2.2). The effect of finite fermion masses is less than 0.3%.

	IBA $m_f = 0$	Complete $m_f \neq 0$	Branching Ratio
$\Gamma_{\mathrm{W}\to\mathrm{e}\nu_\mathrm{e}}$	0.2262	0.2255	0.1083
$\Gamma_{\mathrm{W}\to\mu\nu_\mu}$	0.2262	0.2255	0.1083
$\Gamma_{\mathrm{W}\to\tau\nu_\tau}$	0.2262	0.2253	0.1082
$\Gamma_{\mathrm{W}\to\mathrm{had}}$	1.4104	1.4054	0.6751

Table 2.2: W decay widths in the Improved Born Approximation and nil mass of fermions compared with the results obtained applying all the corrections and non nil fermion masses. The Branching ratios are computed with the complete set of corrections.

Once the branching ratios (BR) are known, also the decay fraction (DF) of the different W pair decay channels can be found[9]:

$$\begin{aligned}\mathrm{DF}_{\mathrm{WW}\to\mathrm{q\bar{q}q\bar{q}}} &= \left(\mathrm{BR}_{\mathrm{W}\to\mathrm{q\bar{q}}}\right)^2\\ \mathrm{DF}_{\mathrm{WW}\to\mathrm{q\bar{q}}\ell\bar{\nu}} &= 2\left(\mathrm{BR}_{\mathrm{W}\to\mathrm{q\bar{q}}}\right)\left(\mathrm{BR}_{\mathrm{W}\to\ell\bar{\nu}}\right)\\ \mathrm{DF}_{\mathrm{WW}\to\ell\bar{\nu}\bar{\ell}\nu} &= \left(1-\mathrm{BR}_{\mathrm{W}\to\mathrm{q\bar{q}}}\right)^2\end{aligned}$$

In table 2.3 these results are compared with a naive determination[10].

2.1.5 Simulation steps of the $\mathrm{e}^+\mathrm{e}^- \to \mathrm{WW} \to$ 4f process

As already mentioned the study of complex processes, like the LEP2 ones, is performed using numerical simulations. These programs allow the calculation of complex quantities (like cross sections, angular distributions, etc.) and also allow the generation of simulated events which will be processed in the same identical manner of real events.

The simulation of the $\mathrm{e}^+\mathrm{e}^- \to \mathrm{WW} \to$ 4f process, as the majority of other LEP2 processes, is carried out in four steps, as shown in fig. 2.11.

I) The two Ws are produced in the $\mathrm{e}^+\mathrm{e}^-$ annihilation, and each decays in a quark or lepton pair. At this level some ISR photons may be radiated. This phase is well described by the electroweak theory.

---

[9] The first two come from the binomial statistics, the third from unitarity.

[10] Neglecting the radiative corrections, the W decay width in any kinematically possible (no top quark) isospin doublets are equal; since these doublets are 9, 3 leptonic and 6=(2 doublets)x(3 colours) hadronic, it follows that $\mathrm{BR}_{\mathrm{had}}$=2/3 and $\mathrm{BR}_{\mathrm{lep}}$=1/3.

W^+W^- decay channel	Decay Fraction corrected	naive
$q\bar{q}q\bar{q}$	45.6%	$\left(\frac{2}{3}\right)^2$=44.4%
$e\bar{\nu}q\bar{q}$	14.6%	$2\cdot\left(\frac{2}{3}\right)\cdot\left(\frac{1}{9}\right)$=14.8%
$\mu\bar{\nu}q\bar{q}$	14.6%	$2\cdot\left(\frac{2}{3}\right)\cdot\left(\frac{1}{9}\right)$=14.8%
$\tau\bar{\nu}q\bar{q}$	14.6%	$2\cdot\left(\frac{2}{3}\right)\cdot\left(\frac{1}{9}\right)$=14.8%
$\ell^-\bar{\nu}\ell^+\nu$	10.6%	$\left(\frac{1}{3}\right)^2$=11.1%

Table 2.3: Corrected and naive decay fractions for the different final states of W decays.

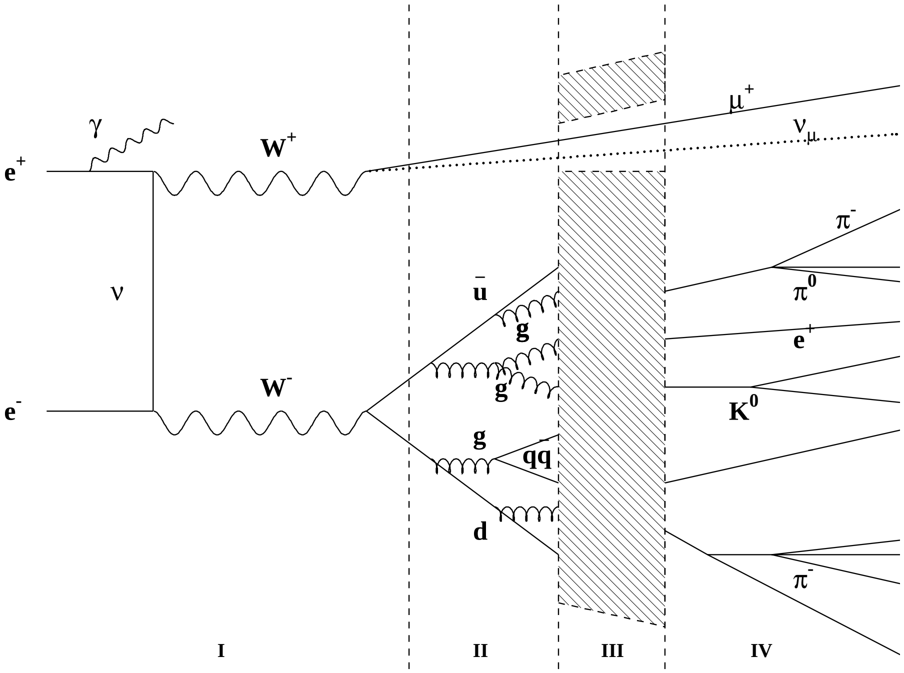

Figure 2.11: Schematic representation of the different steps of the $e^+e^- \rightarrow W^+W^- \rightarrow \mu^+\nu_\mu q\bar{q}$ simulated process.

II) In the second phase gluons and photons are radiated by the primary quarks. This process is described by QCD theory and in particular by the Altarelli-Parisi equations.

III) In the third step the coloured partons are glued to form hadrons; this phase is called hadronization or fragmentation and consists of QCD non perturbative effects that can only be described by phenomenological models.

IV) In the last phase the non stable hadrons, created in the fragmentation phase, decay in long lived particles are seen by the detector.

The programs most used by the LEP experiments to simulate the parton shower and hadronization are: JETSET [46], ARIADNE [47] and HERWIG [48].

2.1.6 Four fermion processes

Since the Ws cannot be detected, the only observable signal is a four fermion final state. As already mentioned, at lowest order, there are several diagrams that have the same final state of the CC03 graphics. For example there are 20 diagrams that contribute to the process $e^+e^- \rightarrow e^-\bar{\nu}_e u\bar{d}$, as shown in fig. 2.12.

Table 2.4 shows the number of Feynman diagrams for the four fermions final states with flavours such that they could be produced by W pair intermediate states.

	$\bar{d}u$	$\bar{s}c$	$e^+\nu_e$	$\mu^+\nu_\mu$	$\tau^+\nu_\tau$
$d\bar{u}$	43	11	20	10	10
$e^-\bar{\nu}_e$	20	20	56	18	18
$\mu^-\bar{\nu}_\mu$	10	10	18	19	9

Table 2.4: Number of Feynman diagrams for W-pair produced four-fermion final states.

If the produced final state consists of particle-antiparticle pairs, as can happen in the leptonic and hadronic channel, the final state can also be obtained through γ or Z intermediate states. Moreover it should be mentioned that QCD diagrams, involving an intermediate gluon, contribute in the case of final states consisting of two quark-antiquark pairs.

All these "4f" diagrams cannot be considered separately from the "CC03" graphics because of the interference between each other. The increased number of diagrams determines a change in the total cross section and in the kinematical event distributions; however the contribution of diagrams different from CC03 is usually limited to particular regions of the phase space, so that their contribution to the cross section is decreased after the application of the cuts used for the signal selection.

In our case, since we are interested in W pair production, our signal is represented by a four fermion final state that comes from the decay of a W pair; in other words we want to measure only the CC03 cross section even if the "real" physical process is described by

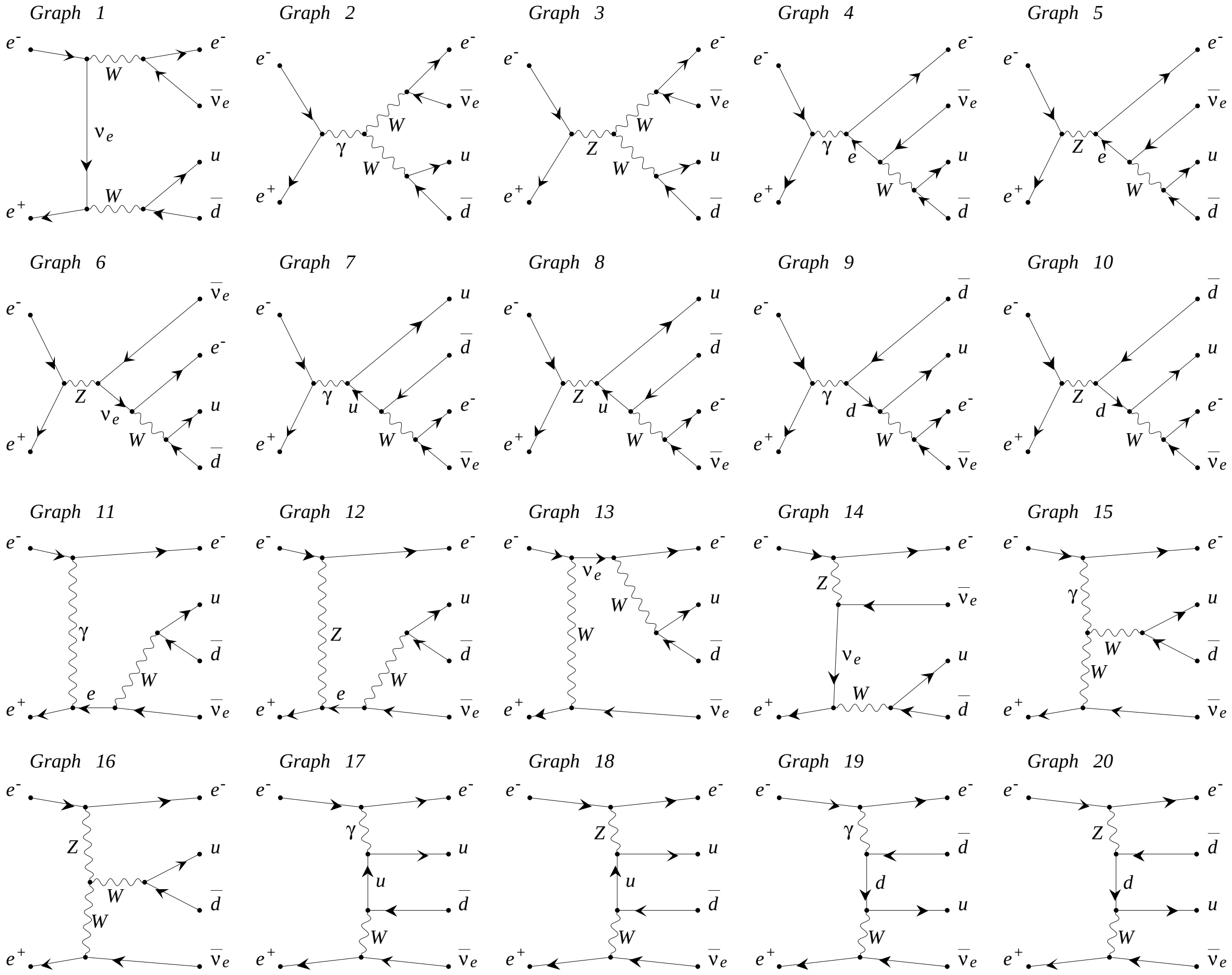

Figure 2.12: The twenty charged current diagrams (CC20) describing the process $e^+e^- \rightarrow e^-\bar{\nu}_e u\bar{d}$; the first three are the CC03 diagrams with two W resonant bosons.

the CC03 plus all the other graphs. We therefore need to define a procedure to subtract the effect of the other 4f diagrams.

A similar problem was faced in the measurement of the cross section of the $e^+e^- \rightarrow Z \rightarrow e^+e^-$ at LEP1, where the process with the γ-exchange in the t-channel, which has the same final state, had to be subtracted [34].

On the other hand the 4f cross section is well defined, but it is neither easily measurable, nor precisely calculable. In fact, for example, in the process $e^+e^- \rightarrow e^+e^-q\bar{q}$, the $\cos\vartheta$ distribution of the electron has a peak at unity; this means that experimentally, in most of the events the electron escapes detection along the beam pipe, while, theoretically, the calculation of the cross section in this angular region is really delicate and needs to take into account the masses of the electron to avoid the singularity at $\cos\vartheta = 1$; moreover the calculation is very computing intensive.

For this reason, usually, cuts at low polar angles are used in the Monte Carlo events generation and, as a consequence, the theoretical 4f cross section varies depending on the cuts applied.

The corrections used to subtract the effect of the 4f diagrams different from the CC03 ones are computed using Monte Carlo generated CC03 and 4f events and will be explained in detail in the following.

Experimental definition of CC03 cross section

Usually for a measurement of a cross section σ, one needs to determine the number of events observed in data, N^{obs}, using a selection procedure; then one needs to evaluate the expected contribution from background, N_{bkg}, applying the same selection procedure to a sample of MC simulated events, whose final state is similar to the signal one.

Let ε be the signal selection efficiency, estimated on a signal MC sample, then:

$$\sigma = \frac{N^{obs} - N_{bkg}}{\varepsilon \cdot \mathcal{L}}$$

where $\mathcal{L}$ is the luminosity (see section 1.2.7).

As observed before, in our case the situation is more complicated; for example, the process $e^+e^- \to ZZ \to u\bar{u}d\bar{d}$ has the same final state of $e^+e^- \to WW \to u\bar{u}d\bar{d}$, and it has to be included in the 4f calculation of the WW signal. But if we want to measure the CC03 cross section, the contribution of $ZZ \to u\bar{u}d\bar{d}$ and its interference with $WW \to u\bar{u}d\bar{d}$ has to be evaluated and subtracted from N^{obs}.

Two different approaches exist to take into account of the contribution at N^{obs} of the 4f diagrams, different from CC03, and their interference with the latter: the additive and the multiplicative approach.

The additive approach

The most intuitive way is to treat such a contribution as any background, and simply subtract it from N^{obs}, so neglecting the interference with the signal. Let us call $N_{4f}^{\overline{CC03}}$ the number of four fermions events given by all diagrams except the CC03 ones; it can be computed as:

$$N_{4f}^{\overline{CC03}} = \mathcal{L}\left(\varepsilon_{4f}\,\sigma_{4f}^{MC} - \varepsilon_{CC03}\,\sigma_{CC03}^{MC}\right)$$

where ε_{4f} and ε_{CC03} are the selection efficiencies evaluated on the Monte Carlo 4f and CC03 simulated events, and σ_{4f}^{MC} and σ_{CC03}^{MC} the relative cross sections. Let me observe that both ε_{4f} and σ_{4f}^{MC} depend on the phase space cuts applied at generation level, but, if the experimental cuts are tighter than the MC ones, then the product $\varepsilon_{4f}\sigma_{4f}^{MC}$ does not depend on the generator cuts.

In this approach the CC03 cross section is:

$$\sigma_{CC03} = \frac{N^{obs} - N_{bkg} - N_{4f}^{\overline{CC03}}}{\varepsilon_{CC03} \cdot \mathcal{L}} \tag{2.6}$$

where N_{bkg} represents events given by other physical processes than 4f.

It should also be observed that, for some final states, the destructive interference of 4f and CC03 diagrams can produce a negative value for $N_{4f}^{\overline{CC03}}$.

The multiplicative approach

In the multiplicative approach the CC03 cross section is obtained correcting the measured 4f cross section by the ratio $\sigma^{MC}_{CC03}/\sigma^{MC}_{4f}$:

$$\sigma_{CC03} = \frac{N^{obs} - N_{bkg}}{\varepsilon_{4f} \cdot \mathcal{L}} \cdot \frac{\sigma^{MC}_{CC03}}{\sigma^{MC}_{4f}} \tag{2.7}$$

Also this correction depends on the 4f quantities only through the product $\varepsilon_{4f}\sigma^{MC}_{4f}$ and it is therefore independent from the 4f generator phase space cuts.

These two approaches produce exactly the same result only when the experimental cuts are tuned to completely eliminate the contribution of the diagrams different from CC03, that is when $\varepsilon_{4f}\sigma^{MC}_{4f} = \varepsilon_{CC03}\sigma^{MC}_{CC03}$.

It will be interesting to compare the results of these two approaches later in the analysis developed in this thesis.

I will discuss now the other physical processes that occur at LEP2 (see tab. 2.1) and which may constitute a background source to the W pair selection.

2.2 Background processes

2.2.1 Two fermion production

At LEP2 quark and lepton pair production remains one of the dominant processes. As shown in fig. 2.1(b), quark pair production has a cross section larger than the WW process, and is even larger after the inclusion of initial state radiation (ISR).

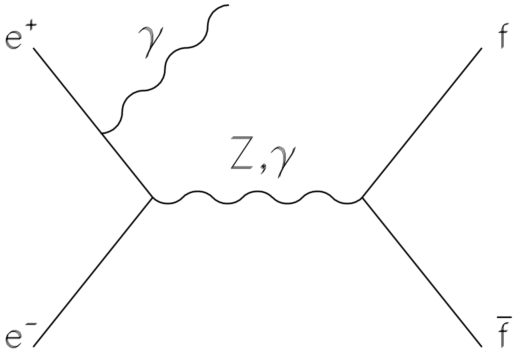

Figure 2.13: Two fermion production diagrams with ISR photon.

At LEP1 energies the $e^+e^- \to Z/\gamma \to f\bar{f}$ process (fig. 2.13) is dominated by the Z resonance. Since the centre of mass energy is close to the Z boson mass, the initial state radiation is strongly suppressed, the angle between the two fermions in space (acollinearity) is close to 180° and the visible mass of the event, calculated from the sum of the energies and momenta of all objects, is close to the Z boson mass.

At energies far above the Z resonance peak the phenomenology of this process changes; two different situations can arise.

In the first configuration the $f\bar{f}$ pair exhibits an acollinearity close to 180° and the visible mass of the event is about equal to the centre of mass energy. This is the configuration where none, or a small energy, photon is radiated and is characterized by the exchange of a very off-mass shell Z or photon in the s-channel.

The second configuration is when a photon is emitted in the initial state with an energy returning the effective centre of mass energy of the $f\bar{f}$ pair close to the Z boson resonance energy; this situation is referred to as "radiative return to the Z". In this case the invariant mass of the $f\bar{f}$ pair is again close to the Z boson mass.

If the initial state radiation is emitted in the longitudinal direction with little transverse momentum, it will escape undetected in the beam pipe below the acceptance of the detector; the $f\bar{f}$ system recoils against the photon and is therefore boosted in the direction of the beam axis. The angle between the two fermions in space is therefore significantly less than 180°, the exact values depend on the LEP energy and the decay angle relative to the boost direction. The angle between the two fermions in the transverse plane (acoplanarity), effectively ignoring the boost in the z direction, is close to 180°. Additionally the polar angle of the missing momentum direction, calculated from the vector sum of the momenta, is small (the missing momentum direction points in the direction of the beam axis).

If the photon is emitted with a large transverse momentum, it will be detected. In this case no missing energy is present, neglecting the effects of the tau decay and the semileptonic decay of heavy quarks.

Electron pair (Bhabha) production is a special case, because a third production diagram is present, the t-channel photon exchange (fig. 2.14), which gives the dominant contribution to the total cross section[11].

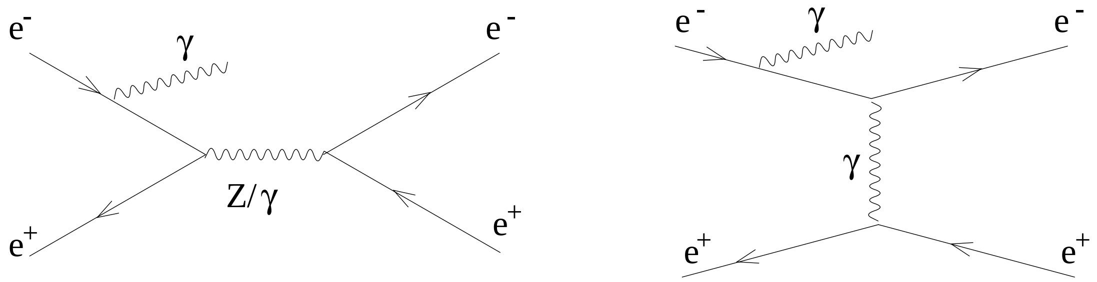

Figure 2.14: The three diagrams that contribute, at lowest order, to the Bhabha process.

In the t-channel dominated processes the cross section changes only slowly with the centre of mass energy and the initial state radiation is suppressed; consequently the electron pair is produced with acollinearity and acoplanarity close to 180°.

In the work for this thesis the quark pair production processes have been simulated with PYTHIA [49], the Bhabha process with BHAGENE [50] (which allows the emission of two bremsstrahlung photons), the muon and tau events with KORALZ [51] (which uses

---

[11] The t-channel Z exchange is negligible respect to the t-channel γ exchange, however it has to be taken into account for an exact calculation.

the YFS2 [52] generator to simulate ISR, and the TAUOLA [53] library to simulate the τ decay taking into account the spin effects).

The cross sections calculated with these generators for a centre of mass energy of 183 GeV are listed in tab. 2.1.

Fig. 2.1(a) shows the two-fermion cross section at LEP1 and LEP2 energies.

2.2.2 $\gamma\gamma$ processes

The $\gamma\gamma$ processes are characterized by a $f\bar{f}$ system produced through the interaction of two bremsstrahlung photons emitted by the incoming electron and positron. They can be divided in leptonic (fig. 2.15) and hadronic (fig. 2.16) final states.

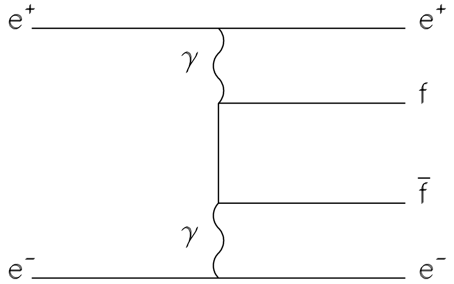

Figure 2.15: Multiperiferical diagram for the $\gamma\gamma$ process $\mathrm{e}^+\mathrm{e}^- \to \mathrm{e}^+\mathrm{e}^- f\bar{f}$.

These events are characterized by a low polar angle electron and positron, and in the majority of the events both escape undetected below the detector acceptance ("untagged").

An event is classified as tagged when either the electron or the positron is detected. These events, although rare, are the ones that may constitute a background to the W pair signal; in fact if the electron is raised at high polar angle, it means that it has emitted an energetic photon which has, in the $\gamma\gamma$ interaction, enough energy to produce, for example, two energetic jets; the positron escaped in the beam pipe represents a missing energy source. This event, therefore, can be mistaken for a $\mathrm{e}^+\mathrm{e}^- \to \mathrm{e}^-\bar{\nu}_e\mathrm{q}\bar{\mathrm{q}}$ event.

The leptonic final states are well described by the DIAG36 generator, that includes the calculation of 36 Feynman diagrams. Apart from the diagram in fig. 2.15, it includes all the QED bremsstrahlung, conversion and annihilation processes [54].

For the hadronic final states we have used PYTHIA and PHOJET [55] generators, which use phenomenological models. For example in the VMD (Vector Meson Dominant) process in fig. 2.16(b) the transformation of the photons in virtual mesons and their consequent strong interactions is not described by perturbative QCD, and phenomenological model are needed. Probably due to the low precision of these models, these generators are often, as we will see, in disagreement with data for several of the experimental variables.

Moreover, since PYTHIA only simulates the photon interactions, without covering the full process of photon radiation off the electrons, it follows that the electron and positron polar angular distribution is mistaken, since these particles are always kept at low polar

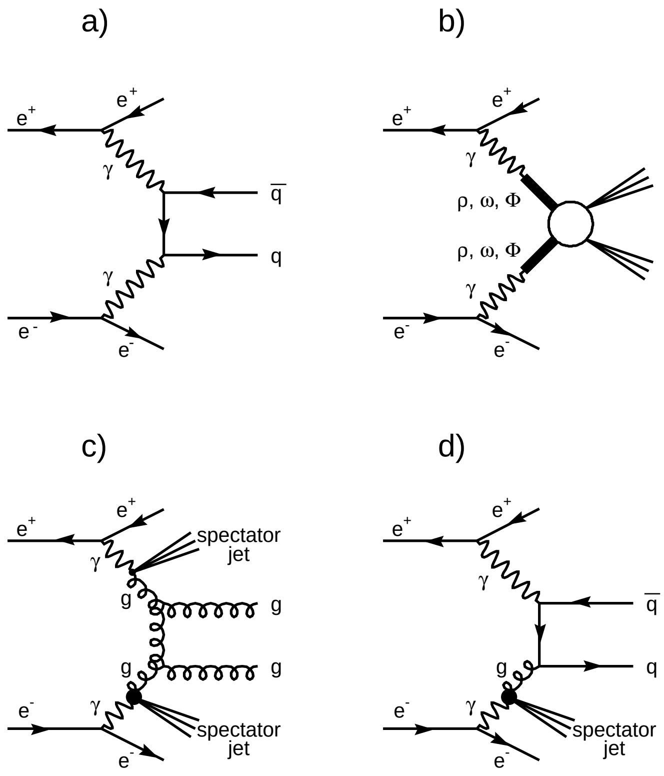

Figure 2.16: Main diagrams for the $e^+e^- \rightarrow e^+e^-q\bar{q}$ process: (a) the direct process (QED), (b) the VMD (Vector Meson Dominant) process and (c-d) the anomalous or QCD processes.

angles. If one is interested in the possibility that the electron or positron could be emitted at high polar angle, then the PHOJET generator should be preferred.

Since the $\gamma\gamma$ cross section increases dramatically as the mass of the $f\bar{f}$ pair decreases, a minimal invariant mass is usually required for the $f\bar{f}$ system at generator level. This is because only a limited amount of Monte Carlo simulated events can be generated, due to the limited CPU time, and therefore this generator cut is necessary to ensure a statistically significant background estimate.

The cross section reported in table 2.1 has been calculated with a cut of 15 GeV on the $q\bar{q}$ invariant mass.

2.2.3 Other processes

In order to complete the discussion of the processes listed in table. 2.1, we are now going to briefly introduce the Z pair production process and the so-called “single W” and “Zee” processes.

As shown in fig. 2.1(a) at a centre of mass energy over the threshold of the Z pair production, the process shown in fig. 2.17 begins to become important.

In particular, it should be observed, that when both the Zs decay hadronically, the 4

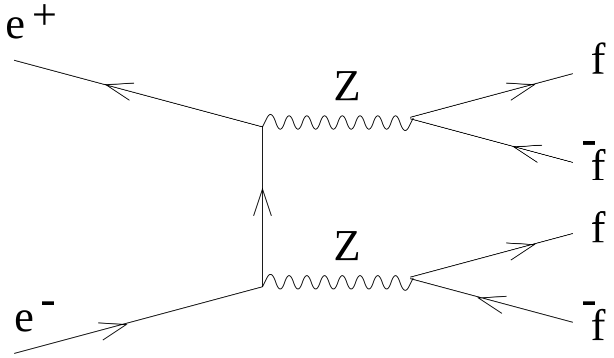

Figure 2.17: Diagram representing the process with two resonant Zs, kinematically possible at $\sqrt{s} \geq 2\,\mathrm{M_Z}$.

jet final state is topologically indistinguible from the $\mathrm{e^+e^-} \to \mathrm{WW} \to \mathrm{q\bar{q}q\bar{q}}$ process, as it has already been discussed in section 2.1.6. On the other hand, when one or both Zs decay leptonically, the ZZ process may constitute a background source to the W semileptonic and leptonic channels if one or two leptons escape undetected.

The single W process (fig. 2.18(a)) can hardly constitute a background source to the W analysis, since the electron in the final state goes often undetected at low polar angle, while the Zee process (fig. 2.18(b)) can be dangerous for the semileptonic process $\mathrm{e\bar{\nu}q\bar{q}}$ when the Z decays hadronically and the outgoing electron, remaining in most cases at low polar angles, remains undetected and is mistaken for a neutrino.

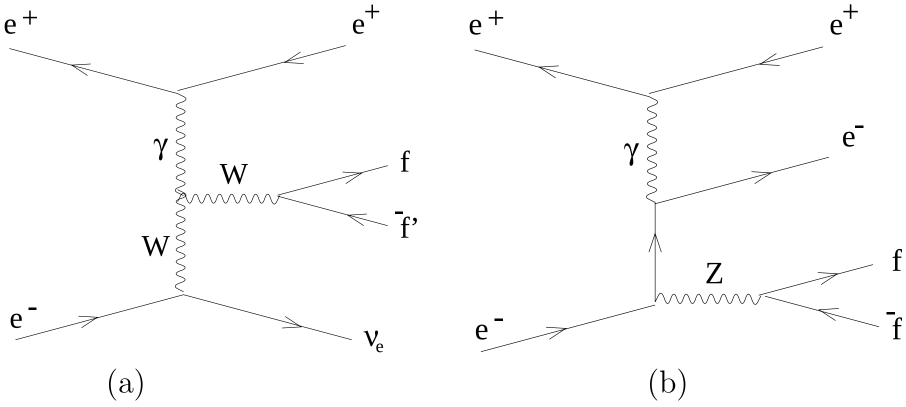

Figure 2.18: Diagrams representing the (a) “single W” and (b) “Zee” processes.

Chapter 3

Data analysis

As in any physics field, in high energy physics it is interesting to compare the results of a measurement with the prediction of the theory. As we have seen in section 1.2 the experimental setup used is very complex and the only sign left by a physical process, a e^+e^- interaction, is the electronic response caused by the passage of the particles into the different sub-detectors. These responses are recorded on-line and are then analysed at a second time (off-line); it is the task of a reconstruction program, called REL3 (Reconstruction of Events in L3), to transform the raw data, that is the electronic signals of the hit wires or the energy deposits in the calorimeters, in higher class objects, directly related to the particles, like tracks, bumps, clusters etc., that are more easily used for the physics analysis.

On the other hand we want to compare these results with the prediction of the theory, but, since the complexity of the experimental apparatus, the analytical prediction of such measurements is impossible; therefore simulations are used.

We have already discussed, in chapter 2, the large use of Monte Carlo techniques for the generation of physical process events; in a subsequent step, also the response of the detector to these generated events is simulated using Monte Carlo techniques. SIL3 (SImulation in L3) is the program that performs this task in L3. The output of SIL3 has the same structure of the raw data and can be processed by the same program, REL3, used for real data; in this way we can directly compare the simulated reconstructed objects with the real ones, that means comparing the results of a measurement with the theory prediction. However usually the reconstructed objects of both types are further processed in order to identify quantities with a greater physical interest, like number of different type particles, jets, topological variables, etc. This is the step usually called data analysis, where all the reconstructed quantities are used to perform the final measurement, like a cross section.

In fig. 3.1 the two parallel routes that finally converge in the data analysis are shown.

Let's now discuss in more details the simulation and reconstruction programs.

3.1 L3 detector simulation

As already mentioned the SIL3 program simulates the interaction of the generated particles with the detectors and the subsequent electronic response of the detector to these

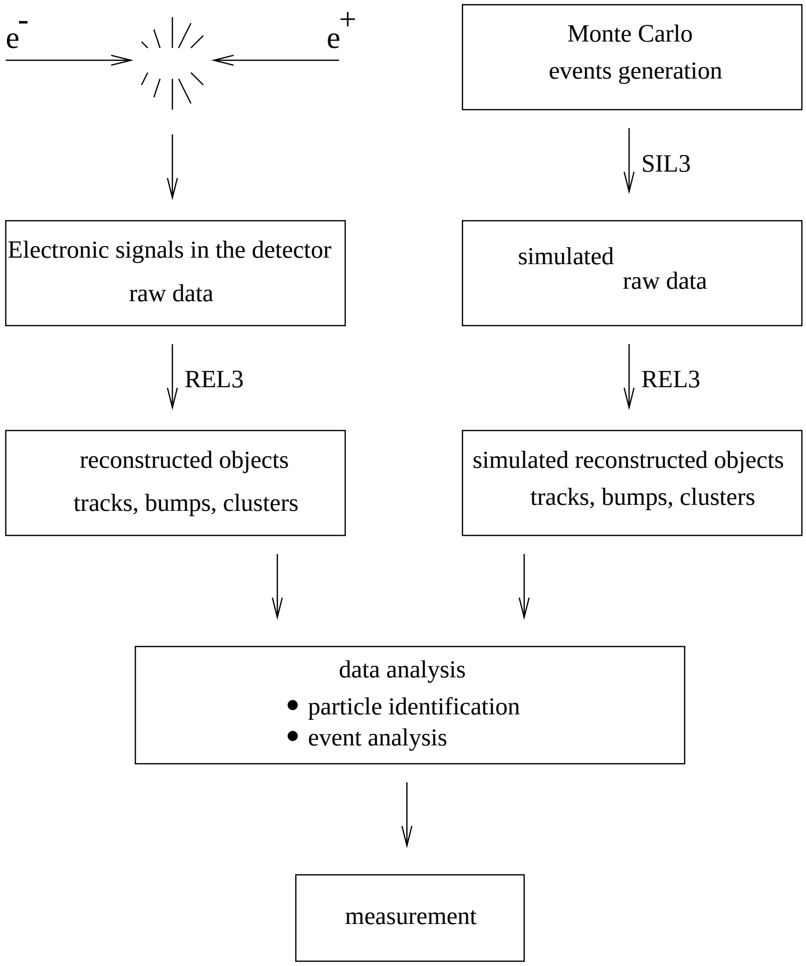

Figure 3.1: Schematic representation of the processed events from generation (collision or Monte Carlo) to the measurement result.

interactions. SIL3 first defines the geometry of the detectors, their chemical composition and simulates the magnetic field in the detectors; in a second step it uses the GEANT [56] program to simulate the interaction of the particles with the experimental apparatus; in particular GEANT takes care of the decay of the instable particles (like $K^{\pm}$ and K^0), the energy lost through the multiple scattering, the creation of e^+e^- pairs, etc. The simulation is very complex since it takes into account all the interactions of the secondary particles in the shower produced by the interaction of the primary particles with the detector material. The hadronic interaction processes are simulated by the GHEISHA [57] program, nested inside GEANT. Moreover SIL3 casually redefines the interaction point position to reproduce the same distribution observed in the data (the uncertainty on the interaction vertex is due to the finite dimension of the bunches).

In the last step the simulated energy deposits are converted in units of the electronic readout, that is in ADCs or TDCs counts; these have the same information format produced by real data, as recorded on-line.

In the so-called “ideal detector simulation” it is assumed that all the different parts of the detectors are properly working at full efficiency. In real life this seldom happens. It can happen that some electronic readout channels, or some high voltage supplies have problems during a data taking run[1]. These informations, related to the history of the L3 detector, are recorded in a database called DBL3 which is then used to perform a "real detector simulation". To this end, the sample of generated events is divided in runs proportionally to their integrated luminosity; then each sample uses the informations written in the L3 database to reconstruct the simulated event with the real detector informations. For instance, the simulation of an event with a hadronic shower which points towards a HCAL tower without high voltage takes into account this inefficient detector part.

The database DBL3 is composed of seven parts relative to the different sub-detectors and other two relative to the trigger and the run control. Each contains the geometry of the detectors, on-line information as the BGO temperature, BGO pedestals, the TEC sectors high voltage and off-line informations as the calibrations constants of the TEC and BGO, the number of BGO dead crystals, etc.

3.2 Event reconstruction

The reconstruction program REL3 takes care of transforming the recorded informations coming from tens of thousand electronic readout channels (either simulated or real) in more physical quantities. REL3 first reconstructs the objects in the sub-detectors (like energy clusters in the BGO or tracks in the TEC), then tries to combine these objects in order to reconstruct more complex quantities directly related to particles.

In this section I will define in more details the different reconstructed objects.

Tracks. The tracks are reconstructed by fitting the TEC hit wires and SMD strips (called simply "hits") with a circumference in the $r - \varphi$ plane; thus the track curvature radius R is extracted and the transverse p_T momentum computed ($\mathrm{p}_T \propto R$). Moreover also the distance, in the $r - \varphi$ plane, of the track from the interaction vertex (DCA) is calculated. Informations about the ϑ polar angle are derived from the hits in the Z chamber, from the SMD hits, and, if $(\vartheta, \pi - \vartheta) \leq 35^\circ$, from the number of the outermost TEC wire hit; in fact, since the TEC wires are parallel to the beam direction, from the knowledge of the number of hit wires it is possible to derive the ϑ polar angle (this determination method is called "flange information").

The main parameters relative to a track are:

- the number of hits used in the fit (the maximum is 62 in the TEC and 3 in SMD);
- the span of the track, that is the distance between the first and the last hit wire;
- the DCA;
- the transverse momentum p_T;

---

[1] The data taking period is divided in runs, that correspond roughly to the amount of data that can be recorded on a tape.

- the polar angle ϑ.

Bumps in BGO. Bumps in BGO are formed gathering together crystals with an energy greater than 10 MeV around a local maximum crystal with an energy of, at least, 40 MeV. For each bump, so formed, the centre of gravity and the sums Σ_9 and Σ_{25} of the energies deposited in a 3x3 and 5x5 crystal matrix are constructed (an electromagnetic particle, as an electron or a photon, delivers 91% of its energy in a 3x3 crystal matrix and 97% in a 5x5 crystal matrix). Once these sums are corrected for the lateral energy loss, the ratio Σ_9/Σ_{25} is calculated; it represents an important variable to discriminate electromagnetic from hadronic particles.

Another important variable to evaluate the bump electromagneticity is χ^2_{em}; it is the result of the comparison between the event energy distribution deposited in a 3x3 crystal matrix and the expected one for an electromagnetic particle.

The shape of the bump itself is characterized by another variable called skewness, that represents the ratio between the two axes of the ellipse computed from the second momenta of the energies delivered in the crystals.

The main parameters used to describe a bump are then:

- the number of crystals the bump is made of;
- the bump energy;
- the most energetic crystal energy;
- Σ_9, Σ_{25} and Σ_9/Σ_{25} corrected;
- χ^2_{em} and skewness.

HCAL hits. HCAL clusters are formed by an algorithm that matches together the energy deposits in the chambers of a tower using their ϑ and φ informations.

The energy deposits in the hadron calorimeter due to the uranium noise (see section 1.2.4) of several GeV per event are almost completely eliminated by such algorithm.

ASRC. The local energy deposits in the electromagnetic and hadronic calorimeter can be joined together to form clusters (ASRCs)[2] if their angular coordinates, ϑ and φ, are close enough. The most interesting quantities related to a cluster are its energy, the angular coordinates and the energy contribution from the different detectors (BGO, HCAL, EGAP).

Muons. Muons are identified in the muon chambers (sec. 1.2.5). The tracks in these chambers can sometimes be produced by hadronic showers that are not completely stopped by the hadron calorimeter, called "punch-through". At least two P segments[3] are needed to measure the track curvature and, as a consequence, the transverse momentum; the polar angle ϑ, measured by the Z chambers, allows the determination of the muon momentum.

---

[2] **A** **S**mall **R**esolvable **C**luster.

[3] P segment means a group of hit wires in a P chamber.

The hits belonging to a muon track are, in a second step, fitted together with the TEC and SMD hits to form a higher class object, representing a muon coming from the vertex interaction, called AMUI; as for the TEC tracks, the distance between the AMUI and the vertex interaction is called DCA.

The main quantities relative to a muon track are: the number of segments used for track fitting, the momentum, the polar coordinates, the DCA and the muon time of flight, measured by the scintillators.

REL3 also has a graphical event representation, as shown in the $e^+e^- \rightarrow e\bar{\nu}q\bar{q}$ event in fig. 3.2, where the tracks are represented by lines, the energy deposits by towers in the BGO and by squares in the HCAL; the dimension of the towers and squares is proportional to the energy deposited. In this figure the isolated electron is represented by a track in the TEC matched with a bump in the BGO, and the two coplanar jets are constituted by narrow bundles of hadronic particles pointing roughly to the same direction.

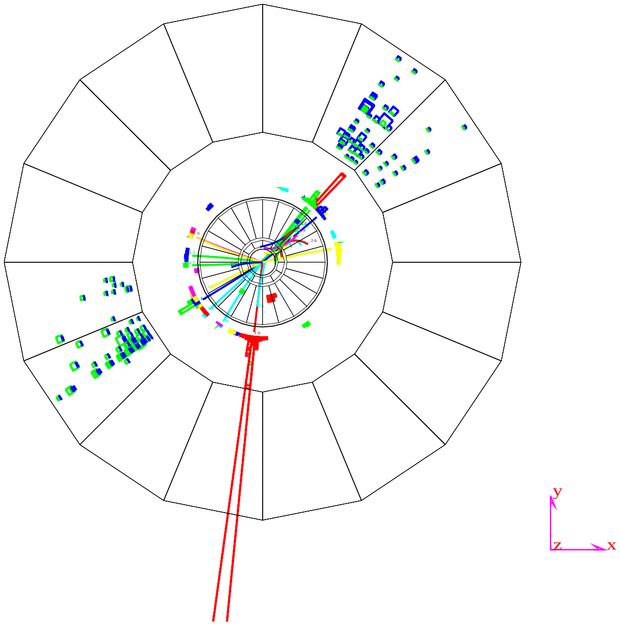

Figure 3.2: Graphical representation of a $e^+e^- \rightarrow e\bar{\nu}q\bar{q}$ event at $\sqrt{s} = 183$ GeV.

The graphic visualization allows, in a first step of the analysis, an easier understanding of the event topology aiding the study of the variable distributions.

Jets. Qualitatively a jet can be defined as a collection of hadrons moving in approximately the same direction, originating from the decay-fragmentation of a "hard" parton. Since we do not understand fragmentation in very high detail it is impossible to describe the exact evolution of a parton into a jet, but within the framework of QCD some explanation as to why the hadrons formed are roughly collinear with the original parton can be ascribed to the confinement property of QCD; when high energetic quarks or gluons tend to separate from each other the increasing strength of the colour field polarizes the vacuum and creates a succession of quark-antiquark pairs, which combine into a narrow jet of hadrons around the original parton direction. The sum of the four momenta of the hadrons is generally referred to as the four momentum of the jet, which is then considered to be a "pseudo-particle" representing the original parton. The average transverse momentum of the hadrons with respect to the jet axis depends very little on the longitudinal energy of the hadrons (it is of the order of 250 MeV), hence higher energies result in narrower and better defined jets.

Quantitatively jets are defined and assembled by a class of algorithms which join together the reconstructed objects in the detectors. All such algorithms are iterative procedures; first a set of objects in the event and a function or "metric" y_{ij} have to be chosen; then for each object pair ij the y_{ij} metric is calculated and the pair ij with the smallest value of y_{ij} is combined into a pseudo-particle which replaces the two objects. The iterative process continues until either the desired number of jets is reached, or the minimum metric y_{ij} between all pairs of jets is larger than a preset cutoff y_{cut}. In the first case the event is characterized by a minimum y_{ij} value, in the second case each event can be classified by the number of jets found.

The different methods used to determine which objects to combine together all reflect the assumption that objects separated by small angles or having low momentum with respect to each other belong to the same original parton. The most used metrics are: JADE [58], LUCLUS [59] and DURHAM [60].

- **JADE metric** :

  $$y_{ij} = \frac{2E_iE_j(1 - \cos\vartheta_{ij})}{E_{\mathrm{vis}}^2} \tag{3.1}$$

  where E_i is the energy of the i-th cluster, and E_{vis} is the visible energy of the event; the use of E_{vis} instead of E_{cm}(centre of mass energy) tends to make the measure less sensitive to detector acceptance corrections.

  The numerator of eq. 3.1 represents the squared invariant mass of the ij pair, in the case where the two particles or clusters are massless. This algorithm suffers the problem that low energy particles that go in opposite directions, have anyway small value of y_{ij}, and so may be tagged to the same jet, even though they probably belong to different partons. For instance, consider two soft gluons i and j, they will have a small value of y_{ij} even if their directions are not close, and the iterative algorithm will combine the soft gluon with each other first, rather than first trying to combine the soft gluons with the high energy particles; the result can be an artificial jet made of soft particles. Therefore JADE is not a good algorithm to determine the jet directions and energies, nevertheless it is known to give a very good agreement between the number of initial partons and the number of jets reconstructed from the hadrons.

- **LUCLUS metric**:

  $$y_{ij} = \frac{|\vec{p_i}| \cdot |\vec{p_j}| \cdot \sin(\vartheta_{ij}/2)}{|\vec{p_i}| + |\vec{p_j}|} \tag{3.2}$$

For small relative angle ϑ_{ij} this metric reduces to:

$$y_{ij} = \frac{|\vec{p}_i \text{ x } \vec{p}_j|}{|\vec{p}_i + \vec{p}_j|}$$

where $\vec{p}_i$ is the momentum of the i-th cluster and "x" represents the cross product. In this limit we see that y_{ij} has the simple physical interpretation as the transverse momentum of either particle with respect to the direction given by the sum of the two particle momenta. On the other hand, when the two particles are back to back, eq. 3.2 is closely related to their invariant mass.

This algorithm forms jets starting with the fastest object in the event, and assigning all objects with transverse momentum less than some arbitrary value to that jet; it then takes the second fastest object not assigned to a jet as a new jet initiator, and so on.

The LUCLUS algorithm is less accurate in the reproduction of parton-jet multiplicities with respect to JADE, but since it starts clustering with the highest momentum object, the found jets are characterized by a high angular and energy resolution.

- **DURHAM metric**:

$$y_{ij} = \frac{2\min(E_i^2, E_j^2)\,(1 - \cos\vartheta_{ij})}{E_{\text{cm}}^2} \tag{3.3}$$

The DURHAM metric is based on the relative transverse momentum of the objects i and j; the numerator of eq. 3.3 has the geometrical interpretation, in the small angle limit, as the squared transverse momentum of the softer particle with respect to the direction of the harder one. If the energy of the two particles are equal it represents their squared invariant mass.

DURHAM, as LUCLUS, algorithm has better performances in the determination of the jet directions and energies, than in reproducing parton-jet multiplicities.

All types of jet algorithms have advantages and drawbacks; the invariant mass type algorithms are generally known to give good parton-jet multiplicities but less accurate energy and angular determination, whereas the transverse momentum based algorithms have a high energy and angular resolution but do not reproduce the parton-jet multiplicities so well.

In this thesis JADE is used to determine the number of jets, once a certain value of the y_{cut} is chosen; whereas LUCLUS and DURHAM are used to reconstruct respectively two and four jets.

In the two jets case, especially at LEP1 where the two jets produced were most likely back to back, a different jet reconstruction technique could be used. First the thrust axis $\vec{n}$ for which the thrust value:

$$T(\vec{n}) = \frac{\sum_i |\vec{p}_i \cdot \vec{n}|}{\sum_i |\vec{p}_i|}$$

is maximized, is determined. The event is then separated in two hemispheres with respect to the thrust axis. Each jet is formed adding the four momenta of all the objects in a hemisphere. However if there are three jets in the event, for instance a gluon radiated off one of the quarks, the algorithm will fail as parts of one jet are divided between the two hemispheres, spoiling the determination of the momentum direction of the original partons.

3.3 Energy calibration in hadronic events

The passage of a hadron particle in the detector is characterized by a track in the TEC, if the particle is charged, a small energy deposit in the electromagnetic calorimeter and the remaining energy in the hadron calorimeter. Sometimes, as already mentioned, part of the shower can reach the muon chambers; moreover electromagnetic particles and muons coming from the decay of unstable hadrons (γ's from π^0, e and μ from B and D mesons) have to be taken into account in the determination of the jet energy.

No detector alone can completely measure the hadrons energy; the TEC, that in principle could measure the momentum of charged hadrons, has neither a good energy resolution, nor a good angular coverage. Therefore the energy deposits in each sub-detectors are properly reweighted in order to optimize the resolution of the energy measurement for hadrons using events whose energy is a-priori well known, that is hadronic decays of the Z at $\sqrt{s} \simeq M_Z$. This operation is called "energy calibration".

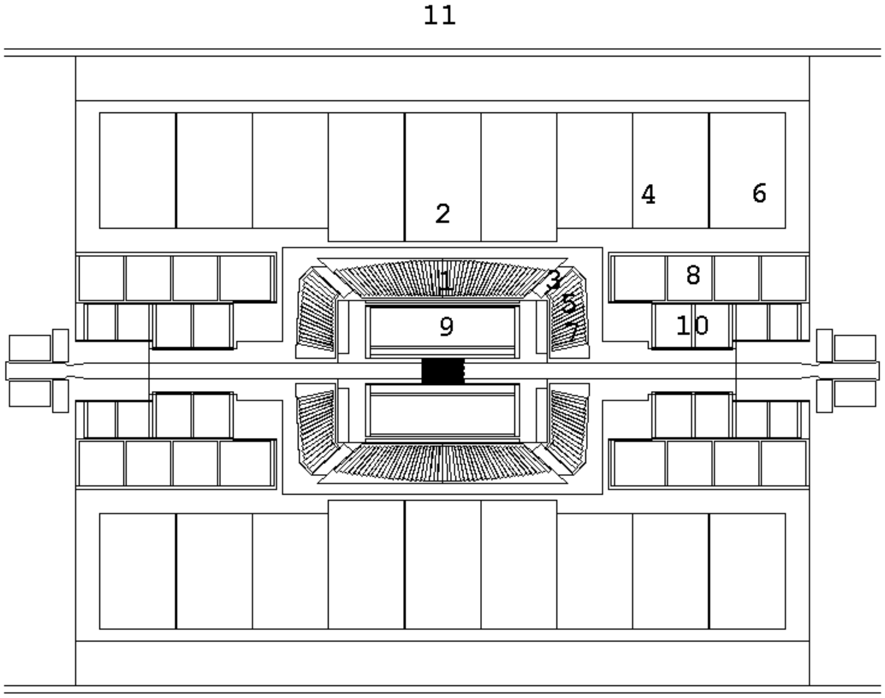

Figure 3.3: The regions of the L3 detector, with different characteristics, used for the hadronic energy calibration and the subsequent measurements of jet energy.

The calibration method used in this thesis is described in ref. [61]. The detector is divided in 11 regions, as shown in fig. 3.3; the cluster energy deposited by the hadrons in each region i is multiplied by a factor G_i, called "G-factor", and the contributions of the different sub-detectors are summed to obtain the total hadronic energy.

The regions labelled by the numbers 1, 3, 5, 7 contain the energy of the electromagnetic showers; region 1 is the BGO barrel, 3 the EGAP, regions 5 and 7 the BGO endcaps separated according to the different parts of the hadronic calorimeter (HC1 and HC2) behind them, which are characterized by a different interaction length and different sampling. Regions labelled with numbers 2, 4, 6, 8, 10 contain the energy of the hadronic showers and are characterized by a different number of interaction lengths, or by different sub-detectors interposed between them and the interaction vertex. Regions number 9 and 11 regard respectively the TEC and the muon chambers.

Since the tracks are included in the energy computation, in order to avoid double counting of the energy of a charged hadron, whose energy is measured both in the TEC than in the calorimeters, the clusters are divided in charged and neutral. A cluster is defined charged if it is constituted by a deposit in the calorimeters matched with a TEC track; if there is no track matching the cluster, then it is called neutral. Afterwards different G-factors are used for neutral and charged clusters, so that for charged clusters the TEC and calorimeter contributions to the hadron energy are properly weighted.

The total energy is then calculated as:

$$E_{\rm tot}^{\rm had} = \sum_{i}^{11} \left(G_i^C \cdot E_i^C + G_i^N \cdot E_i^N \right) \tag{3.4}$$

where the index i runs over the 11 different regions of the detector, E_i^C and E_i^N are respectively the energy of a charged and neutral cluster in the i-th region, G_i^C and G_i^N are the 22 G-factors relative to the charged and neutral clusters.

The G-factors are experimentally determined by minimizing the energy resolution for the hadronic decays of the Z at $\sqrt{s} \simeq M_Z$.

3.4 Lepton and photon identification

The semileptonic and leptonic events discussed in section 2.1 are characterized by the presence of at least one lepton; moreover in the W semileptonic decays there are two jets in addition to such lepton; if the lepton is not well separated from the hadronic showers it may not be easily identified.

In this section I describe the criteria used to identify leptons and photons in presence of hadronic showers. This identification is performed by a program [62], used for several different analyses and which I have developed and modified in some parts in order to adapt it to the W analysis.

This program is organized so that it looks for particles in the following order: muons, electrons and photons in BGO and in EGAP, taus with hadronic decays and MIPs (minimum ionizing particles). The order in which the particles are looked for is important since once a particle is identified, its constituent objects (tracks, clusters, ASRCs, AMUI) are cancelled from the event and are not used in the subsequent search for other particles.

The visible energy of the event E_{vis} is then given by the sum of the expression 3.4 and the energy of each identified lepton and photon:

$$E_{\text{vis}} = E_{\text{tot}}^{\text{had}} + \sum_{\ell} E_{\ell} \qquad (3.5)$$

where the index ℓ runs over all leptons and photons identified.

At this first step the criteria used for the particle identification are such as to have a high identification efficiency and, as a consequence, at this preselection step a rather high contamination is allowed. As we will see, more tighter criteria will be adopted for the final W pair selections described in chapter 5.

3.4.1 Electron and photon identification

Both electrons and photons are called electromagnetic particles since they are characterized by an energy deposit in the electromagnetic calorimeter which fulfils the electromagnetic shower criteria. Electrons are distinguished from photons because the energy deposit in the electromagnetic calorimeter is matched with a track in the TEC.

The informations relative to the bump are used to derive the electron-photon energy and angular coordinates.

The criteria used to select "good" bumps and the matching of the bump with a possible near TEC track are discussed in detail in Appendix A.1; in particular the problem of matching the best track to the bump in case where there are more tracks in a tight window around the bump is faced.

The matching criteria I have introduced are rather complicated and reflect the request to have the maximum electron selection efficiency with a rather low photon contamination.

Electrons and photons are also searched for in the EGAP regions; the identification and isolation criteria used are described in Appendix A.2

To probe the performances of such identifications I have studied the electron identification using an $\text{e}^+\text{e}^- \to \text{WW} \to \text{e}\bar{\nu}\text{q}\bar{\text{q}}$ Monte Carlo sample at $\sqrt{s} = 183$ GeV, where informations on the generated electron are available. In principle one could also perform the same study on a Bhabha sample, but it is not the best choice since we are interested in the electron identification in the presence of hadrons, where we can test the isolation cuts as well.

I have looked for a reconstructed electron in a 0.1 rad half-cone around the direction of an electron generated in the whole phase space and I have found that in 81.5% of the cases it is properly recognized. Of course electrons are not reconstructed at low polar angles, in particular at $\vartheta, \pi - \vartheta < 11.5°$ where there is no electromagnetic calorimeter; moreover the track reconstruction efficiency decreases steeply under 25° as it is shown in fig. 3.4, where the number of reconstructed electrons divided by the number of generated electrons is reported as a function of $\cos\vartheta$.

In 11.1% of the cases the electron is misidentified as a photon; this happens either when the electron is at a low polar angle or when the TEC track is lost because of some inefficiencies; in 3.6% of the cases it is reconstructed as a τ, in a few cases as a MIP and in 3.7% of the cases it is lost (see fig. 3.12 in sec. 3.5).

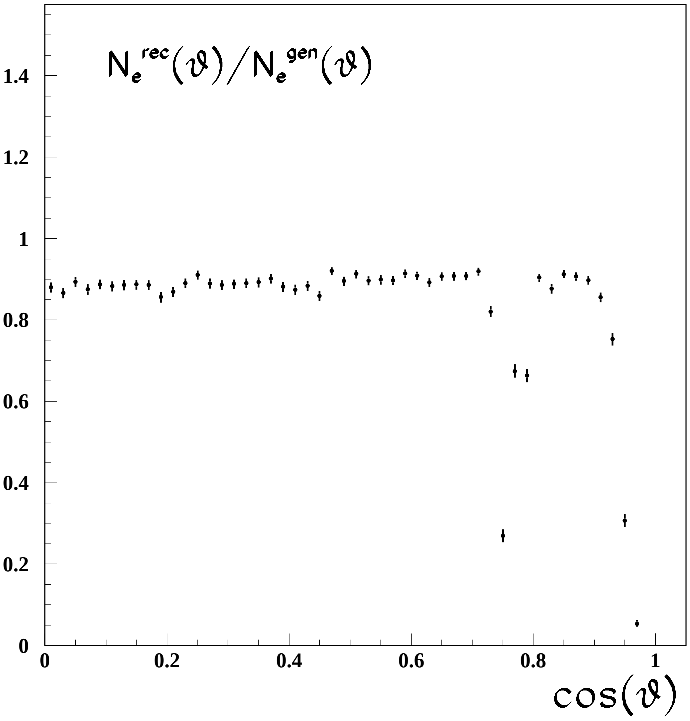

Figure 3.4: Number of reconstructed electrons in a 0.1 rad half-cone around the electron direction divided the number of generated electrons as a function of $\cos\vartheta$.

From fig. 3.4 one can also see that the electron reconstruction efficiency is almost 90% in the BGO barrel, between 30% and 60% in the EGAP[4] and falls steeply after the BGO endcaps for $\cos\vartheta > 0.9$.

Fig. 3.5(a) shows the distributions of the difference between generated and reconstructed quantities such as φ, ϑ and energy for electrons in BGO barrel and endcaps. From the mean and the root mean squared (RMS) reported in the figures it can be argued that electrons are well identified both in angle than in energy; this is due to the good angular and energy resolution of the BGO electromagnetic calorimeter discussed in sec. 1.2.2.

Fig. 3.5(b) shows the same quantities for electrons reconstructed in the EGAP; we can see the worsened performance of electron reconstruction in EGAP respect to BGO, especially regarding the energy reconstruction where the RMS of the difference between the reconstructed and generated electron energy passes from 1.8 GeV, in BGO, to 7.5 GeV in EGAP.

Finally in fig. 3.5(c) one can see the distributions concerning the angular differences in ϑ and in φ between the electron bump and the matched track and also the distribution of the difference between the reconstructed electron energy (that is the bump energy) and the matched track momentum. The comparison between fig. 3.5(c) and fig. 3.5(a) underline the low resolution of the TEC in ϑ and momentum measurement.

---

[4] The electron reconstruction efficiency in a fiducial volume of the EGAP is 60%, the bin with 30% is probably caused by a narrow uninstrumented gap between the EGAP and the BGO barrel.

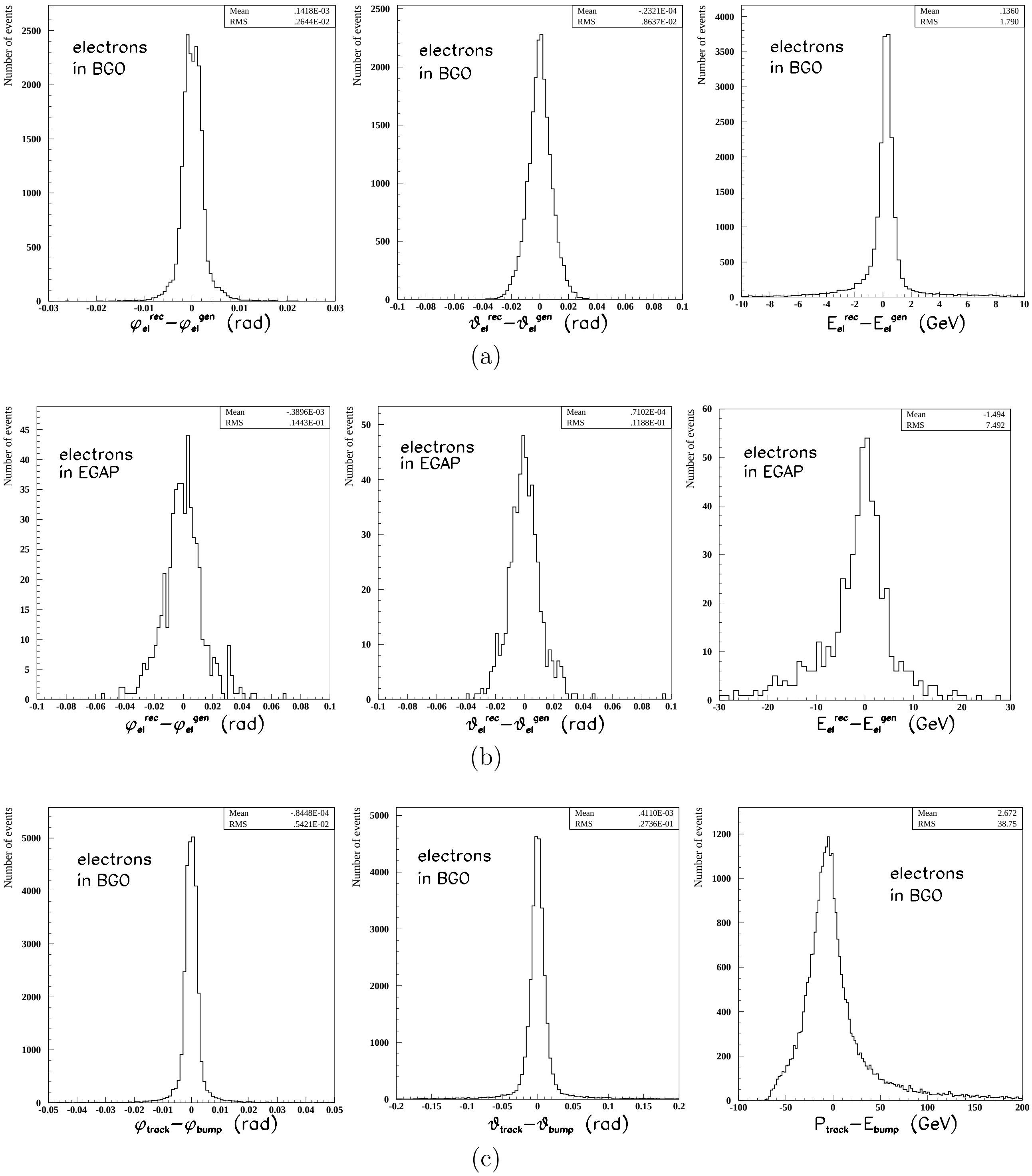

Figure 3.5: (a) Difference between generated and reconstructed quantities for electrons in the BGO barrel and endcaps. (b) Difference between generated and reconstructed quantities for electrons in the EGAP. (c) Difference between φ, ϑ and energy of a reconstructed electron and the same quantities of its matched track.

3.4.2 Muon identification

Muons are identified by the presence of a track in the muon chambers. The criteria used to select muons are listed in Appendix A.3; as for the electron case, these criteria are tuned in order to maximize the identification efficiency for energetic isolated muons.

The best estimate of the original muon energy is the sum of the AMUI momentum and the energy lost by the muon before reaching the muon chambers[5]; this energy is summed to the AMUI momentum in the REL3 program. To further take into account possible δ ray emission of the muon we sum the calorimetric energy contained in a 5° half-cone around the muon direction to the track momentum.

In order to avoid that a TEC track produced by a muon will be subsequently used for reconstructing another lepton, a TEC track matched to the AMUI is dropped from the event. The TEC track-AMUI matching criteria are described in Appendix A.3.

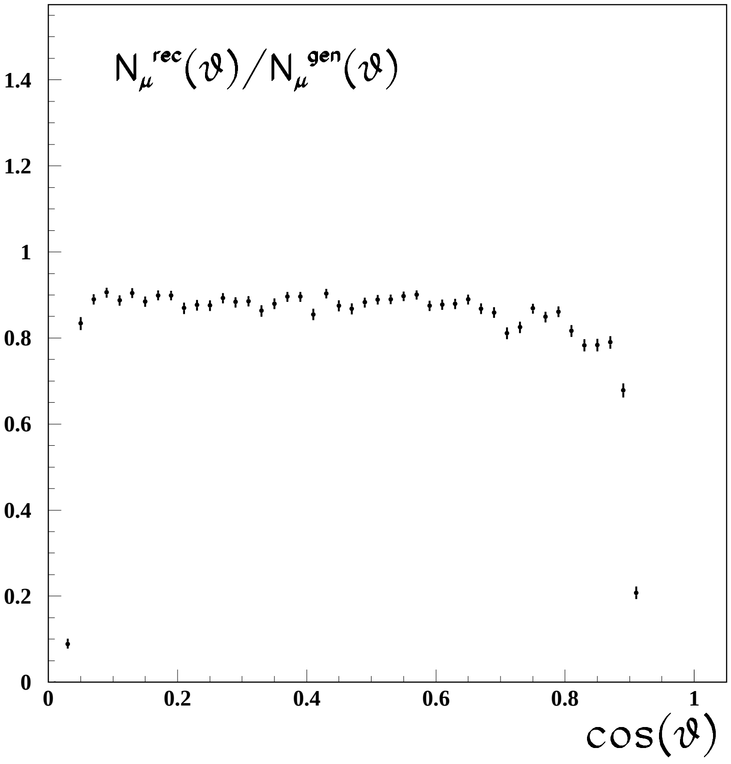

Figure 3.6: Number of reconstructed muons in a 0.1 rad half-cone around the direction of the muon divided the number of generated muons as a function of $\cos\vartheta$.

I have studied the performance of muon identification on a sample of $e^+e^- \rightarrow WW \rightarrow \mu\bar{\nu}q\bar{q}$ events, at $\sqrt{s} = 183$ GeV, with muons generated in the whole phase space; I have looked for a muon in a 0.1 rad half-cone around the direction of a generated muon and I have found that in 74.5% of the cases it is properly recognized, in 10.2% of the cases it is mistaken for a τ, in 2.6% of the cases as a MIP (see next section for a MIP definition), in

---

[5] Muons are minimum ionizing particles in the calorimeters and deliver in average 200 MeV in BGO and 2-3 GeV in the hadronic calorimeter.

a few cases it is mistaken for a γ or for an electron, while it is lost in 11.7% of the cases (see fig. 3.12 in sec. 3.5). Most of the lost muons point at a polar angle $(\vartheta, \pi - \vartheta)$ less than 24°, where the forward-backward muon chambers end their coverage. Fig. 3.6 shows the muon reconstruction efficiency as a function of the polar angle ϑ. It is zero at 90° where the two half-wheels of the muon chambers are joined and there is no active detector; it ithen remains a little below 90% in the remaining barrel region; it falls to between 80% and 85% in the forward-backward muon chambers and drops to zero for $\cos\vartheta$ greater than 0.91.

Fig. 3.7 shows the comparison between the reconstructed and generated particle angular variables, and shows an overall excellent agreement, especially for the φ coordinate.

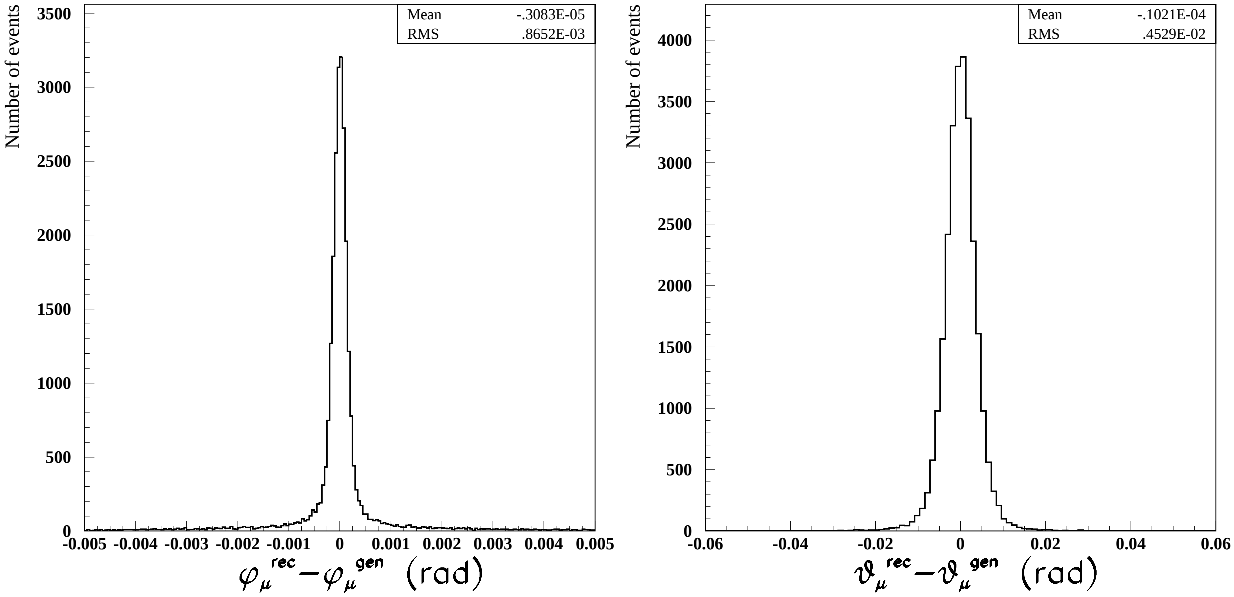

Figure 3.7: Comparison between the muon reconstructed and generated angular variables.

3.4.3 MIP identification

We have seen in the previous section that the muon reconstruction efficiency is not 100% even in the region covered by the muon chambers, therefore, in order to enhance the muon identification efficiency, I have developed a "MIP-finder". A muon with an energy greater than a few GeV, behaves as a minimum ionizing particle (MIP) in the calorimeters, where it typically deposits a few hundred of MeV in the BGO and $\sim$ 2 GeV in the HCAL.

For each TEC track that has not been used to tag other leptons, the algorithm looks whether the track can be matched with a calorimetric energy deposit compatible with a MIP. Then it assigns to the MIP the angular coordinates of the calorimetric cluster and as energy the momentum of the matched track.

The MIP identification and isolation criteria are listed in Appendix A.4.

Since MIPs are reconstructed after all other leptons and, once a lepton is identified its constituent objects are dropped, the Monte Carlo statistics is not enough to study the behavior of the MIP kinematic variables; therefore I have reconstructed a sample of Monte Carlo $e^+e^- \rightarrow WW \rightarrow \mu\bar{\nu}q\bar{q}$ events at $\sqrt{s} = 183$ GeV where all the muons are treated as MIPs and I have studied the performance of the "MIP finder" on such sample.

Fig. 3.8(a) shows the MIP identification efficiency as a function of cosϑ; it is of the order of 65% in all the detector except in the EGAP region where it is about 50% and at low polar angles where it drops to zero.

Since the energy resolution is based totally on the momentum resolution of the TEC, the MIP energy measurement (fig. 3.8(b)) is not as good as in the other cases.

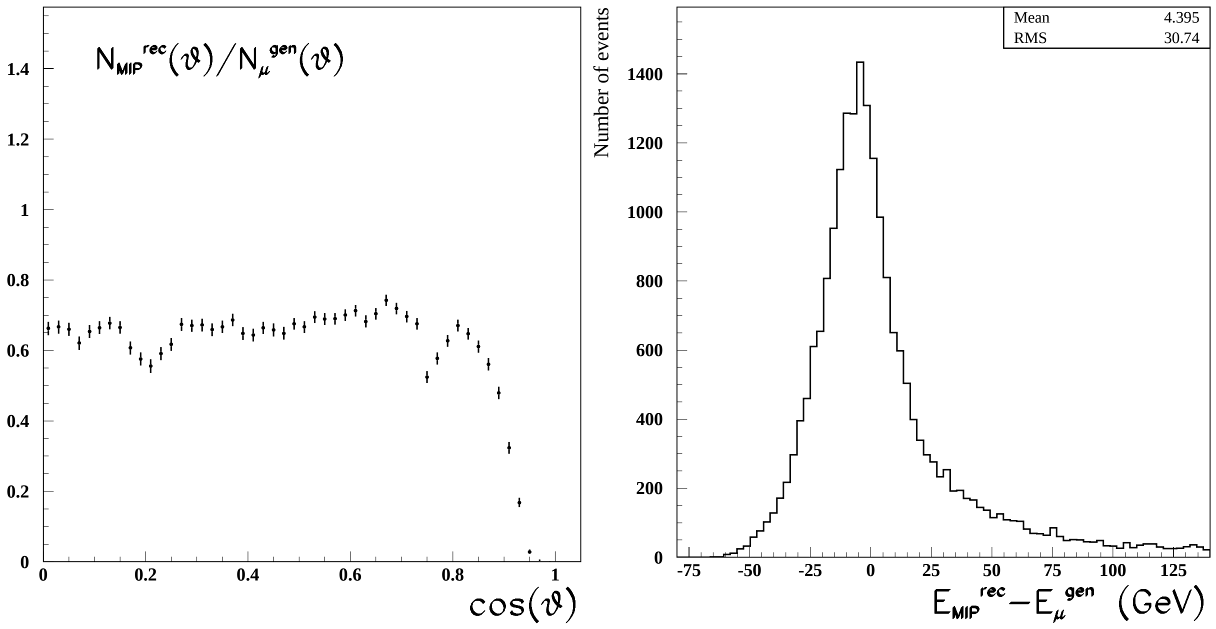

Figure 3.8: (a)Number of reconstructed MIPs in a 0.1 rad half-cone around the muon direction divided the number of generated muons as a function of cosϑ. (b)Comparison between the MIP reconstructed energy and the generated muon energy.

3.4.4 Tau identification

In this section I will describe the identification criteria of τ leptons with hadronic decays, since taus decaying leptonically are characterized by the presence of an electron or a muon in the detector, whose identification criteria have already been described.

We look for isolated hadronic clusters matched with one, two or three TEC tracks with at least 20 hits. Taus with two matched tracks are the ones where either one track is lost due to TEC inefficiencies or where it cannot be resolved from a near track.

The τ direction is determined from the tracks direction weighted by their momenta; the τ energy is then computed as the calorimetric energy contained in a 10° half-cone around the direction of the τ.

The list of cuts used to identify and isolate a tau are reported in Appendix A.5.

I have studied the τ identification efficiency on a $\mathrm{e^+e^-} \rightarrow \mathrm{WW} \rightarrow \tau\bar{\nu}_\tau \mathrm{q\bar{q}}$ sample at $\sqrt{s} = 183$ GeV, looking for a reconstructed τ in a 0.1 rad half-cone around the direction of the generated τ. The result is (see fig. 3.12 in sec. 3.5) that a τ is properly identified in 57% of the cases. When the calorimetric energy deposit is compatible with an electromagnetic particle the τ may be mistaken for a photon (6.7% of the times) or an electron (8.7% of the times) depending whether none or just one track is reconstructed (no track may be present along the τ direction due to TEC inefficiency or to the τ low polar angle). In 1.7% of the cases the τ is mistaken for a MIP and 25% of the times it is lost.

Fig. 3.9(a) shows that in the angular region covered by the calorimeters the identification efficiency for hadronically decaying taus is about 60%. Fig. 3.9(b) shows the difference between the generated and the reconstructed τ energy; since the decay of a τ always involves one or more neutrinos, such a figure provides an estimate of the neutrino energy and does not give any information about the resolution of the τ energy measurement.

Fig. 3.9 (c) and (d) show the differences for the reconstructed and generated τ angles ϑ and φ; the RMSs of about 2° are dominated by the unknown neutrinos direction and momentum.

If the τ decays leptonically it is classified as an electron or a muon through the identification criteria discussed in the previous sections. In these cases however the presence of neutrinos in the tau decay will allow in the analysis described in chapter 5 to label as tau some of the low energy particles identified as electrons or muons. Fig. 3.10 and 3.11 show the same quantities described in fig. 3.9 for a Monte Carlo sample of taus decaying respectively in electron and in muon (plus neutrinos). Fig. 3.10(a) shows a drop in the EGAP region ($\cos\vartheta \simeq 0.76$), while fig. 3.11(a) shows the low muon reconstruction efficiency at $\vartheta \simeq 90°$.

As for the hadronically decaying taus, the low angular resolution shown in fig. 3.10, 3.11 (c) and (d) are due to the unknown neutrinos direction and momentum.

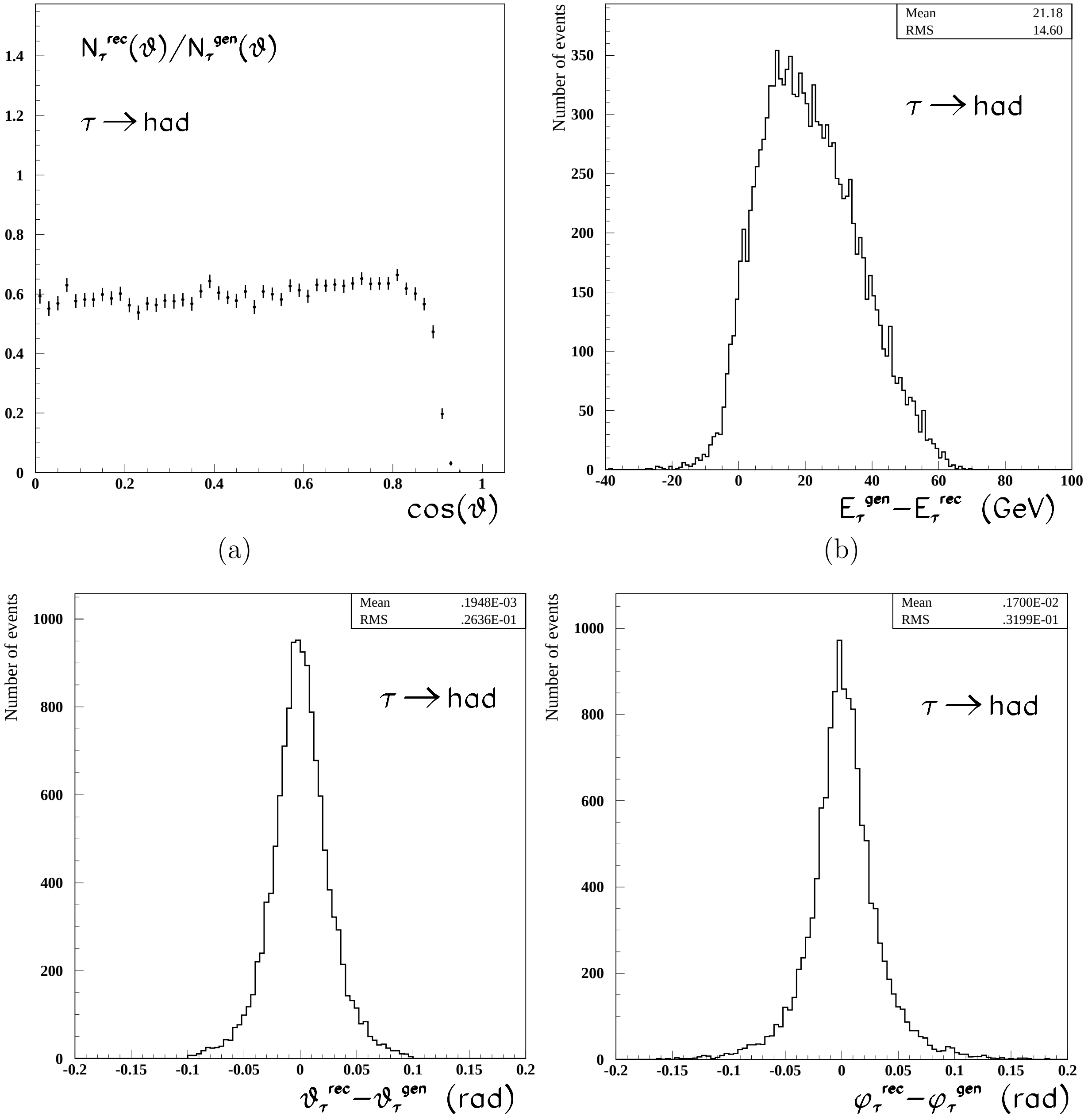

(a) (b)

(c) (d)

Figure 3.9: (a) Identification efficiency for hadronically decaying taus as a function of cosϑ. (b) Energy difference between the generated and the reconstructed τ, mainly due to the missing neutrinos. (c) Angular difference between the reconstructed and generated τ polar angles. (d) Angular difference between the reconstructed and generated τ azimuthal angles.

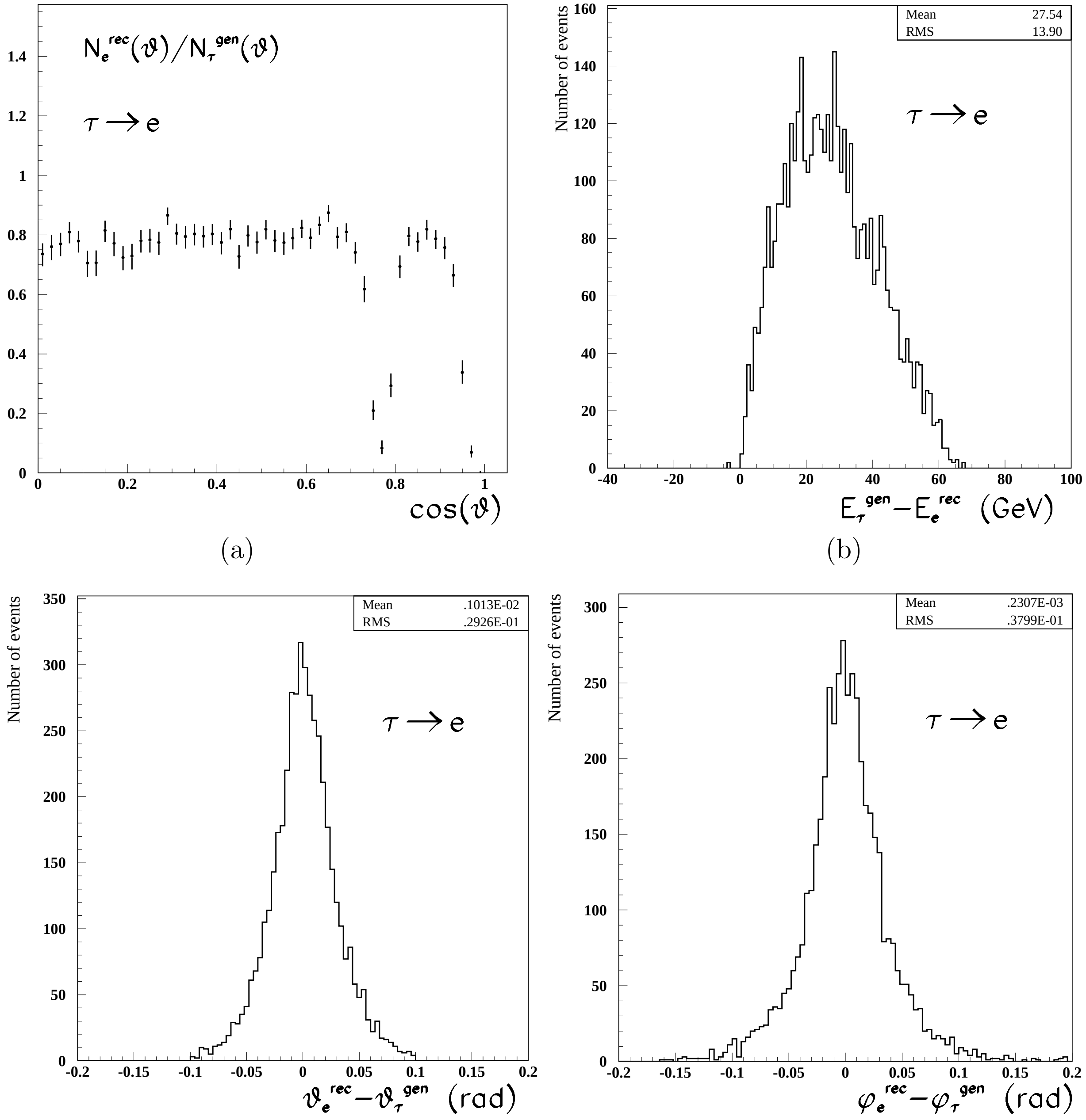

(a) (b)

(c) (d)

Figure 3.10: (a) Identification efficiency for leptonically decaying $\tau \rightarrow e\bar{\nu}_e\nu_\tau$ as a function of $\cos\vartheta$. (b) Energy difference between the generated τ and the reconstructed e, mainly due to the missing neutrinos. (c) Angular difference between the reconstructed e and generated τ polar angles. (d) Angular difference between the reconstructed e and generated τ azimuthal angles.

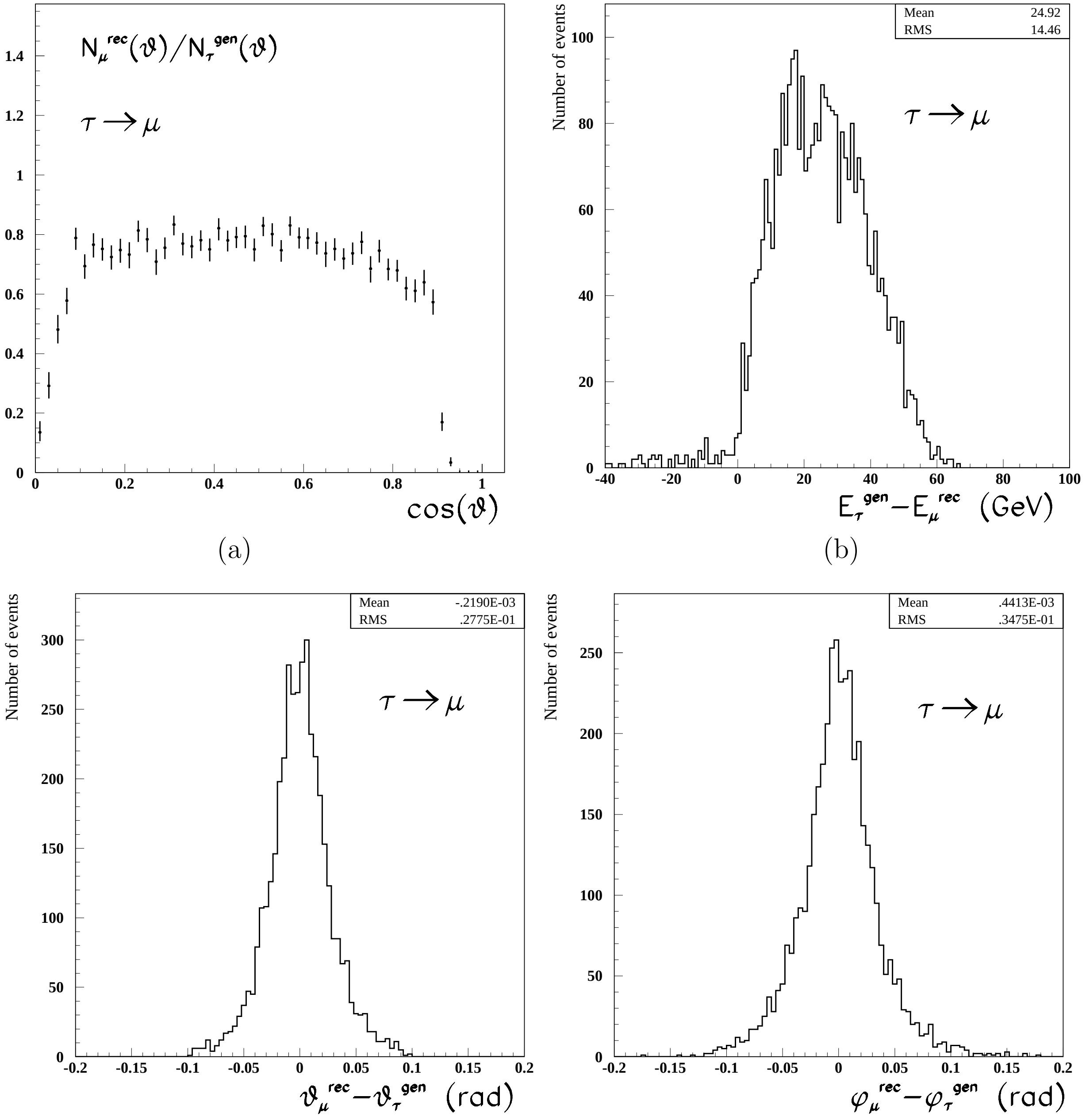

(a) (b)

(c) (d)

Figure 3.11: (a) Identification efficiency for leptonically decaying $\tau \rightarrow \mu\bar{\nu}_\mu\nu_\tau$ as a function of cosϑ. (b) Energy difference between the generated τ and the reconstructed μ, mainly due to the missing neutrinos. (c) Angular difference between the reconstructed μ and generated τ polar angles. (d) Angular difference between the reconstructed μ and generated τ azimuthal angles.

3.5 Summary of lepton identification performance

In fig. 3.12 the performances of the reconstruction program in lepton identification are summarized.

I have reported in abscissa the different types of possible reconstructed particles: electrons, muons, taus, MIPs and photons. In ordinate there are the types of different generated leptons: electrons coming from the process $e^+e^- \to WW \to e\bar{\nu}q\bar{q}$, muons from $e^+e^- \to WW \to \mu\bar{\nu}q\bar{q}$ and taus from $e^+e^- \to WW \to \tau\bar{\nu}q\bar{q}$; for the tau case I have split the sample in taus decaying hadronically and taus with a leptonic decay ($\tau \to e\bar{\nu}_e\nu_\tau$, $\tau \to \mu\bar{\nu}_\mu\nu_\tau$).

Each sample has a statistics proportional to the branching ratio of the relative process; the number of starting events are reported in ordinate as well. The numbers in the boxes of each row show how many of a given type generated leptons are reconstructed as electron, muon, tau, MIP and photon. As expected electrons are identified mostly as electrons, muons mostly as muons and so on.

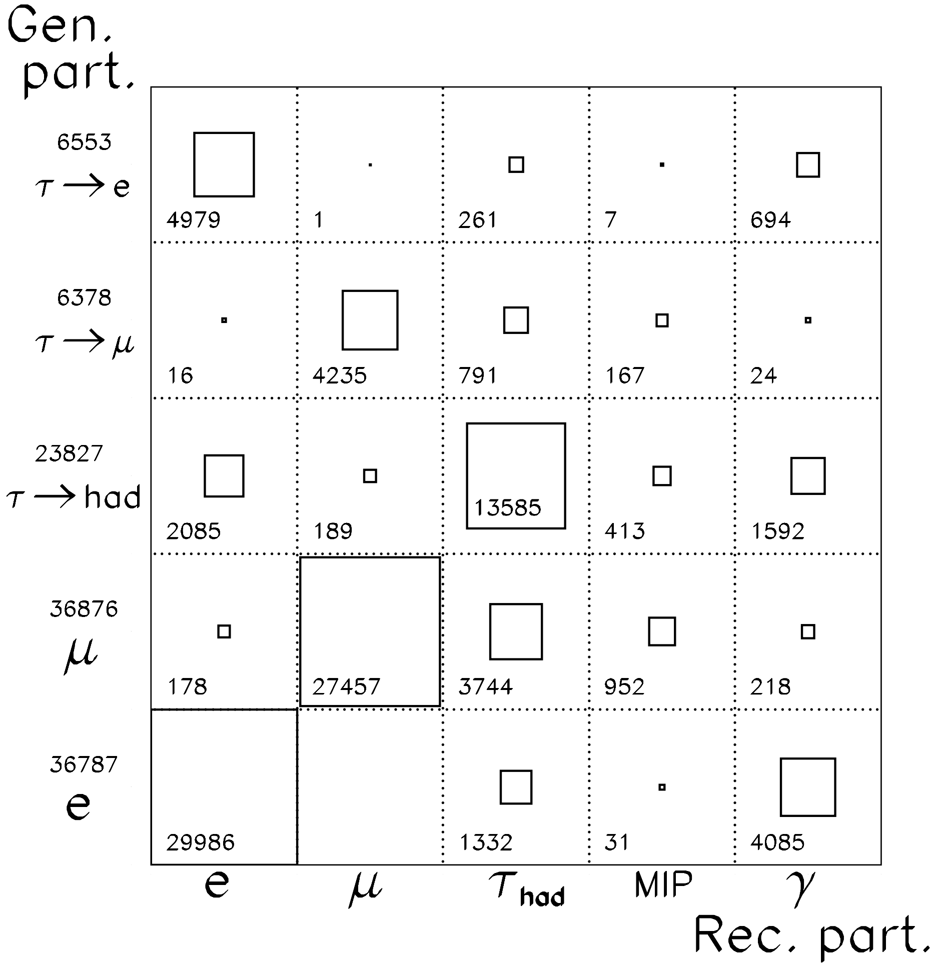

Figure 3.12: Summary of lepton identification performance, where number of generated leptons against different types of reconstructed particles are reported.

3.6 Jet identification performance

In this section a comparison is made between variables regarding the reconstructed jets and the original values of the generated partons, in a similar way to what has been done for leptons.

To this end I have studied jets in sub-samples of semileptonic events $e^+e^- \to WW \to e\bar{\nu}q\bar{q}$, $\mu\bar{\nu}q\bar{q}$, with the reconstructed lepton (e, μ) subtracted from the event.

I define the jet reconstruction efficiency as the number of jets reconstructed in a 0.2 rad half-cone around the direction of the generated quark divided by the number of generated quarks as a function of $\cos\vartheta$ (fig. 3.13). This efficiency is characterized by a constant behaviour over the whole detector; its value however depends on the dimension of the cone in which the jet is searched, since jets are large objects.

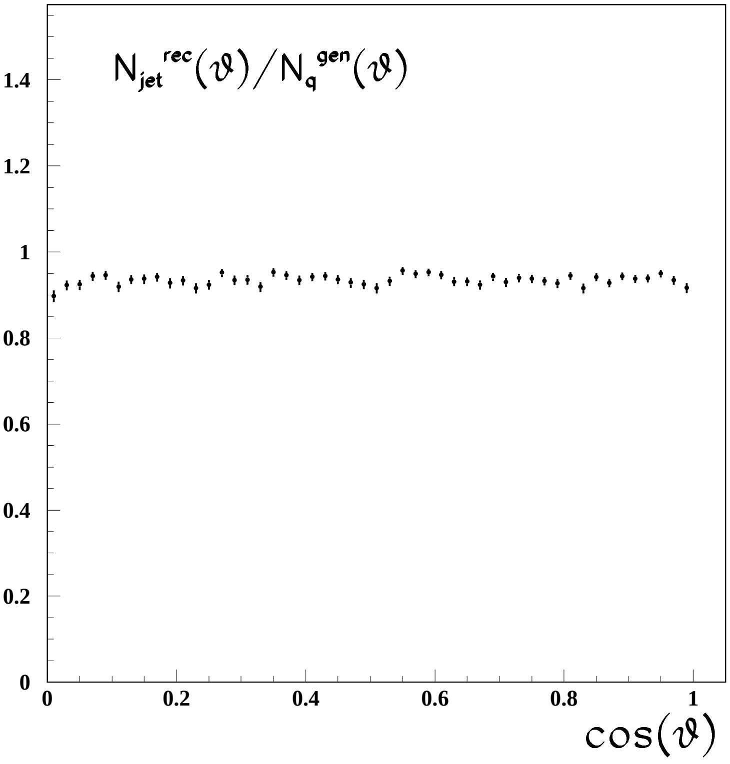

Figure 3.13: Number of reconstructed jets in a 0.2 rad half-cone around the direction of the original quark divided by the number of generated quarks as a function of $\cos\vartheta$.

Fig. 3.14 and 3.15 give an estimate for the angular and energy resolution of reconstructed jets. Jets are searched in a 0.2 rad half-cone around the direction of the generated quark and the difference between the reconstructed and corresponding generated quantities are shown.

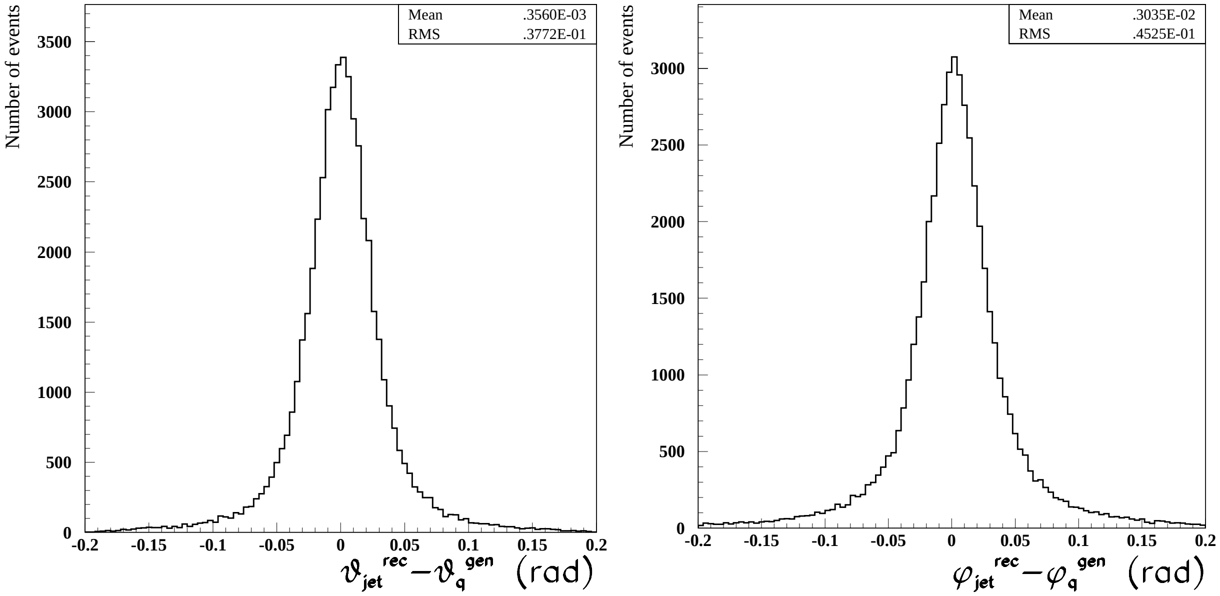

Figure 3.14: Comparison between the reconstructed jet and the original quark angular coordinate.

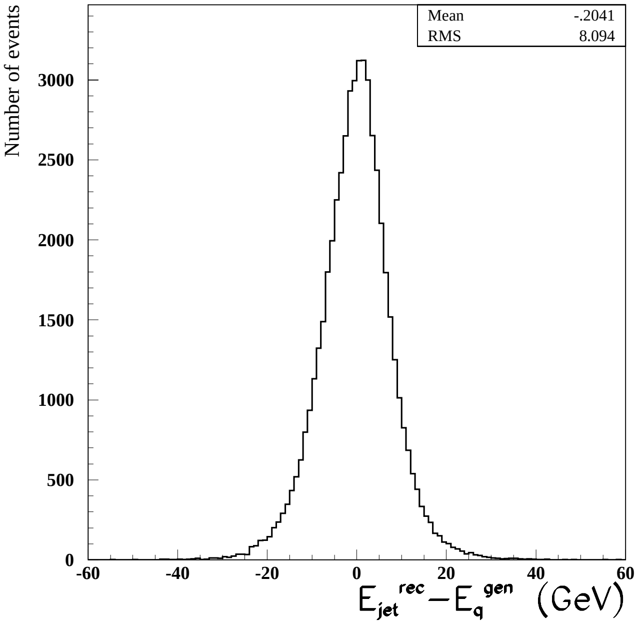

Figure 3.15: Comparison between the reconstructed jet energy and the original quark energy.

Chapter 4

Optimized multi-cuts method

4.1 Introduction

The aim of this thesis is the cross section measurement of W pair production. For this purpose we have developed a new method of analysis in order to obtain a lower statistical error respect to the standard methods.

In general the cross section measurement of a physical process is extracted from the following formula:

$$N_{\mathrm{sig}} = \varepsilon \cdot \sigma \cdot \mathcal{L} + N_{\mathrm{bkg}}$$

that relates the number of signal events N_{sig} to the expected events number $\varepsilon \cdot \sigma \cdot \mathcal{L} + N_{\mathrm{bkg}}$ through the unknown cross section σ, ε is the expected selection efficiency, $\mathcal{L}$ the luminosity and N_{bkg} the expected number of events coming from background processes.

There are mainly two different method commonly used to select the data sample:

- cut-based analysis
- multivariate analysis

In the cut-based analysis the number of signal events N_{sig} and the expected selection efficiency are determined by applying a set of cuts respectively on the data and on the MC signal sample. The set of cuts to be used are found by eye looking at the MC distribution variables that better discriminate signal from background (fig. 4.1).

In the multivariate-based analysis more complicated techniques to discriminate signal from background are used in order to increase the selection efficiency for a given purity[1]. The most used of these techniques is the Neural Network (N.N.) approach; that is a N.N. is trained on both MC signal and background in order to better discriminate the two sample data, using a certain number of variables. A typical output of a N.N. is shown in fig. 4.2, applied to a four jet hadronic sample. The cross section is then computed either determining N_{sig} and ε by a traditional cut to the N.N. output, or with a global likelihood fit to the found and expected distributions of the N.N.

---

[1] The purity of a selection is defined as the number of selected events in the signal sample, N_{sig}, divided by the sum of N_{sig} and the number of background events that pass such a selection.

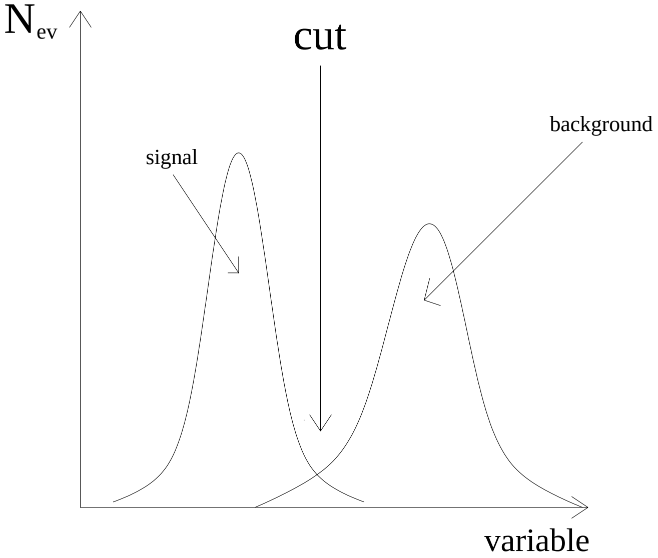

Figure 4.1: Cut chosen by eye in order to discriminate signal from background.

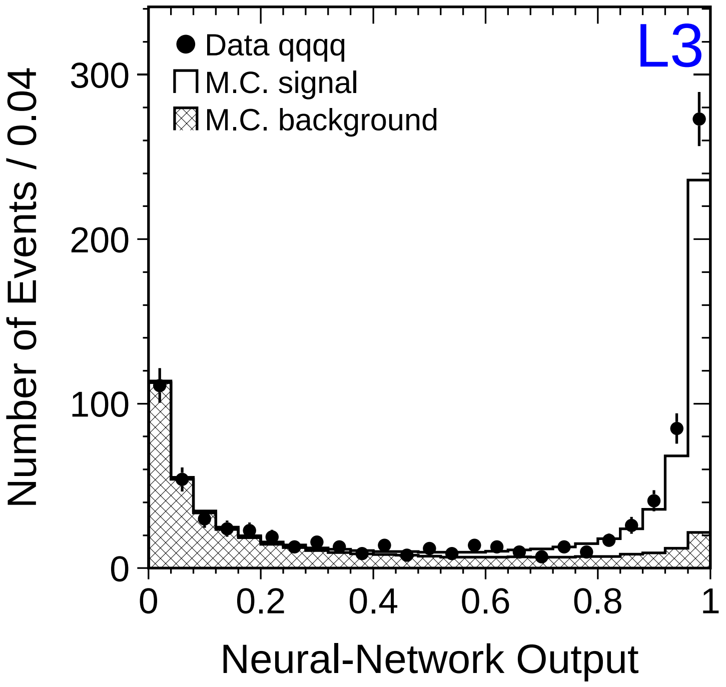

Figure 4.2: Typical neural network output.

Generally the cut-based method is more safe; selecting events by applying cuts to the variables distributions has the advantage that one can compare step by step data to MC distributions for every variable, so that it is relatively easy to find out possible discrepancies. Moreover with this method the systematic error determination procedure is well tested and under control. The counterpart is that the variables used for the selection are usually correlated and it is not easy to take this correlation into account if one deals with ten or more variables. As a consequence a cut-based analysis usually does not achieve the best possible efficiency for a given purity of the signal sample. On the other hand selections done using a N.N. have usually better performances, but are less transparent.

Usually a cut-based analysis has to be preferred to a multivariate-based analysis if the latter offers no significant gain in performance.

4.2 Optimized multi-cuts method

In this chapter a new method that takes advantage from both techniques mentioned above will be described. The optimized multi-cuts method should have the transparency of a cut-based analysis combined with the highest possible efficiency for a given number of background events.

For a better understanding of this method I will anticipate in this chapter some results regarding the W pair selections that will be explained and described in detail in the next chapter.

The optimized multi-cuts method, developed during the work for this thesis, consists mainly in two parts. In the first step the problem of finding a set of cuts that permits to minimize the statistical error of a cross section measurement will be faced. In the second step a weight factor will be introduced in the definition of statistical error, which will allow the production of several "optimized" selections for each analysis channel. Eventually all these selections will be used to extract the relative cross sections with a global maximum likelihood fit.

4.2.1 Step 1: Optimization of a single selection

As pointed out in the previous paragraphs, choosing cuts by eye makes difficult to take into account possible correlations in the multi-dimensional space of variables, so to overcome this problem we have used MINUIT [27] to choose the set of cuts that minimizes the statistical error of a cross section measurement. The procedure works in the following manner: let $\vec{\xi}$ be the vector of cuts used for a certain selection, the $\vec{\xi}$ vector is moved automatically by the minimization program and for every value of $\vec{\xi}$ in the multi-dimensional phase space cuts the statistical error on the cross section is computed; the procedure ends when a minimum is found.

To be more precise, since the statistical error depends also on the number of candidates selected in real data, we have chosen to minimize the "expected" statistical error described in the next paragraph.

The expected statistical error

To measure a cross section we need to count the number of events that pass a certain selection. This number is subject to Poisson statistics and the statistical error of a cross section measurement derives directly from the error on this number.

Let k be the number of events selected in the data; computing the statistical error at $\alpha = 68.2\%$ of confidence level (C.L.) means finding two numbers λ_1 and λ_2 (fig. 4.3) so that the probability to have in a measurement a number of events greater than k is $\alpha/2$ for a Poisson distribution whose mean value is λ_1 and the probability to find a number of events lower than k is $\alpha/2$ for a Poisson distribution whose mean value is λ_2.

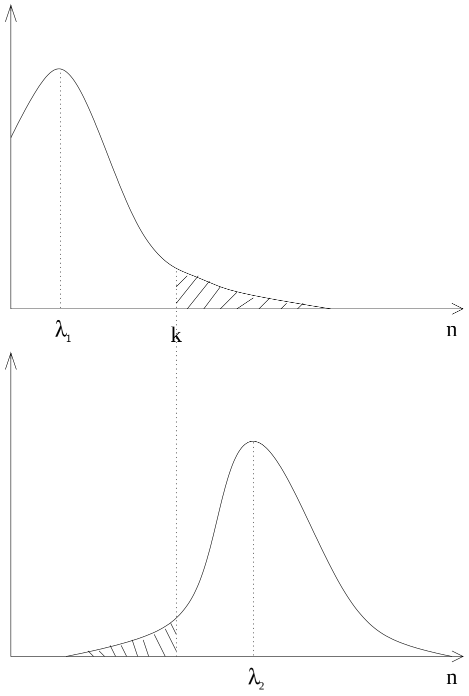

Figure 4.3: Statistical error at 68.2% of C.L.

$$\begin{aligned}
\sum_{n=k}^{\infty} \frac{e^{-\lambda_1}\lambda_1^n}{n!} &= \tfrac{1}{2}(1-\alpha) \quad \Longrightarrow \sum_{n=0}^{k-1} \frac{e^{-\lambda_1}\lambda_1^n}{n!} = \frac{1}{2}(1+\alpha) \\
\sum_{n=0}^{k} \frac{e^{-\lambda_2}\lambda_2^n}{n!} &= \tfrac{1}{2}(1-\alpha)
\end{aligned}$$

Tab. 4.1 shows the Poisson statistical error Δk on a count k computed at 68.2% of C.L. where:

$$\Delta k_- = k - \lambda_1$$
$$\Delta k_+ = \lambda_2 - k$$
$$\Delta k = \lambda_2 - \lambda_1$$

	68.2% of C.L.			variance	width-log-lik		
k	Δk	Δk_+	Δk_-	$2 \cdot \sqrt{k}$	Δk	Δk_+	Δk_-
1	3.124	2.297	0.827	2.000	2.056	1.358	0.698
2	3.925	2.634	1.291	2.828	2.868	1.765	1.102
3	4.546	2.915	1.6313	3.464	3.496	2.080	1.416
4	5.071	3.159	1.913	4.000	4.028	2.346	1.682
6	5.956	3.579	2.377	4.899	4.922	2.794	2.128
10	7.367	4.261	3.105	6.325	6.342	3.504	2.838
20	9.968	5.539	4.429	8.944	8.957	4.812	4.145
50	15.146	8.107	7.038	14.142	14.150	7.408	6.742
100	20.988	11.018	9.970	20.000	20.006	10.336	9.670
300	35.601	18.314	17.287	34.641	34.644	17.655	16.989

Table 4.1: Statistical error at 68.2% of C.L. compared to the Poisson variance and to the log-likelihood-error.

These errors are compared, in tab. 4.1, to the same error evaluated as the square root of the Poisson variance $\sqrt{k}$ and to the error evaluated as the width of the log-Likelihood function at maximum minus one half (sometimes wrongly[2] reported as having a statistical meaning of 68.2% of C.L.). One can see that the difference between the three evaluations of the errors become negligible only when the count number k is very large.

The method described above is the correct way to find the statistical error for a cross section measurement at 68.2% C.L. in the case k is an integer as it is always in a count of real data. Indeed our purpose is to find the "expected" statistical error that is the statistical error we would have if the count k is exactly equal to what we expect from MC. Since we usually simulate a number of MC events thousands of times greater than the expected ones, once we normalize the number of MC selected events to the luminosity of the experiment the result is a non integer value of expected events.

For this reason we need to extrapolate the method above for a non integer number of selected events, that from now on we will call x.

Let $\delta\sigma_{\mathrm{stat}}^{\mathrm{exp}}(x, N_{\mathrm{bkg}})$ be the expected statistical error as a function of the number x of selected events and N_{bkg} the number of expected background events; the optimization procedure works well only if $\delta\sigma_{\mathrm{stat}}^{\mathrm{exp}}(x, N_{\mathrm{bkg}})$ is a continuous function of its parameters, so we cannot simply put $\delta\sigma_{\mathrm{stat}}^{\mathrm{exp}}$=$\delta\sigma_{\mathrm{stat}}^{\mathrm{exp}}(\mathrm{int}(x)$,$N_{\mathrm{bkg}})$ which is a step function.

The simplest generalization I have thought of is the following: let k=int(x) and $\Delta x = x - k$, then I search for two values λ_1 and λ_2 such that (fig 4.4):

$$\begin{aligned}
\sum_{n=k}^{\infty} \frac{e^{-\lambda_1}\lambda_1^n}{n!} - \frac{e^{-\lambda_1}\lambda_1^k}{k!} \cdot \Delta x &= \tfrac{1}{2}(1-\alpha) \quad \Longrightarrow \sum_{n=0}^{k-1} \frac{e^{-\lambda_1}\lambda_1^n}{n!} + \frac{e^{-\lambda_1}\lambda_1^k}{k!} \cdot \Delta x = \frac{1}{2}(1+\alpha) \\
\sum_{n=0}^{k} \frac{e^{-\lambda_2}\lambda_2^n}{n!} + \frac{e^{-\lambda_2}\lambda_2^{k+1}}{(k+1)!} \cdot \Delta x &= \tfrac{1}{2}(1-\alpha)
\end{aligned}$$

---

[2] For a not Gaussian distribution.

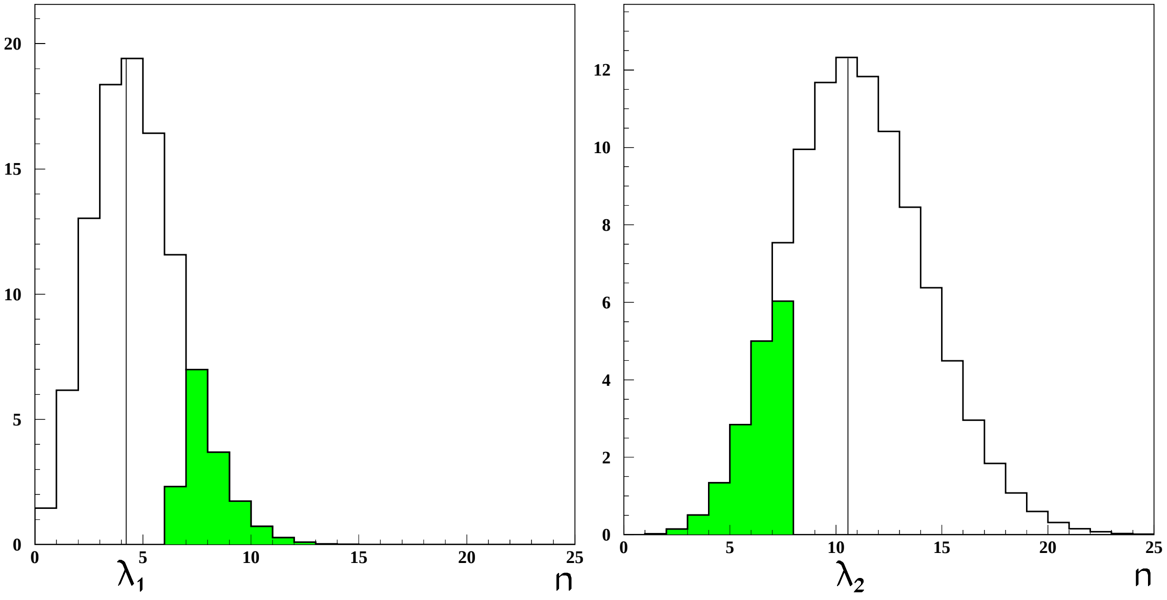

Figure 4.4: Statistical error at 68.2% of C.L. in case of a non integer number of selected events x=6.8.

The idea being the following: supposing that x=6.8 as in fig 4.4, if x were 6 then I would have chosen λ_1 so that the integral from 6 to infinity equals 15.9%. But since x=6.8 I subtract from the previous integral 80% of the content of the 6-th bin (the integral correspond to the shaded area in the figures).

For the upper limit λ_2, if x were 6 I would require that the sum of the bins of the second distributions shown in fig 4.4 from 0 to 6 to be equal to 15.9%. Since x=6.8 I have to add 80% of the contents of the 7-th bin to the previous integral.

By definition this extrapolated probability conserves unitarity in the sense that:

$$\sum_{n=0}^{k-1} \frac{e^{-\lambda_1}\lambda_1^n}{n!} + \frac{e^{-\lambda_1}\lambda_1^k}{k!} \cdot \Delta x + \sum_{n=0}^{k} \frac{e^{-\lambda_2}\lambda_2^n}{n!} + \frac{e^{-\lambda_2}\lambda_2^{k+1}}{(k+1)!} \cdot \Delta x = 1$$

and moreover

$$\delta\sigma_{\text{stat}}^{\text{exp}} = \frac{\lambda_2(x) - \lambda_1(x)}{\varepsilon\,\mathcal{L}}$$

is a continuous function of x.

Optimization program

As already mentioned the optimization procedure is an almost automatic way to obtain a selection with highest possible efficiency and lowest background once the variables that better discriminate signal from background are chosen.

Since a wrong choice of the variables could invalidate the advantages brought by the optimization part, I perform this choice in two steps. First I put into the program all the variables, and their combinations, that can be useful for the selection without worrying about their possible correlations, then I find with the minimization procedure the set of optimum cuts for this superset of variables.

Then, in order to reduce the number of variables used, I have implemented in the optimization program a part that automatically removes redundant variables in the following way: for every cut j the increase $\Delta(\delta\sigma_{\rm stat}^{\rm exp})$ of the expected statistical error without the cut on that variable is evaluated,

$$\Delta(\delta\sigma_{\rm stat}^{\rm exp}) = \frac{\delta\sigma_{\rm stat}^{\rm exp}\left(\varepsilon(\vec{\xi}^{\,{\rm all}-j}), N_{\rm bkg}(\vec{\xi}^{\,{\rm all}-j})\right) - \delta\sigma_{\rm stat}^{\rm exp}\left(\varepsilon(\vec{\xi}^{\,\rm all}), N_{\rm bkg}(\vec{\xi}^{\,\rm all})\right)}{\delta\sigma_{\rm stat}^{\rm exp}\left(\varepsilon(\vec{\xi}^{\,\rm all}), N_{\rm bkg}(\vec{\xi}^{\,\rm all})\right)}$$

where $\vec{\xi}^{\,\rm all}$ is the vector of all cuts used for the selection and $\vec{\xi}^{\,{\rm all}-j}$ is the same vector without the j-th cut.

Afterwards the program removes all the cuts on variables with zero increase in the statistical error and ranks the remaining ones in order of $\Delta\delta\sigma_{\rm stat}^{\rm exp}$ value.

Moreover it produces as output the "histograms n-1" of all the variables, that is the histograms where all the cuts are applied but the one related to the variable plotted.

So, looking at the $\Delta\delta\sigma_{\rm stat}^{\rm exp}$ value and at the n-1 histograms at the same time, it is easy to choose the most useful variables and re-optimize the selection with this reduced set to obtain the final result.

In fig. 4.5 it is shown the bi-dimensional surface of $\delta\sigma_{\rm stat}^{\rm exp}$ for the four jet selection in the case where the two variables are independent and it is also shown the point where the optimization program has found a minimum.

However there is a problem related to this procedure; if the number of simulated events is not very big, as it may happen on the tails of the distributions, where one can have just a few discrete events (fig. 4.6), the minimization procedure will produce a polarized results towards a bigger efficiency.

This problem is overcome applying the optimization only on one half of the simulated sample and evaluating the efficiency on the other half sample.

4.2.2 Step 2: Multi-selections

To further reduce the statistical error, we need to construct, for every WW channel decay, a set of optimized selections that progress from a selection with low efficiency and low background contamination to a selection with high efficiency and high background. I will explain why in the next ideal example: suppose we want to measure a cross section of a process and suppose that the optimization program has found a minimum for a selection with ε=80% and $N_{\rm bkg}$=50 and that with this selection we have found $N^{\rm data}$=450 events in the data collected at a integrated luminosity $\mathcal{L}$=50 pb^{-1} (fig. 4.7(a)). Moreover let's compute in this example the statistical error as the width of the following likelihood:

$$\begin{aligned} \ell &= -2\cdot\ln\frac{e^{-\lambda}\lambda^{N^{\rm data}}}{N^{\rm data}!} \\ \lambda &= \varepsilon\cdot\sigma\cdot\mathcal{L} + N_{\rm bkg} \end{aligned}$$

at minimum plus one half. The result of this measurement is:

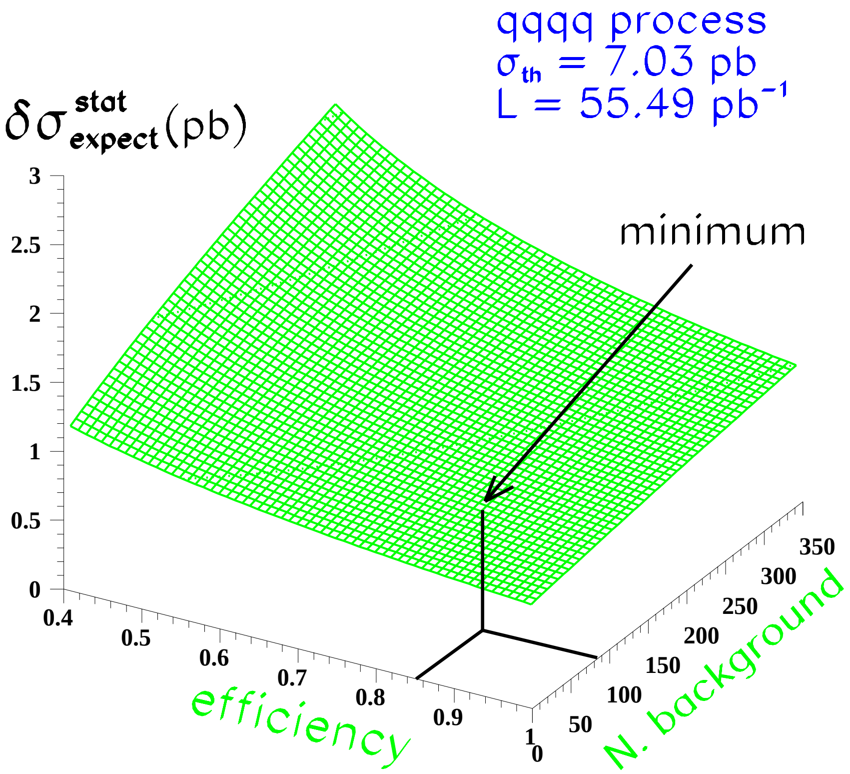

Figure 4.5: Expected statistical error on WW → qqqq(γ) cross section measurement as a function of signal efficiency and number of background events.

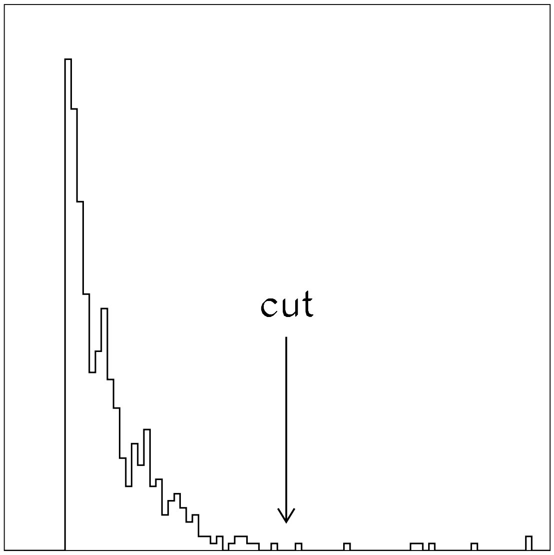

Figure 4.6: Discrete tail of a distribution.

$$\sigma = \left(10.0^{+0.539}_{-0.522}\right)\ \mathrm{pb}^{-1} \Longrightarrow \delta\sigma_{\mathrm{stat}} = 1.061\ \mathrm{pb}^{-1}$$

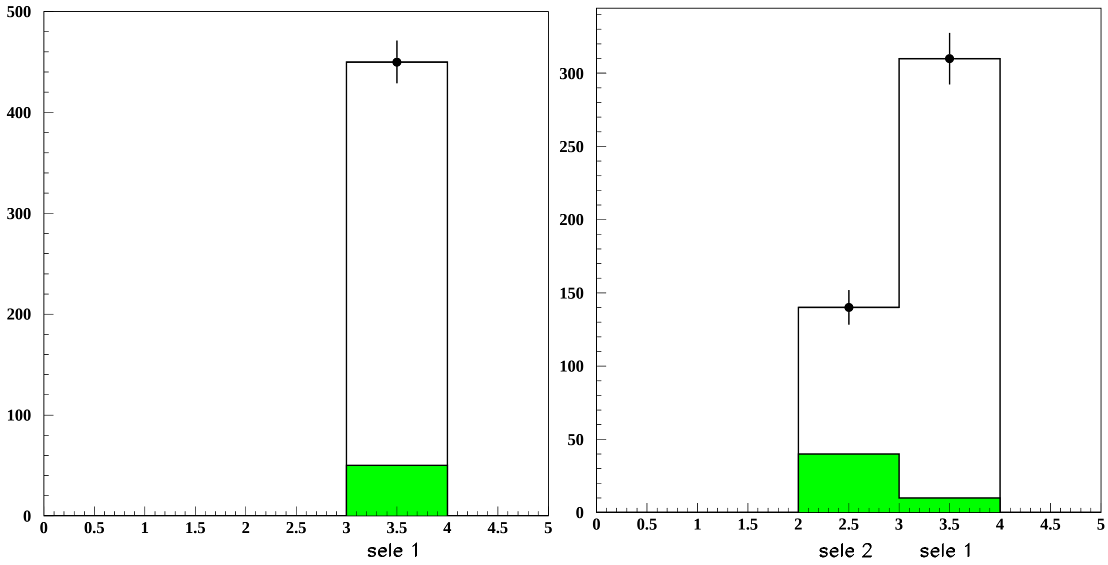

(a) (b)

Figure 4.7: (a) Optimized selection, (b) same selection split in two parts.

Since this result comes from the optimum selection this should be the best one can achieve. Indeed if we split this selection in two parts I will show that the situation can even improve. To this end let's make a purer selection with ε=60% and N_{bkg}=10 with the additional request that every event in it passes also the optimum one; this selection is worse than the previous since using it we would obtain a $\delta\sigma_{\mathrm{stat}} = 1.174\ \mathrm{pb}^{-1}$, but if we construct a histogram (fig. 4.7(b)) where we put in the first bin the events that pass the first (optimized) selection but not the second, and in the second bin the events that pass just the second selection (the purer) and then we minimize the following likelihood:

$$\begin{aligned} \ell &= -2 \cdot \ln \sum_{i=1}^{2} \frac{e^{-\lambda_i} \lambda_i^{N_i^{\mathrm{data}}}}{N_i^{\mathrm{data}}!} \\ \lambda_i &= \varepsilon_i \cdot \sigma \cdot \mathcal{L} + N_i^{\mathrm{bkg}} \end{aligned}$$

with:

i	ε_i	N_i^{data}	N_i^{bkg}
1	0.2	140	40
2	0.6	310	10

we find:

$$\sigma = \left(10.0^{+0.534}_{-0.517}\right)\ \mathrm{pb}^{-1} \Longrightarrow \delta\sigma_{\mathrm{stat}} = 1.052\ \mathrm{pb}^{-1}$$

We can further improve the situation with adding a third larger selection, let's say with ε=90% and N_{bkg}=150 with the additional request that it contains all the events selected by the previous selections; as before we can construct a histogram (fig. 4.8)

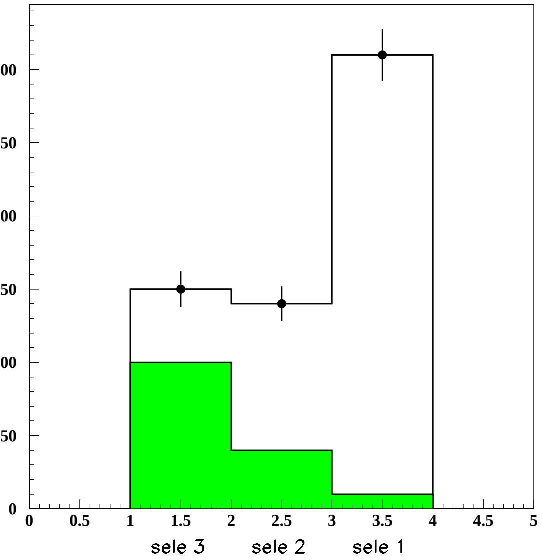

Figure 4.8: Histogram enriched with a selection at higher efficiency.

where we put in the first bin only the events that pass the larger selection and the other two bins as before. If we measure now the cross section minimizing ℓ:

$$\begin{aligned} \ell &= -2 \cdot \ln \sum_{i=1}^{3} \frac{e^{-\lambda_i} \lambda_i^{N_i^{\text{data}}}}{N_i^{\text{data}}!} \\ \lambda_i &= \varepsilon_i \cdot \sigma \cdot \mathcal{L} + N_i^{\text{bkg}} \end{aligned}$$

with:

i	ε_i	N_i^{data}	N_i^{bkg}
1	0.1	150	100
2	0.2	140	40
3	0.6	310	10

we obtain:

$$\sigma = \left(10.0^{+0.522}_{-0.506}\right) \text{ pb}^{-1} \Longrightarrow \delta\sigma_{\text{stat}} = 1.028 \text{ pb}^{-1}$$

We have thus reduced the statistical error found with the optimized selection by more than 3%. The improvement can be greater still, first if we increase the number of selections used, second if the purer and the larger selections are also optimized in the sense that for a fixed efficiency they have the lowest background contamination. But in the previous paragraphs we have seen that by definition there is only one optimized selection: the one with the lowest possible expected statistical error; so we need to modify a bit our definition. This is done simply introducing a weight factor w to multiply $N_{\mathrm{bkg}}(\vec{\xi})$ in the procedure described in paragraph 4.2.1.

In this way when $w = 1$ we re-find the best possible selection; when $w < 1$ we obtain selections with higher efficiency but higher background and when $w > 1$ we find a purer selection. Now also the selections with $w \neq 1$ are optimized according to the new definition.

Varying w we can then find a whole set of different selections with different purities and construct a curve $N_{\mathrm{bkg}}(\varepsilon)$ that projected on the bi-dimensional surface $\delta\sigma^{\mathrm{exp}}_{\mathrm{stat}}(\varepsilon, N_{\mathrm{bkg}})$ gives us the best curve in the 3d-space shown in fig. 4.9.

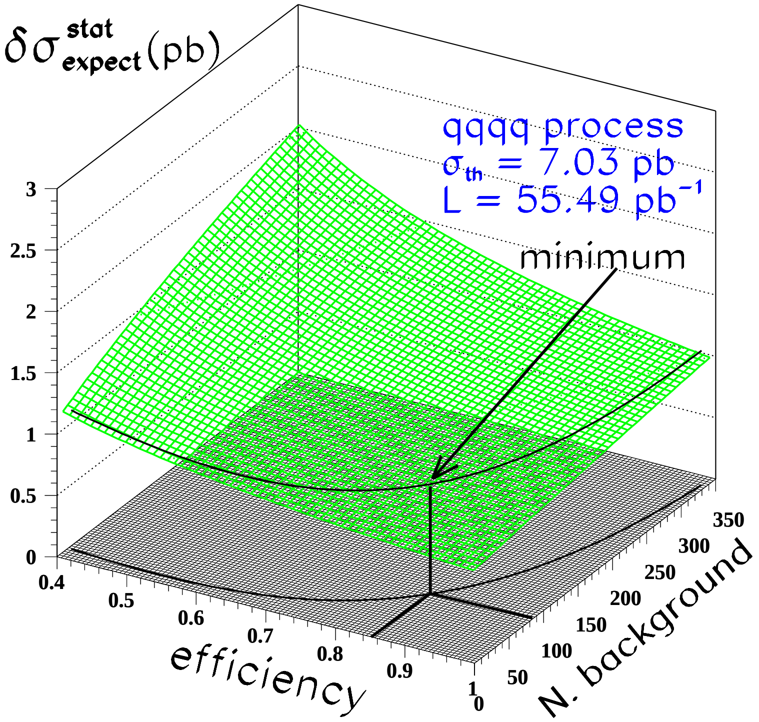

Figure 4.9: Curve $N_{\mathrm{bkg}}(\varepsilon)$ projected on the surface $\delta\sigma^{\mathrm{exp}}_{\mathrm{stat}}(\varepsilon, N_{\mathrm{bkg}})$.

Let $\xi_{i,j}$ be the i-th cut of the j-th selection, I require in this procedure that $\xi_{i,j}$ is a cut tighter than $\xi_{i,j-1}$. Then I can construct for each event a discrete variable WLIKE equal to the number of selections an event passes. By definition the greater is the value of WLIKE, the greater is the probability that the event belongs to the channel under study. Moreover the sum of the contents of the bins from bin j to bin j_{max} is equal to the number of events that pass the j-th selection, as we have seen in the previous example.

Performing several selections for each channel has another non negligible advantage; in fact with just one selection one may land in a peculiar region of data and background, therefore one needs to evaluate this effect, in the systematic errors computation, moving the cuts around their central position. On the other hand using several selections this

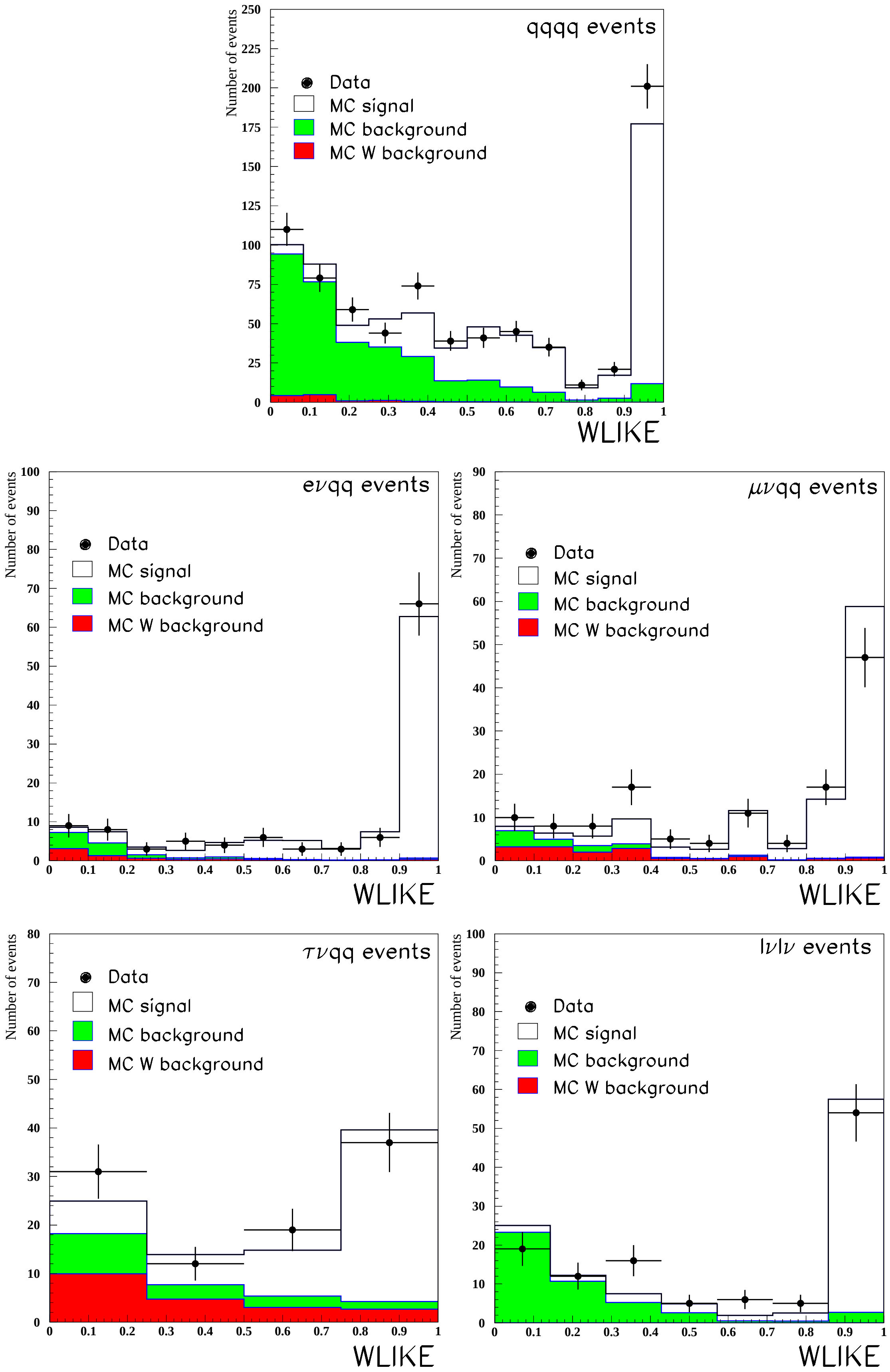

Figure 4.10: WLIKE variable distribution for the five final channels.

effect is averaged by definition.

Fig. 4.10 shows the distribution of the WLIKE variable for the five final channels of the W pairs production process I have obtained with this method. The details of this five channel selections will be described in the following chapter.

4.3 Global likelihood fit

The five distributions of the WLIKE variable for the different final states shown in fig. 4.10 contain all the information we need to extract the value of the cross sections. This can be done with a global fit minimizing the following likelihood function ℓ:

$$\ell = -2 \cdot \sum_{i=1}^{5} \sum_{k=1}^{N_i^{\text{bins}}} \ln \frac{e^{-\lambda_{ik}} \, \lambda_{ik}^{N_{ik}^{\text{data}}}}{N_{ik}^{\text{data}}!} \tag{4.1}$$

$$\lambda_{ik} = \sum_{j=1}^{5} \varepsilon_{ijk} \, \sigma_j \, \mathcal{L} + N_{ik}^{\text{bkg(no\_W)}} \tag{4.2}$$

where the indices i and j run over the 5 W-pair-decay-channels and k over the bins of the WLIKE distributions. N_i^{bins} is the number of bins in the histogram of the WLIKE variable related to the channel i, N_{ik}^{data} is the number of events selected in data for the i-th channel in the k-th bin, $N_{ik}^{\text{bkg(no\_W)}}$ is the number of background events, for the i-th channel in the k-th bin, coming from non W processes, σ_j (j=1,...,5) are the five free parameter to fit and ε_{ijk} is the selection efficiency of the channel j in the selection of the channel i in the bin k, and it is operatively defined as:

$$\varepsilon_{ijk} = \frac{N_{ijk}}{N_j^{\text{tot}}}$$

where N_{ijk} is the non normalized number of MC events belonging to the channel j that pass, in the k-th bin, the selection relative to the i-th channel, and N_j^{tot} is the total number of MC generated events for the j-th channel.

Chapter 5

W pair selections

In sec. 2.1 we have already discussed the three topologies related to the different final states of the W pair:

- $\mathrm{W^+W^-} \to \mathrm{q\bar{q}q\bar{q}}$ hadronic or "four jet" channel;
- $\mathrm{W^+W^-} \to \ell^-\bar{\nu}_\ell \mathrm{q\bar{q}}$ semileptonic channel ($\ell = \mathrm{e}, \mu, \tau$);
- $\mathrm{W^+W^-} \to \ell^-\bar{\nu}_\ell \ell^+\nu_\ell$ leptonic channel.

Since I have chosen to have three different selections for the semileptonic channel, according to the flavour of the lepton (exclusive selection), and one inclusive selection for the purely leptonic channel, I will write in the following of these five different final states:

$$\mathrm{e^+e^-} \to \mathrm{WW} \to \mathrm{q\bar{q}q\bar{q}},\quad \mathrm{e}\bar{\nu}\mathrm{q\bar{q}},\quad \mu\bar{\nu}\mathrm{q\bar{q}},\quad \tau\bar{\nu}\mathrm{q\bar{q}},\quad \ell^-\bar{\nu}\ell^+\nu$$

An inclusive selection is in general preferable when it takes advantages from the general characteristics of the event, like the presence of missing energy and so on. On the other hand it is worth performing an exclusive selection if it is based on lepton identification.

Most of the tools that are used for the analysis and the method applied to the cross section measurement has already been discussed in the previous chapters; in the following I will define some variables that are used for the final event selections, described in detail later on.

5.1 Topological variables

The visible energy E_{vis} has already been defined in sec. 3.4; the missing momentum vector $\vec{\mathrm{p}}_{\mathrm{miss}}$ is also important and is computed as the vector that added to the total reconstructed momentum results in a zero sum. The missing energy E_{miss} is defined as the module of the missing momentum.

The energy measured in the luminosity monitors, E_{LUM}, and in the ARL, E_{ALR}, is not taken into account in the computation of E_{vis} and E_{miss}.

Acoplanarity and acollinearity are defined as respectively the space angle and the angle in the r-φ plane formed by two particles or jets.

Sphericity and spherocity are two useful variables which describe the global shape of an event. Each event is assumed to be characterized by some identified leptons plus some calorimetric objects of momentum $\vec{p_i}$, with $i = 1, 2, \ldots, n$ an index running over the "particles" of the event.

The sphericity tensor is defined as [63]:

$$S^{\alpha\beta} = \frac{\sum_i p_i^{\alpha} \, p_i^{\beta}}{\sum_i |\vec{p_i}|^2}$$

where $\alpha, \beta = 1, 2, 3$ corresponds to the x, y and z components. By diagonalization of $S^{\alpha\beta}$ one find three eigenvalues $\lambda_1 \geq \lambda_2 \geq \lambda_3$, with $\lambda_1 \lambda_2 \lambda_3 = 1$. The sphericity of the event is defined as:

$$S = \frac{3}{2}(\lambda_2 + \lambda_3)$$

so that $0 \leq S \leq 1$. It represents the sum of the squared transverse momenta with respect to the event axis[1]; $S \simeq 0$ for a 2-jet event and $S \simeq 1$ for an isotropic event.

The spherocity is defined as [64]:

$$S' = \left(\frac{4}{\pi} \cdot \frac{\sum_i |p_i^{\perp}|}{\sum_i |\vec{p_i}|} \right)^2$$

where the transverse momenta $p^{\perp}$ are calculated respect to the axis that minimizes $\sum_i |p_i^{\perp}|$ (typically it is in the direction of the largest particle momentum); the factor $(4/\pi)^2$ gives an S'=1 normalization for a totally spherical event.

The spherocity, as the sphericity, measures the deviation from perfect two jet structure but it does not involve squared quantities in the sum, hence it is less sensitive to how the jet momentum is parceled out among the hadrons respect to the sphericity variable where the momenta are squared summed. For a more detailed comparison between sphericity and spherocity see reference [65].

5.2 Four jet selection

The fully hadronic channel $e^+e^- \rightarrow WW \rightarrow q\bar{q}q\bar{q}$ is characterized by four jets in the final state; fig. 5.1 shows a four jet candidate.

Each event is forced to four jets using the DURHAM algorithm described in sec. 3.2, and afterwards a constrained kinematical fit of the measured quantities is performed through a routine [66] which uses the method of the Lagrange multipliers and minimizes the χ^2 with an iterative procedure. The fit is performed imposing that the measured quantities satisfy four-momentum conservation (4C-fit); a further request of equal masses of the two reconstructed Ws can be imposed (5C-fit), where the W masses are computed from the jet pair that minimizes the χ^2; moreover the equal masses can be forced to be equal to the W mass estimate (80.4 GeV), in this case we have a fit with six constraints (6C-fit).

---

[1] The eigenvector corresponding to the λ_1 eigenvalue.

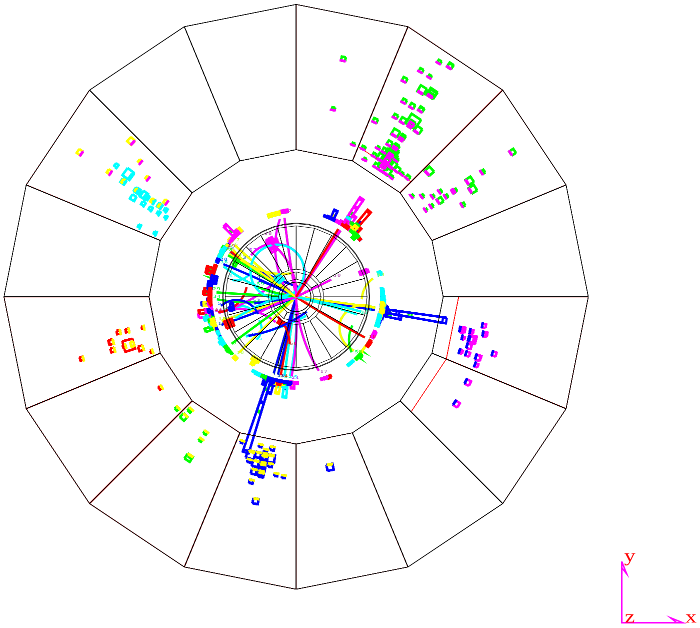

Figure 5.1: Candidate event for the four jet channel selection.

Since we do not know which is the jet pair that comes from the same W, the first problem to be faced in the four jet analysis is finding the algorithm which produces the maximum jet pairing efficiency. Matching the jets to the correct W is important only if variables, like M_W, which depend on the pairing are used for event selection.

I have studied several pairing algorithms on a four jet Monte Carlo sample, where I have also the informations of the generated quarks; I have selected a sub-sample of events with two jets reconstructed in a 0.2 rad half-cone around the direction of two generated quarks coming from the same W; then I have counted how many of the reconstructed jets are paired to the same W according to the different algorithm used (tab. 5.1):

1. Min $[\,|M_{W_1} - M_{W_2}|\,]$,
   this algorithm chooses as jet pair the one which minimizes the difference of the two W masses; the low pairing efficiency (tab. 5.1) is due to the fact that it favours equal masses regardless of their value;

2. Max $[M_{W_1} + M_{W_2} + \mathrm{Min}\,(M_{W_1}, M_{W_2})]$,
   it maximizes the sum of the two W masses and favours pairs with greater minimum W mass;

3. Max $[M_{W_1} + M_{W_2} - |M_{W_1} - M_{W_2}|]$,
   this algorithm favours jet pairing which produces equal W masses and which maximizes M_W at the same time;

4. χ^2 (5C-fit),
   jet pairing that minimizes the χ^2 with five constraints (four constraints from the four momentum conservation and one from the request of equal W masses);

5. χ^2 (6C-fit),
   jet pairing that minimizes the χ^2 with six constraints (four constraints from the four momentum conservation and two from the request of equal W masses and equal to 80.4 GeV).

Pairing algorithm	Pairing efficiency
Min $[\,|M_{W_1} - M_{W_2}|\,]$	64.0%
Max $[M_{W_1} + M_{W_2} + \text{Min}\,(M_{W_1}, M_{W_2})]$	68.0%
Max $[M_{W_1} + M_{W_2} - |M_{W_1} - M_{W_2}|]$	78.5%
χ^2 (5C-fit)	72.5%
χ^2 (6C-fit)	85.2%

Table 5.1: Pairing algorithms and the relative pairing efficiency.

Tab. 5.1 shows that the best jet pairing comes from the 6C-fit algorithm.

Now we must study if the distributions of the Monte Carlo variables used both for signal and background are in agreement with data and this can be done comparing data and Monte Carlo distributions for a selection with a very high background contamination, so that possible disagreements are amplified.

For this purpose I have selected events using the following cuts:

- $E_{\text{vis}} \geq 90$ GeV
- $E_{\text{miss}} \leq 60$ GeV
- $N_{\text{ASRC}} \geq 25$
- $Y_{34} \geq 0.0015$

where E_{vis} and E_{miss} have already been defined in sec. 5.1, N_{ASRC} is the total number of ASRCs in the event and Y_{34} represents the minimum value of the y_{ij} (defined in sec. 3.2, with the indices i and j running over the four jets) that comes from forcing the event in four jets; the name Y_{34} stems from the fact that this represents the value of y_{cut} that forces the event from having three to having four reconstructed jets.

The results of this simple preselection are:

Number of selected data = 1249
Number of Monte Carlo signal events = 381.4
Number of all background events (except $\gamma\gamma$ events) = 840.5
Number of $\gamma\gamma$ background events = 144.2

where the $\gamma\gamma$ background has been generated with PHOJET; all the other possible background sources are listed in tab. 2.1.

These numbers show that there is some disagreement between data and Monte Carlo, as one can also see from fig. 5.2 where some variables related to such a selection are displayed; $\cos\vartheta_{\rm miss}$ represents the $\cos\vartheta$ of the missing momentum, $M_{jj}^{-\gamma}$ is the invariant mass of the event forced to two jets after that an isolated photon of energy greater than 30 GeV, if present, has been subtracted, $M_W^{\rm 5C-fit}$ and $\chi^2_{\rm 5C-fit}$ are the W mass and the χ^2 that comes out from the fit with 5 constraints described above.

It is however evident that the disagreement is limited to the regions with high $\gamma\gamma$ background. The same variables with a $\gamma\gamma$ background reduced by hand by a factor 5.4 are shown in fig. 5.3 and show a very good agreement in all the distributions. The factor 5.4 is simply the value that equalizes data and Monte Carlo expected events.

Some theoretical aspects of the problems related to the Monte Carlo $\gamma\gamma$ events have been discussed in sec. 2.2.2. The low quality of the $\gamma\gamma$ event simulation will be taken into account in the evaluation of the systematic errors.

The high level of background contamination shown in fig. 5.3 is mainly due to the fact that the cross section of the $\rm e^+e^- \to q\bar{q}(\gamma)$ background is about 15 times the signal one. Moreover the shape of the background distributions is often tangled with the signal one; fig. 5.3 shows hence the starting point from which we want to extract the signal.

As already discussed in sec. 4.2 the signal efficiency and the level of background we allow in the selection are chosen by the optimization program in order to minimize the statistical error of the cross section measurement.

5.2.1 Optimized selection

Starting with the preselected sample previously described I have looked for the variables that better discriminate signal from background; for this purpose I have used the optimization procedure described in sec. 4.2. I have run the optimization using 29 variables; most of these are correlated and others are redundant, but, as I have already discussed in sec. 4.2.1, the optimization program takes care of disentangling the correlations and of dropping the redundant variables.

For completeness I list here the variables that I have used at this first step: the visible energy, the energy deposited in the luminosity monitors and in the ALR, the missing energy, the missing momentum projected along the beam pipe normalized to the visible energy, the $\cos(\vartheta)$ of the missing momentum, the number of ASRCs and the number of tracks in the event, the energy of a possible isolated photon or muon, the sphericity and spherocity of the event, Y_{34}, the χ^2 of the fit at four, five and six constraints, the W mass output of the 5C-fit, the number of reconstructed jets by the JADE algorithm with y_{cut}=0.02, the minimum number of ARSC present in a jet, the invariant mass of the event forced to two jets, $M_{jj}^{-\gamma}$, the maximum and the minimum jet energy, the minimum angle between two jets, the mass of the two Ws, the sum and the difference of the two W masses, the minimum and maximum angle between two jets coming from the same W.

The variables that use informations of the jet pairing have been constructed using the 6C-fit pairing, since it has the best performance. The jet variables (energy and angular informations) are obtained from the 4C-fit.

I have first run the optimization routine with a weight factor $w = 1$ (see sec. 4.2.2),

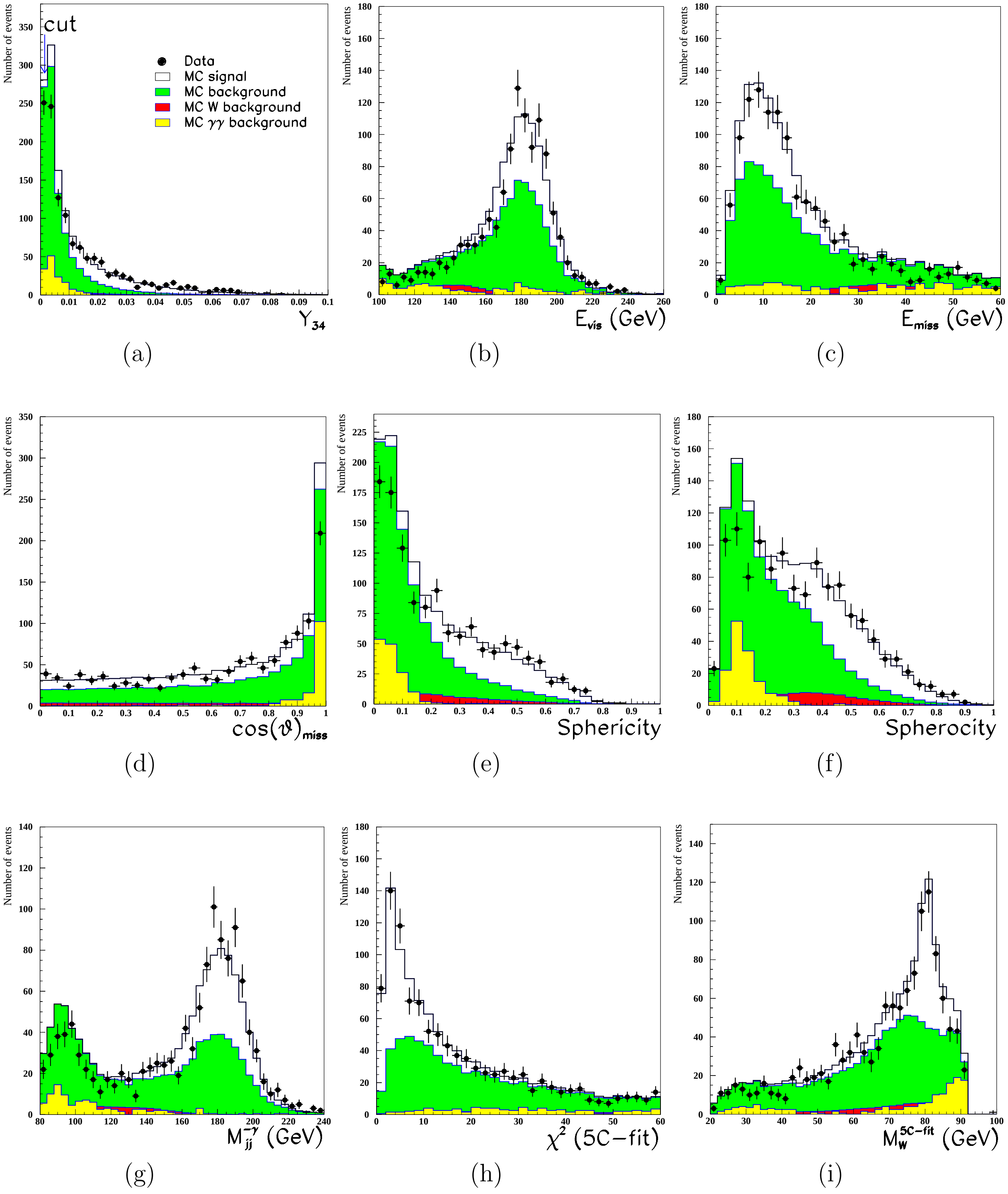

(a) (b) (c)

(d) (e) (f)

(g) (h) (i)

Figure 5.2: Comparison of data with Monte Carlo expectation from some variables whose meaning is explained in the text; the background coming from WW processes and from the $\gamma\gamma$ process are superimposed on the total background to remark possible discrepancies.

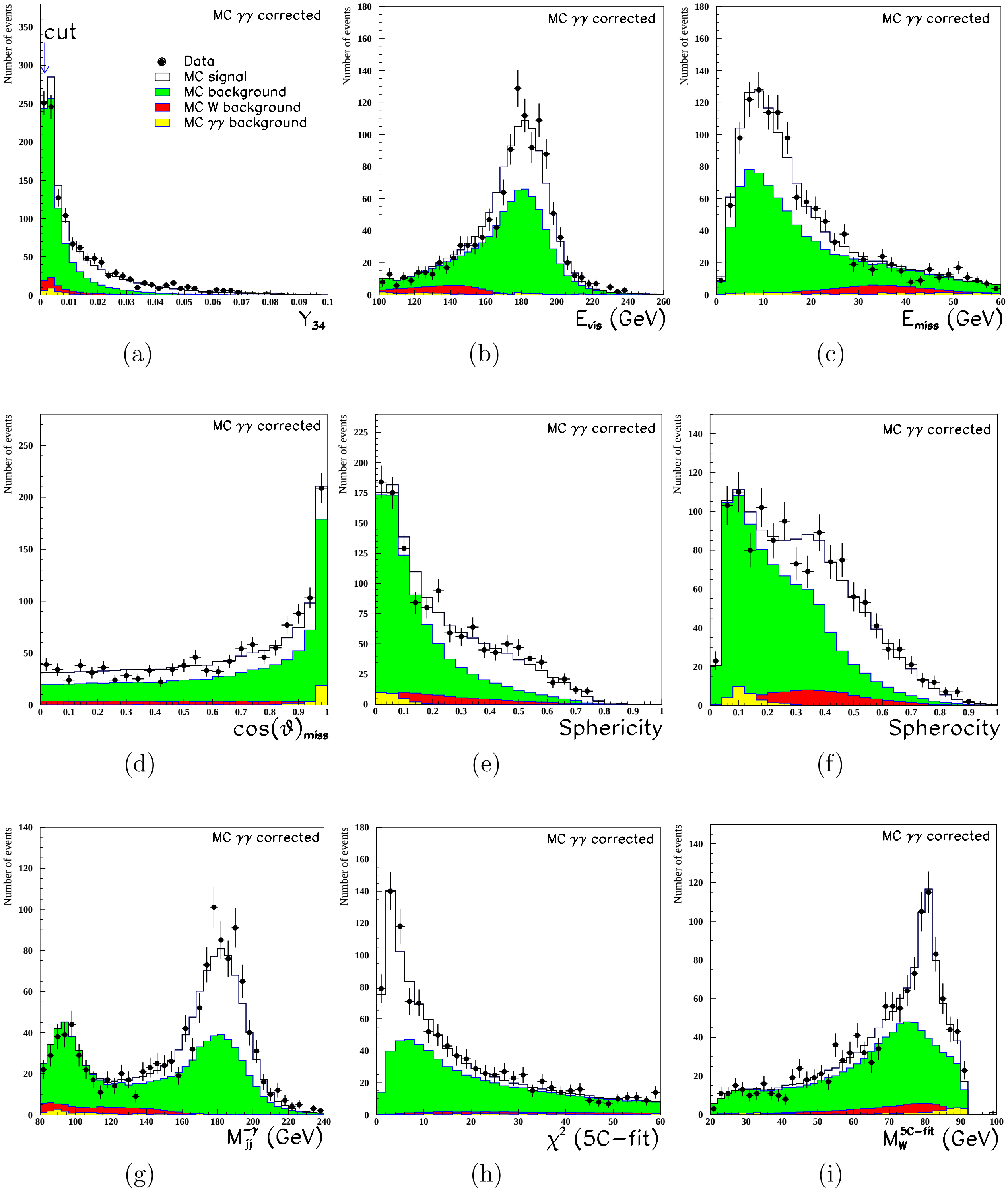

(a) (b) (c)

(d) (e) (f)

(g) (h) (i)

Figure 5.3: The same distributions of the previous figure where now the $\gamma\gamma$ background has been reduced by hand by a factor 5.4.

and I have found that 14 of these variables are useless or bring a very small improvement to our goal: that of having the lowest possible statistical error. Once such variables have been dropped, the results of this optimized selection are shown in tab. 5.2 and in fig. 5.4, 5.5. The number of Monte Carlo expected events, $N_{\rm sig}^{\rm MC}$, and the signal efficiency, ε, have been evaluated using KORALW simulated events, the number of expected background events has been estimated using Monte Carlo events simulated for all the processes listed in tab. 2.1 and is almost completely due to $\mathrm{q\bar{q}}(\gamma)$ events ($\sim 88\%$) and ZZ events ($\sim 10\%$); the remaining is shared between Zee and WW $\rightarrow \tau\bar{\nu}\mathrm{q\bar{q}}$, $\mathrm{e}\bar{\nu}\mathrm{q\bar{q}}$ events.

ε	$=$	84.9%	
$N_{\rm back}^{\rm MC}$	$=$	88.9	
$N_{\rm sig}^{\rm MC}$	$=$	331.1	$\Delta\left(\delta\sigma_{\rm stat}^{\rm exp}\right)$
$N_{\rm DATA}$	$=$	467	
Spherocity	$\geq$	0.2120	$1.47 \cdot 10^{-2}$
$N_{\rm ASRC}^{\rm min}$ in jet	$\geq$	3	$1.03 \cdot 10^{-2}$
$\chi^2_{\rm 5C-fit}$	$\leq$	38.6	$6.82 \cdot 10^{-3}$
$\chi^2_{\rm 4C-fit}$	$\leq$	11.2	$2.18 \cdot 10^{-3}$
$M_{jj}^{-\gamma}$	$\geq$	113.2 GeV	$1.95 \cdot 10^{-3}$
Y_{34}	$\geq$	0.0027	$1.88 \cdot 10^{-3}$
E_γ	$\leq$	50.0 GeV	$1.34 \cdot 10^{-3}$
Sphericity	$\geq$	0.0763	$9.29 \cdot 10^{-4}$
$E_{\rm jet}^{\rm min}$	$\geq$	10.0 GeV	$6.58 \cdot 10^{-4}$
$N_{\rm ASRC}$	$>$	40.0	$6.43 \cdot 10^{-4}$
E_μ	$\leq$	40.0 GeV	$5.99 \cdot 10^{-4}$
$\alpha_{\rm jj}^{\rm min}$	$\geq$	0.270 rad	$4.24 \cdot 10^{-4}$
$E_{\rm LUM+ALR}$	$\leq$	31.1 GeV	$3.97 \cdot 10^{-4}$
$E_{\rm miss}$	$\leq$	45.0 GeV	$3.90 \cdot 10^{-4}$
$N_{\rm track}$	$\geq$	0	0

Table 5.2: Efficiency, ε, number of expected background, $N_{\rm back}^{\rm MC}$, and signal, $N_{\rm sig}^{\rm MC}$, number of selected data, $N_{\rm DATA}$ and the value of the cut for the 15 variable used for the optimized selection; on the right side of each cut the $\Delta\delta\sigma_{\rm stat}^{\rm exp}$ is reported; see text for an explanation of the cut on $N_{\rm track}$.

Most of the variables in tab. 5.2 and in fig. 5.4, 5.5 have already been defined; $E_{\rm LUM+ALR}$ represents the energy deposited in the luminosity monitors and in the ALR, $N_{\rm ASRC}$ and $N_{\rm track}$ respectively the number of ASRC and tracks in the event, E_γ and E_μ the energy of the possible more energetic isolated photon or muon and $\alpha_{\rm jj}^{\rm min}$ is the minimum angle between jets.

The distributions reported in fig. 5.4 and 5.5 represent the "n-1 histograms", that is the histograms with all the cuts applied except the cut on the plotted variable.

In tab. 5.2 I have also reported the $\Delta(\delta\sigma_{\rm stat}^{\rm exp})$ related to each cut; we see that the most powerful cuts are the spherocity and the minimum number of ASRC in the jet ($N_{\rm ASRC}^{\rm min}$

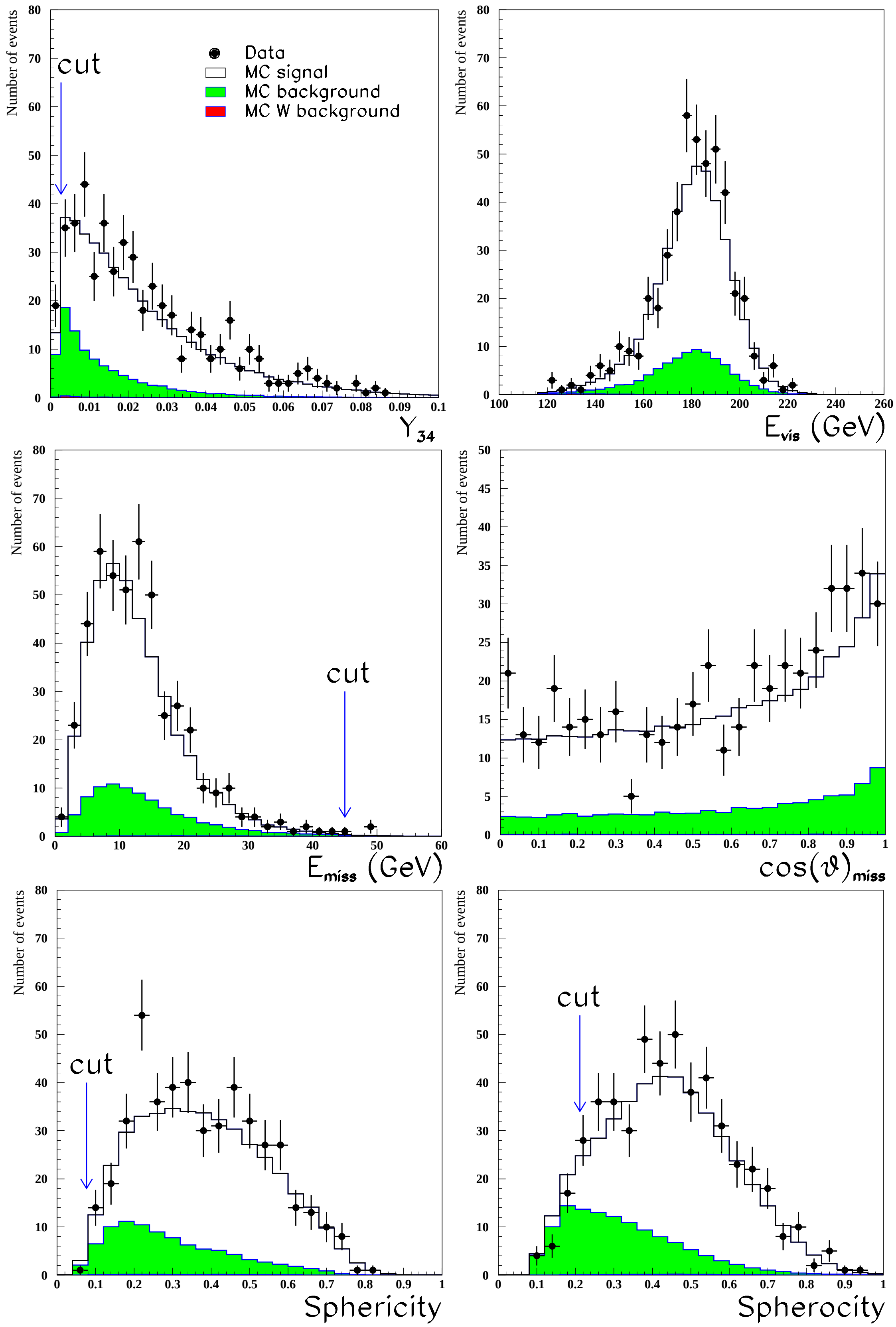

Figure 5.4: Distributions of some variables used in the four jet selection.

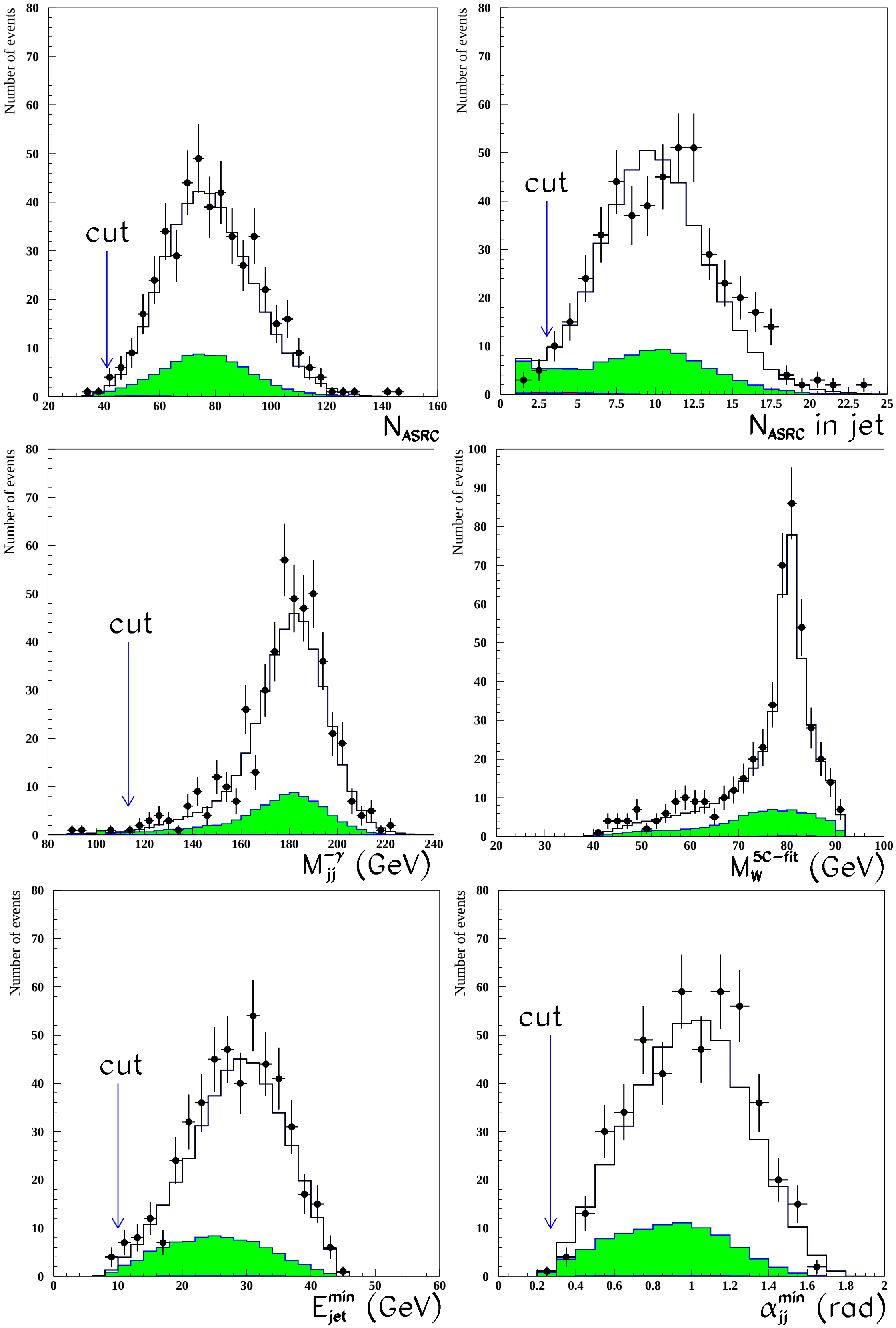

Figure 5.5: Distributions of some variables used in the four jet selection.

in jet), as we can also infer from the n-1 histograms in fig. 5.4 and 5.5. On the other hand the variables with a low value of $\Delta\delta\sigma^{\mathrm{exp}}_{\mathrm{stat}}$ just cut on the tails of the background distributions.

I want to remark here that none of the these variables used for the final selection depend on the jet-jet pairing and therefore the results are independent of the pairing algorithm used.

The cut on N_{track} at zero deserves an observation; in order to increase the selection efficiency, if N_{track} is less then 3 I drop the event only if either the total energy in the BGO is less then 50 GeV or the total energy in the HCAL is less then 15 GeV. This is done so as not to lose good four jet events occurred when the TEC was off ($\sim 5\%$ of times). That is the reason why the $\Delta(\delta\sigma^{\mathrm{exp}}_{\mathrm{stat}})$ of this variable is zero; anyway the cut is not dropped since it is used for the other selections with $w > 1$.

After the study of a single optimized selection (w=1), I pass to the multi-cuts method; I look for optimized selections with this sub-set of 15 variables, moving the weight w from 0.05 (very loose selection), to 1000 (very tight selection). Tab. 5.3 shows the results obtained; as expected the selection with $w = 1$ has the lowest $\delta\sigma^{\mathrm{exp}}_{\mathrm{stat}}$.

Using this set of 12 selections I can build the WLIKE variable (fig. 5.6), defined in sec. 4.2.2, from which, together with the WLIKE distributions of the other W final state channels (sec. 4.3), I will extract the $e^+e^- \to WW \to q\bar{q}q\bar{q}$ cross section.

Fig. 5.6 shows a slight excess of data limited to the bin corresponding to the purest selection.

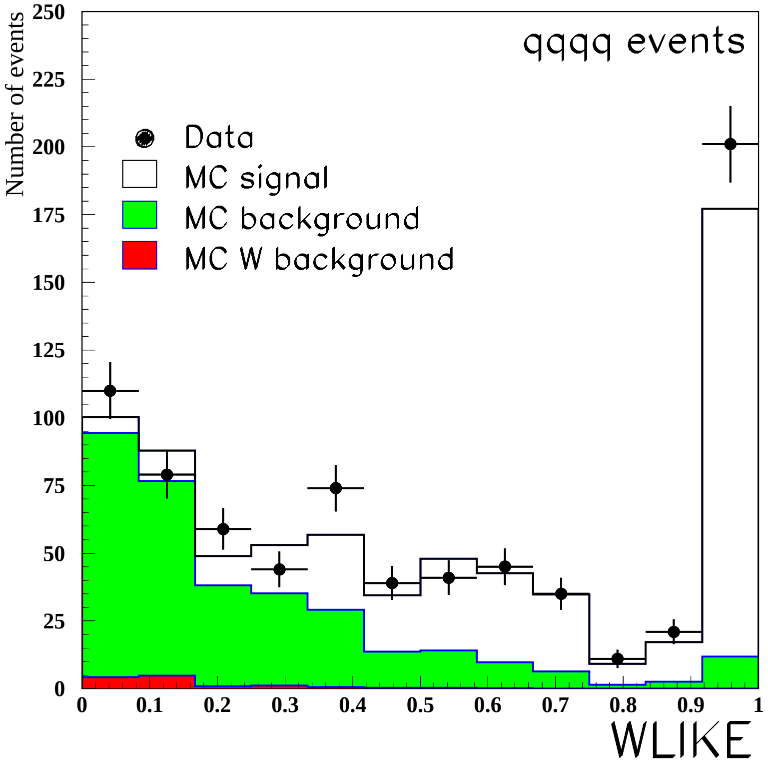

Figure 5.6: WLIKE distribution for the four jet channel.

Weight w	$=$	0.05	0.1	0.3	0.5	1	3	5	10	25	50	100	1000
ε	$=$	96.7%	95.2%	92.3%	89.5%	84.9%	77.8%	72.5%	63.8%	55.4%	48.1%	46.1%	42.4%
$N_{\rm back}^{\rm MC}$	$=$	333.1	238.8	162.2	124.1	88.9	59.7	46.1	31.9	22.2	15.8	14.4	11.9
$N_{\rm sig}^{\rm MC}$	$=$	377.1	371.2	359.8	349.0	331.1	303.5	282.7	248.9	215.9	187.6	179.8	165.1
$N_{\rm DATA}$	$=$	759	649	570	511	467	393	354	313	268	233	222	201
$\delta\sigma_{\rm stat}^{\rm exp}$ (pb)	$=$	1.012	0.954	0.912	0.896	0.889	0.905	0.926	0.975	1.036	1.106	1.128	1.186
$E_{\rm LUM+ALR}$	$\leq$	57.0	43.0	32.1	32.0	31.1	25.9	25.5	16.9	16.2	12.8	12.7	12.7
$E_{\rm miss}$	$\leq$	59.8	59.0	47.0	46.0	45.0	39.0	36.2	34.5	34.4	30.2	30.1	30.0
$N_{\rm ASRC}$	$>$	30	34	37	38	40	40	40	40	40	40	40	40
$N_{\rm track}$	$\geq$	0	0	0	0	0	16	16	16	16	16	16	16
E_γ	$\leq$	50.4	50.3	50.2	50.1	50.0	47.2	47.1	47.0	45.7	38.5	38.4	36.5
E_μ	$\leq$	58.0	48.1	48.0	40.1	40.0	39.6	39.5	39.0	32.0	32.0	31.7	30.0
Spherocity	$\geq$	0.090	0.1301	0.1500	0.1843	0.2120	0.2443	0.2704	0.3343	0.3350	0.3679	0.3765	0.3780
Sphericity	$\geq$	0.019	0.0437	0.0625	0.0630	0.0763	0.1063	0.1250	0.1260	0.1261	0.1262	0.1263	0.1265
Y_{34}	$\geq$	0.0015	0.0016	0.0017	0.0022	0.0027	0.0039	0.0041	0.0049	0.0068	0.0069	0.0070	0.0072
$\chi^2_{\rm 4C-fit}$	$\leq$	29.4	24.5	14.8	14.7	11.2	11.2	11.1	10.2	10.2	10.2	10.1	10.1
$\chi^2_{\rm 5C-fit}$	$\leq$	176.3	124.0	67.0	57.5	38.6	30.0	29.5	29.0	15.0	14.9	13.9	10.8
$N_{\rm ASRC}^{\rm min}$ in jet	$\geq$	2	2	3	3	3	3	4	4	4	4	4	4
$M_{jj}^{-\gamma}$	$\geq$	107.8	108.0	108.5	110.5	113.3	116.5	117.0	126.0	126.0	127.0	127.1	127.2
$E_{\rm jet}^{\rm min}$	$\geq$	4.5	4.5	7.5	9.6	10.0	12.5	15.9	16.0	16.5	19.9	19.9	19.9
$\alpha_{\rm jj}^{\rm min}$	$\geq$	0.240	0.241	0.252	0.255	0.270	0.330	0.345	0.435	0.435	0.570	0.570	0.570

Table 5.3: In this table we report for each of the 12 selection the weight, w, the efficiency, ε, the number of expected background, $N_{\rm back}^{\rm MC}$ and signal, $N_{\rm sig}^{\rm MC}$, the number of selected data, $N_{\rm DATA}$, the expected statistical error, $\delta\sigma_{\rm stat}^{\rm exp}$, and the value of the cut for the 15 variable used. All energies are supposed to be measured in GeV.

5.3 $e\bar{\nu}q\bar{q}$ selection

The $e^+e^- \rightarrow WW \rightarrow e\bar{\nu}q\bar{q}$ events are characterized by two identified jets and an electron (in the BGO or in the EGAPs) in the final state; moreover there is missing energy due to the undetected neutrino. A candidate event is shown in fig. 5.7 where one can see the isolated bump in the BGO matched with a TEC track, and two narrow bundles of hadronic particles pointing roughly to the same direction, reconstructed as two jets.

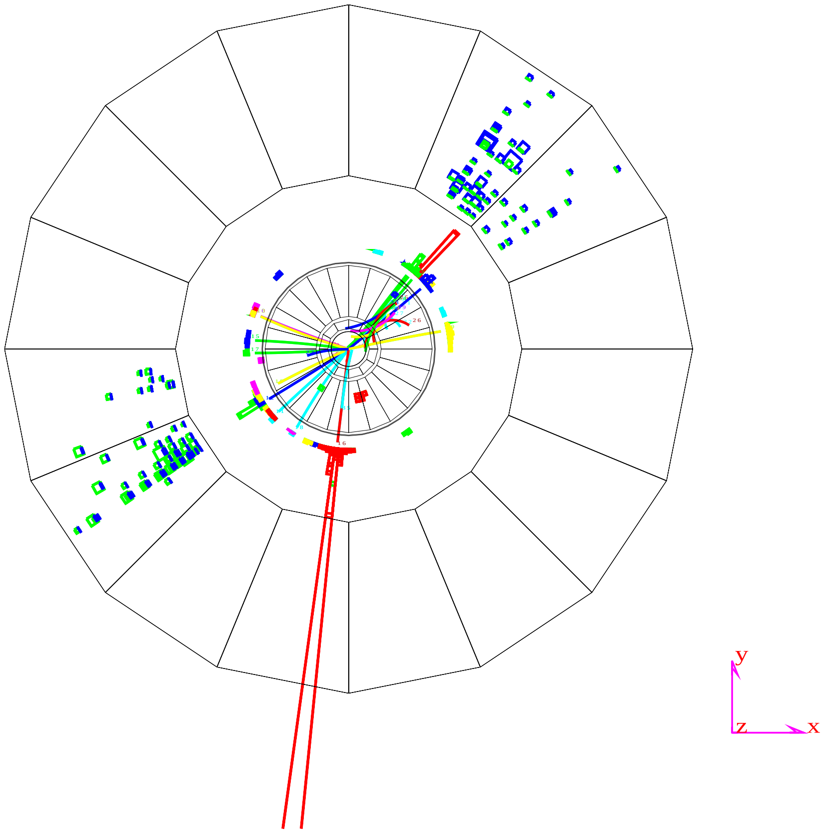

Figure 5.7: Candidate event for the semileptonic selection of $e^+e^- \rightarrow WW \rightarrow e\bar{\nu}q\bar{q}$ events.

The most dangerous backgrounds to this channel comes from the $e^+e^- \rightarrow \tau\bar{\nu}_\tau q\bar{q}$ process when the τ decays in an electron and from the $e^+e^- \rightarrow Z/\gamma \rightarrow q\bar{q}(\gamma)$ when the photon is wrongly matched to a TEC track and is therefore mistaken for an electron.

In the former the original energy of the tau is shared by the electron and the neutrinos in the final state, so it can be distinguished from the signal with a cut on the electron energy; however $\tau\bar{\nu}_\tau q\bar{q}$ events with energetic electrons constitute an irreducible background.

The $e^+e^- \rightarrow Z/\gamma \rightarrow q\bar{q}(\gamma)$ process has a cross section about 50 times greater than the signal one; that is the reason why mistaking a photon for an electron may introduce a big contamination in the selection.

It is therefore important in this selection the choice of the electron isolation criteria and the quality of the matching between the BGO bump and the TEC track.

I have performed the optimization in three steps. In the first step I have determined the isolation variables minimizing the expected statistical error with only $q\bar{q}(\gamma)$ and WW→ $q\bar{q}q\bar{q}$, $\mu\bar{\nu}q\bar{q}$ as background processes, because in these background processes there is no electron present (as there is in WW→ $\tau\bar{\nu}q\bar{q}$ events); however since these represent roughly half the background I expect in the final sample I have used a background weight $w = 2$.

In the second step I have added the search of electrons in the EGAP regions to the previous selection, and I have optimized the variables related to the isolation and identification of electrons in EGAPs on the previous sub-sample of background.

The electron identification and isolation criteria determined in such steps are listed in Appendix B.1, and are fixed in the last step where I determine the remaining variables by optimizing the whole selection using all the background sources.

At this optimization level I use as Monte Carlo signal the events generated with KORALW generator since it contains just the diagrams of the searched signal; once the selection is determined the cross section measurement is performed using EXCALIBUR, that contains all the 4 fermions diagrams, and the correction factor described in sec. 2.1.6.

Varying the weight w from 0.1 to 1000 I have obtained the 10 selections shown in tab. 5.4, where I have reported for each selection the signal efficiency ε and the expected number of signal events $N_{\rm sig}$ estimated both on KORALW and EXCALIBUR Monte Carlo samples, the expected number of background events $N^{\rm MC}_{\rm back}$, the number of data $N_{\rm DATA}$ selected and the expected statistical $\delta\sigma^{\rm exp}_{\rm stat}$.

In each selection reported in tab. 5.4 about 45% of background comes from $e^+e^- \rightarrow$ WW $\rightarrow \tau\bar{\nu}q\bar{q}$, 35% from $e^+e^- \rightarrow q\bar{q}(\gamma)$ and 15% from the Zee process; the remaining is shared between the ZZ and $e^+e^- \rightarrow$ WW $\rightarrow \mu\bar{\nu}q\bar{q}$ processes.

The lower value of the EXCALIBUR efficiency, compared to the KORALW one, is due to the rejection of events that come from 4f diagrams different from CC03. It is worth to note that the expected signal number from EXCALIBUR is less that the one from KORALW for each selection even if the 4f cross section is greater then the CC03 cross section; this is due to a negative interference of some 4f diagrams with the CC03 ones in the kinematical regions of the searched signal.

Tab. 5.4 shows also the variables used and the value of the applied cuts for each selection; $E_{\rm el}$ and $\vartheta_{\rm el}$ represent respectively the electron energy and polar angle, M_{jj} and $M_{e\nu}$ are the jet-jet and electron-neutrino invariant masses (the neutrino energy and direction are inferred from the missing momentum), $p^{\perp}_{\rm miss}$ represents the missing transverse momentum; the two selections labelled with BGO and EGAP refer respectively to the search of the electron in the BGO or in the EGAPs, and the total selection is the logic OR of the two.

Fig. 5.9 shows the "n-1" histograms of some variables used in the selection, together with the cuts chosen by the optimization program for the selection with $w = 1$; we see that only the cut on $M_{e\nu}$ (and the cut on $\cos(\vartheta)_{\rm miss}$, not shown here) has a non negligible effect in the background rejecting, the others just drop some background events in the tails of the distributions.

The low level of background contamination in such "n-1" histograms is due mainly to two reasons; the first is that all the optimization procedure, and also the histograms, have been performed on a pre-selected sample of events, the second reason is that most

Weight w	$=$	0.1	0.5	1.	3.	5.	10.	25.	50.	100.	1000.
$\varepsilon^{\mathrm{KORALW}}$	$=$	77.2%	76.0%	73.6%	71.9%	70.2%	66.8%	63.0%	59.0%	56.5%	50.4%
$\varepsilon^{\mathrm{EXCALIBUR}}$	$=$	62.9 %	61.9%	60.0%	58.7%	57.4%	54.9%	51.7%	48.5%	46.5%	41.6%
$N_{\mathrm{back}}^{\mathrm{MC}}$	$=$	16.9	9.7	5.1	3.6	2.9	1.9	1.4	1.1	0.9	0.7
$N_{\mathrm{sig}}^{\mathrm{MC\,KORALW}}$	$=$	97.8	96.4	93.3	91.1	88.9	84.7	79.8	74.8	71.6	63.9
$N_{\mathrm{sig}}^{\mathrm{MC\,EXCALIBUR}}$	$=$	93.7	92.4	89.5	87.5	85.6	81.9	77.2	72.3	69.3	62.1
N_{DATA}	$=$	113	104	96	93	88	84	78	75	72	66
$\delta\sigma_{\mathrm{stat}}^{\mathrm{exp}}$ (pb)	$=$	0.524	0.512	0.511	0.513	0.518	0.529	0.545	0.563	0.576	0.611
BGO		cut									
E_{vis}	$\leq$	203.0	201.5	201.0	199.0	198.0	191.0	190.5	190.0	189.0	188.0
E_{vis}	$\geq$	85.9	89.0	90.1	90.5	91.0	91.5	99.1	99.9	103.4	103.5
N_{ASRC}	$>$	12	12	12	15	15	15	15	17	19	19
$\cos(\vartheta)_{\mathrm{miss}}$	$\leq$	0.975	0.970	0.970	0.963	0.948	0.933	0.933	0.915	0.915	.898
E_{miss}	$\geq$	11.2	14.0	17.4	18.9	20.3	20.3	22.3	23.6	24.0	24.4
N_{track}	$>$	6	6	6	6	6	6	8	8	8	9
E_{el}	$\geq$	12.5	20.5	21.0	21.1	21.2	21.3	21.4	21.5	22.0	26.1
$\cos(\vartheta)_{\mathrm{el}}$	$\leq$	0.971	0.970	0.957	0.957	0.956	0.956	0.956	0.956	0.956	.955
M_{jj}	$\geq$	23.9	25.3	25.6	46.3	47.5	47.6	54.3	58.8	59.0	60.4
$M_{e\nu}$	$\geq$	45.2	54.1	60.0	63.9	66.3	69.2	70.9	72.8	73.2	75.3
$\mathrm{p}_{\mathrm{miss}}^{\perp}$	$\geq$	5.5	6.0	11.1	11.2	11.3	14.5	16.1	17.0	19.7	19.8
EGAP		cut									
E_{vis}	$\leq$	195.5	195.4	193.0	188.0	186.0	185.5	185.0	184.5	184.0	168.8
E_{vis}	$\geq$	86.0	87.0	88.0	88.2	98.8	100.0	100.2	100.5	100.8	101.0
N_{ASRC}	$>$	14	14	14	14	14	15	16	16	16	16
N_{track}	$>$	5	5	5	5	5	5	5	5	5	5
E_{miss}	$\geq$	8.9	11.5	15.0	15.5	16.0	16.5	16.6	16.8	16.9	20.5
$\cos(\vartheta)_{\mathrm{miss}}$	$\leq$	0.977	0.977	0.976	0.976	0.976	0.955	0.955	0.954	0.953	.952
$\mathrm{p}_{\mathrm{miss}}^{\perp}$	$\geq$	5.0	6.0	10.0	10.3	10.5	10.8	16.3	16.3	16.4	16.5
E_{el}	$\geq$	20.0	20.1	21.5	21.7	22.0	22.1	22.2	22.3	22.4	33.6
M_{jj}	$\geq$	20.0	31.1	31.2	31.3	31.4	31.5	31.6	31.7	32.0	49.2
$M_{e\nu}$	$\geq$	20.0	27.3	46.3	46.3	46.5	53.8	68.1	68.5	69.0	70.0

Table 5.4: Performances of the 10 selections and values of the used cuts; the efficiencies and number of expected events from Monte Carlo are reported both for KORALW than EXCALIBUR. All energies are supposed to be measured in GeV.

of the background is rejected at the level of the electron identification and isolation, that is at the first and second step of optimization.

Fig. 5.8 shows the WLIKE distribution constructed from the 10 $e\bar{\nu}q\bar{q}$ selections; it shows a very good agreement between selected and expected number of events for each selection.

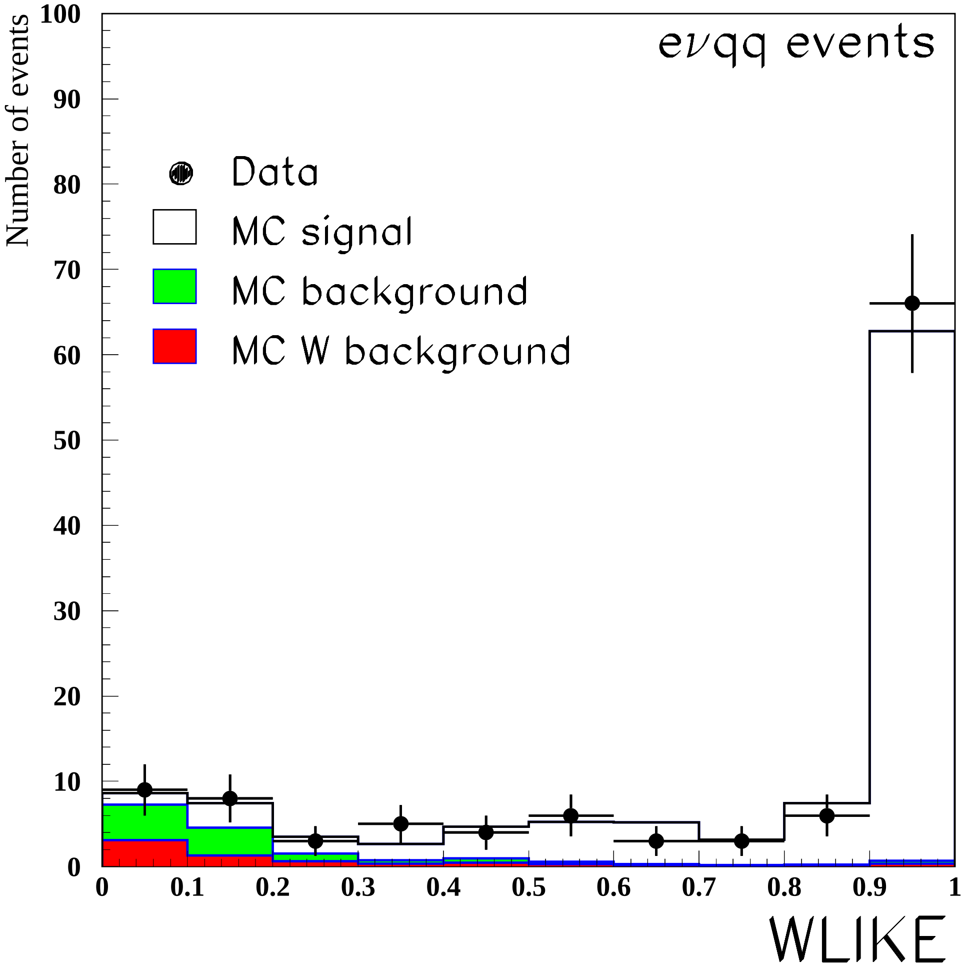

Figure 5.8: WLIKE distribution for the $e^+e^- \to WW \to e\bar{\nu}q\bar{q}$ semileptonic channel.

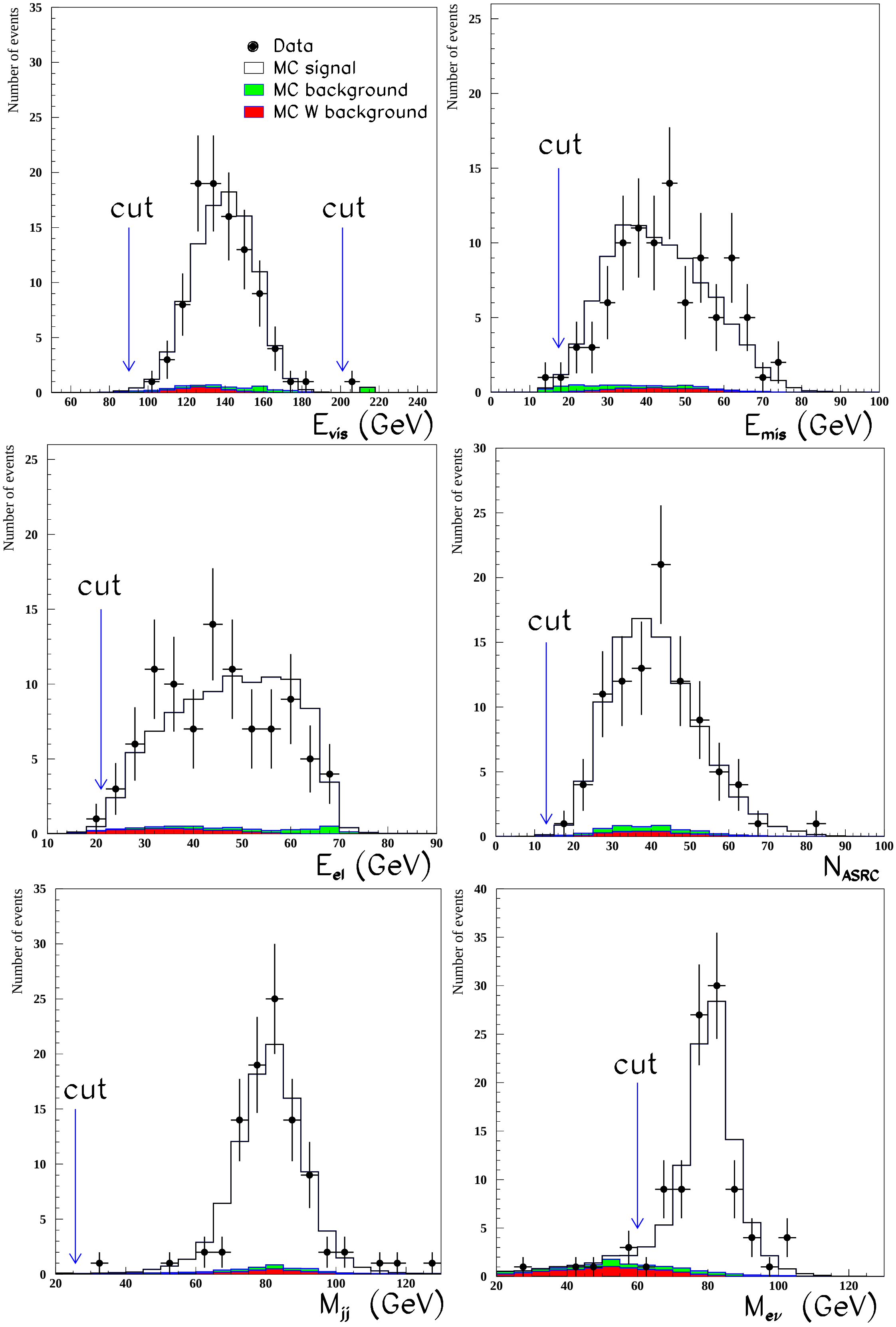

Figure 5.9: Distributions of some variables used for the e$\bar{\nu}$q$\bar{\text{q}}$ selection.

5.4 $\mu\bar{\nu}q\bar{q}$ selection

The $e^+e^- \rightarrow WW \rightarrow \mu\bar{\nu}q\bar{q}$ events are characterized by two identified jets in the final state, a muon reconstructed either as a an AMUI or a MIP, and some missing energy due to the undetected neutrino; a candidate event is shown in fig. 5.10.

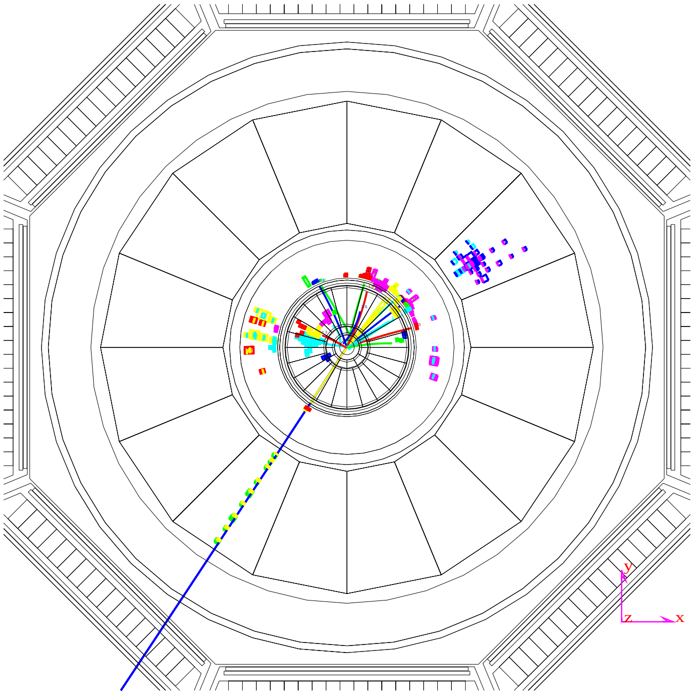

Figure 5.10: Candidate event for the semileptonic selection of $e^+e^- \rightarrow WW \rightarrow \mu\bar{\nu}q\bar{q}$ events.

The main background source to this selection comes from the $e^+e^- \rightarrow \tau\bar{\nu}q\bar{q}$ process when the tau decays in a muon; the events where the muon has almost entirely the tau energy are indistinguishable from the signal.

Another non negligible background source is represented by the $e^+e^- \rightarrow Z\gamma \rightarrow q\bar{q}(\gamma)$, especially when the photon is lost and a muon, coming from a semileptonic decay of a heavy hadron inside a jet, is present; these events are almost entirely rejected by the tight isolation cut imposed, but such a background is anyway dangerous because the cross section of this process is about 50 times greater than the signal one.

As for the $e\bar{\nu}q\bar{q}$ channel I have performed the optimization in three steps; in the first and second step I have determined the cuts on the identification and isolation variables of the muon, reconstructed respectively as an AMUI and a MIP and I have dropped the redundant variables; in the third step I have fixed the identification variables and I have optimized the whole selection (both with AMUI then MIP) with the remaining "global" variables of the event reported in tab. 5.5.

The muon identification criteria fixed by the first two steps are listed in Appendix B.2.

Tab. 5.5 shows the results of the final optimization, that is the 10 optimized selections I have found varying the background weight factor w from 0.5 to 1000. For each selection the efficiency, the number of expected and found events, and the expected statistical error are reported. Moreover the variables used both for the AMUI and for the MIP selection are reported (the final selection being the logic OR of the two).

About 65% of the total background is due to $e^+e^- \rightarrow WW \rightarrow \tau\bar{\nu}q\bar{q}$ and about 20% to the $q\bar{q}(\gamma)$ process; the remaining is shared between the ZZ and $e^+e^- \rightarrow WW \rightarrow e\bar{\nu}q\bar{q}$ processes.

Most of the variables shown in tab. 5.5 have already been defined in the previous text, E_μ and E_{mip} represent respectively the AMUI and the MIP energy, α is the angle between the muon and the nearest jet and $M_{\mu\nu}$ is the muon-neutrino invariant mass.

Fig. 5.12 and 5.13 show the "n-1" histograms of some variables used for the selection with the background weight factor w=1. One can see that the most powerful cuts are those based on the variables $M_{\mu\nu}$, $\alpha\sin(\vartheta)_{\mathrm{miss}}$, E_μ and E_{MIP}. The histograms without cuts are shown for comparison between data and Monte Carlo distributions. No cut is applied on the N_{track} distribution in order to recover events where the TEC high voltage is off. The 10 optimized selections are used to construct the WLIKE variable shown in fig. 5.11, which will be then fitted to extract the cross section.

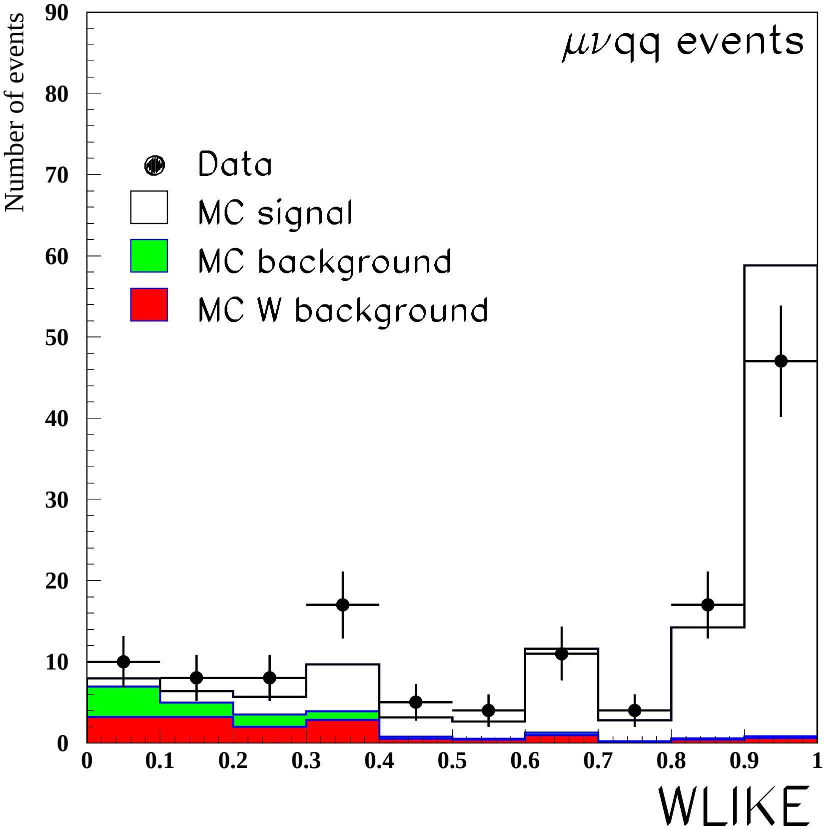

Figure 5.11: WLIKE distribution for the $e^+e^- \rightarrow WW \rightarrow \mu\bar{\nu}q\bar{q}$ semileptonic channel.

Weight w	$=$	0.5	0.3	0.05	1	3	5	10	25	100	1000
ε	$=$	78.3%	77.5%	76.3%	74.7%	70.1%	68.2%	66.6%	58.5%	56.4%	45.7
$N_{\text{back}}^{\text{MC}}$	$=$	23.5	16.6	11.6	8.0	4.1	3.3	2.8	1.6	1.4	0.8
$N_{\text{sig}}^{\text{MC}}$	$=$	99.4	98.4	97.0	94.9	89.1	86.7	84.6	74.3	71.7	58.0
N_{DATA}	$=$	131.0	121.0	113.0	105.0	88.0	83.0	79.0	68.0	64.0	47.0
$\delta\sigma_{\text{stat}}^{\text{exp}}$ (pb)	$=$	0.533	0.522	0.516	0.514	0.522	0.528	0.534	0.568	0.578	0.646
AMUI		cut									
E_{vis}	$\geq$	80.0	80.0	80.0	80.0	80.0	80.0	80.0	80.0	80.0	80.0
N_{ASRC}	$\geq$	18	18	18	18	18	18	18	18	18	20
$\cos(\vartheta)_{\text{miss}}$	$\leq$	.980	.980	.980	.980	.979	.979	.979	.976	.976	.802
E_{miss}	$\geq$	8.0	10.4	10.4	11.7	16.8	18.2	18.2	20.3	20.4	21.2
E_{μ}	$\geq$	10.1	17.7	18.0	18.1	18.2	19.5	21.9	22.4	23.3	25.5
$\alpha \cdot \sin(\vartheta)_{\text{miss}}$	$\geq$	.057	.088	.094	.120	.121	.150	.150	.195	.230	.390
M_{jj}	$\leq$	135.4	125.3	124.9	114.4	114.4	113.1	110.7	104.9	103.6	103.5
M_{jj}	$\geq$	20.0	26.9	32.0	40.5	46.3	47.0	48.8	51.7	53.7	53.7
$M_{\mu\nu}$	$\geq$	20.0	20.2	33.1	45.2	59.6	62.3	63.8	69.4	70.0	70.0
$E_{\text{jet}}^{\text{min}}$	$\geq$	2.7	4.0	6.5	6.9	11.0	11.1	11.1	11.1	12.5	12.5
MIP		cut									
E_{vis}	$\leq$	180.0	180.0	180.0	180.0	180.0	180.0	180.0	180.0	180.0	180.0
E_{vis}	$\geq$	60.0	60.0	60.0	60.0	70.0	70.1	81.5	81.6	115.0	115.1
N_{ASRC}	$\geq$	16	16	16	16	17	17	19	25	25	25
N_{track}	$>$	4	4	4	4	4	8	8	8	8	10
E_{miss}	$\geq$	10.1	10.3	10.5	17.3	23.2	24.4	24.4	24.5	24.6	24.8
$\cos(\vartheta)_{\text{miss}}$	$\leq$	.980	.980	.976	.975	.974	.973	.963	.940	.808	.785
E_{mip}	$\leq$	500.0	500.0	500.0	500.0	448.1	393.8	392.5	150.0	150.0	150.0
E_{mip}	$\geq$	10.4	11.1	19.4	20.5	26.0	27.5	30.0	30.0	30.2	30.3
M_{jj}	$\leq$	142.7	130.1	130.0	130.0	110.0	110.0	110.0	110.0	110.0	110.0
M_{jj}	$\geq$	40.0	40.0	40.0	40.0	63.6	63.6	68.5	68.6	68.8	69.0
$M_{\mu\nu}$	$\geq$	10.0	10.0	10.0	10.0	12.2	14.7	15.0	69.5	69.7	70.0

Table 5.5: Performances of the 10 selections and values of the used cuts; all energies are supposed to be measured in GeV.

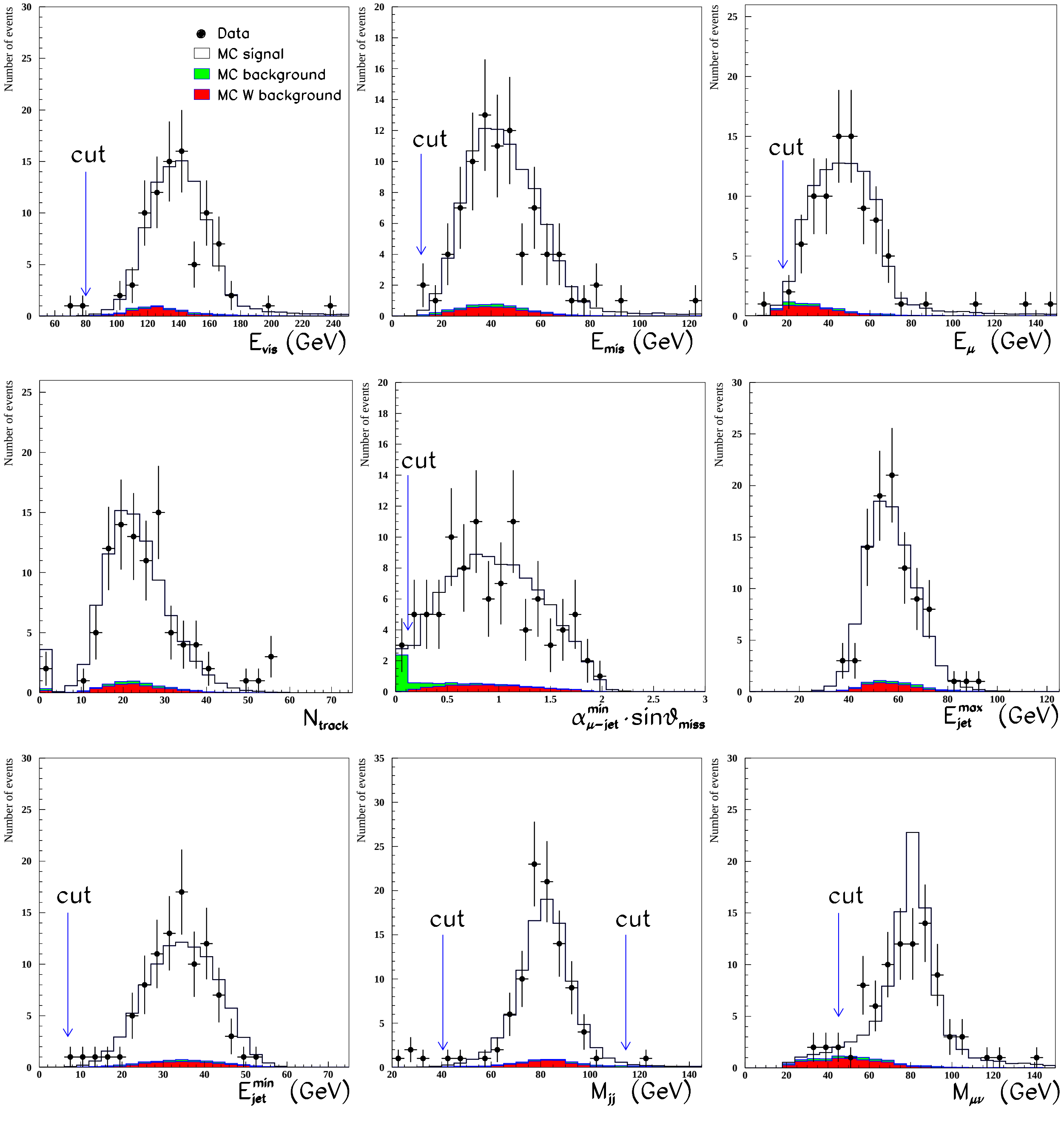

Figure 5.12: Distribution of some variables used in the $\mu\bar{\nu}q\bar{q}$ selection, where the muon is identified as an AMUI.

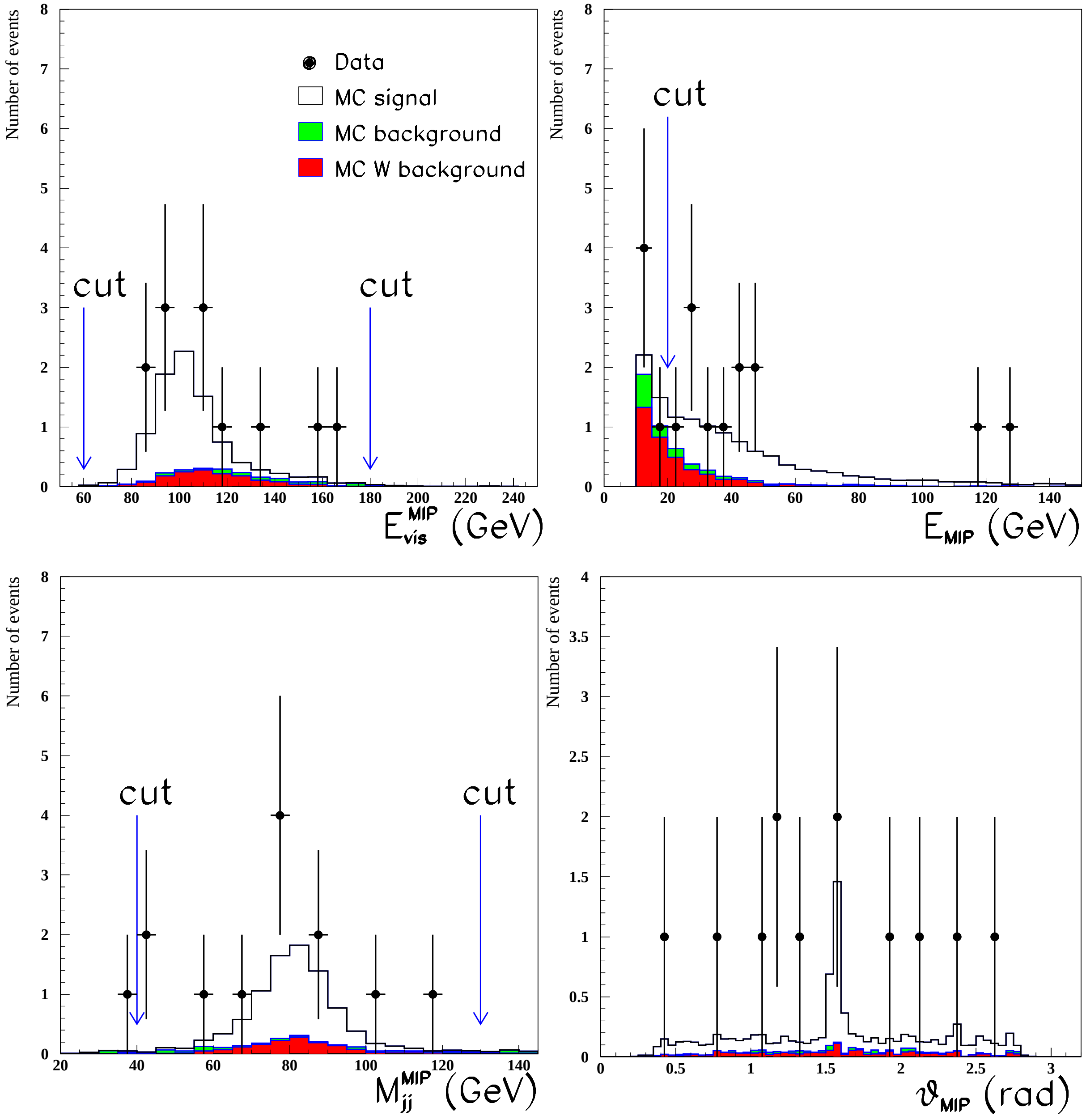

Figure 5.13: Distribution of some variables used in the $\mu\bar{\nu}q\bar{q}$ selection, where the muon is identified as a MIP; the $E_{\rm MIP}$ is plotted after a preselection cut at 10 GeV.

5.5 $\tau\bar{\nu}\mathrm{q}\bar{\mathrm{q}}$ selection

The tau can decay leptonically, in an electron or in a muon, or hadronically; the identification of "hadronic" taus has already been discussed in sec. 3.4.4.

The topology of the $\mathrm{e}^+\mathrm{e}^- \to \mathrm{WW} \to \tau\bar{\nu}\mathrm{q}\bar{\mathrm{q}}$ events depends on the tau decay; if the tau decays leptonically the event is characterized by two jets, a low energy electron or muon and some missing energy due to the undetected neutrinos; if the tau decays hadronically we expect a third jet at low multiplicity (reconstructed as a tau) in the final state. A selected $\tau\bar{\nu}\mathrm{q}\bar{\mathrm{q}}$ event is shown in fig. 5.14 where the jet with 3 tracks is the tau candidate.

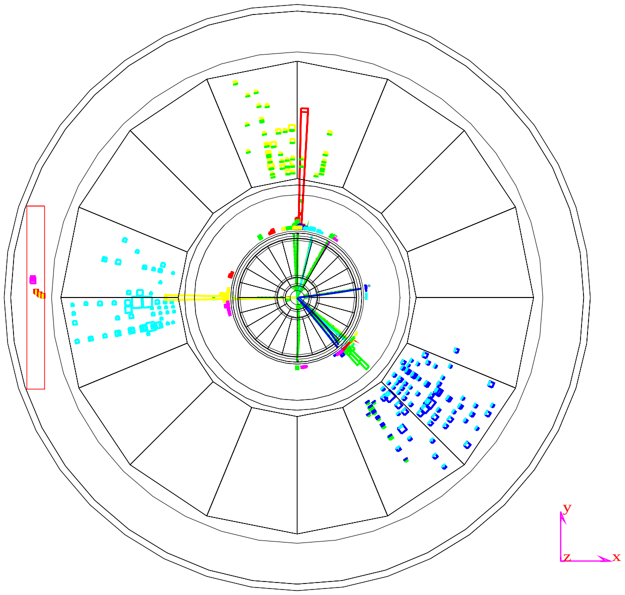

Figure 5.14: Candidate event for the semileptonic selection of $\mathrm{e}^+\mathrm{e}^- \to \mathrm{WW} \to \tau\bar{\nu}\mathrm{q}\bar{\mathrm{q}}$ events.

The selection of $\tau\bar{\nu}\mathrm{q}\bar{\mathrm{q}}$ events varies according to the different tau decays; also the hadronic selection[2] has to be split in three different selections depending on the number of tracks associated to the tau and whether the taus are in the EGAP regions. The reason is that the events where the tau has two associated tracks or points towards the EGAPs introduce a very high background and therefore have to be treated separately.

The final selection is the logic OR of the following 5 selections:

1. events where $\tau \to \mathrm{e}\bar{\nu}_e\nu_\tau$;
2. events where $\tau \to \mu\bar{\nu}_\mu\nu_\tau$;
3. events where $\tau \to$ had, taus with 1 or 3 tracks reconstructed in any part of the detector but the EGAPs;

---

[2] The selection where the tau decays in hadrons.

4. events where $\tau \rightarrow$ had, taus with 2 tracks reconstructed in any part of the detector but the EGAPs;

5. events where $\tau \rightarrow$ had, pointing towards the EGAP regions.

I have studied these five selections separately and for each of them I have determined, using the optimization program, the most useful variables; then I have performed a global optimization and I have obtained the results reported in tab. 5.6, 5.7. About 90% of the total expected background is equally shared between $\mathrm{q\bar{q}}(\gamma)$ and $\mathrm{e^+e^-} \rightarrow \mathrm{WW} \rightarrow \mathrm{e\bar{\nu}q\bar{q}}$, $\mu\bar{\nu}\mathrm{q\bar{q}}$ processes, the remaining 10% is due to ZZ and Zee processes.

In tab. 5.6, 5.7 $M_{\tau\nu}$ represents the invariant mass tau-neutrino, M_{jj} is the invariant mass of the two reconstructed jet, once the identified lepton has been subtracted from the event, while M_{jj}^{glob} is the invariant mass of the two jets which have been reconstructed from all the objects in the event; $\mathrm{p}_{\mathrm{miss}}^{\|}$ is the longitudinal missing momentum $E_{\mathrm{mis}} \cdot \cos(\vartheta)_{\mathrm{miss}}$, $\alpha_{\tau-\mathrm{jet}}$ is the angle between the tau and the nearest jet, $E_{\mathrm{cone}}^{15^\circ}$ is the calorimetric energy contained in a 15° half-cone around the tau direction, $N_{\mathrm{clust}}^{20^\circ}$ is the number of calorimetric clusters in a 20° half-cone around the tau direction.

Fig. 5.16 and 5.17 show some distributions of the used variables for the selection optimized with a background weight factor w=1. Fig. 5.16(a) compares the number of selected and expected events in the five different selections, fig. 5.16(b) shows the distribution of the tau polar angle. The most powerful cuts are the ones on the invariant electron-neutrino and muon neutrino masses (fig. 5.17(c,e)) and the cuts on $\cos(\vartheta)_{\mathrm{miss}}$, M_{jj}, acollinearity and $E_{\mathrm{cone}}^{15^\circ}$ for the hadronic selection (fig. 5.17(f,g,h,i)).

The 4 selections showed in tab. 5.6 have been used to construct the WLIKE variable shown in fig. 5.15.

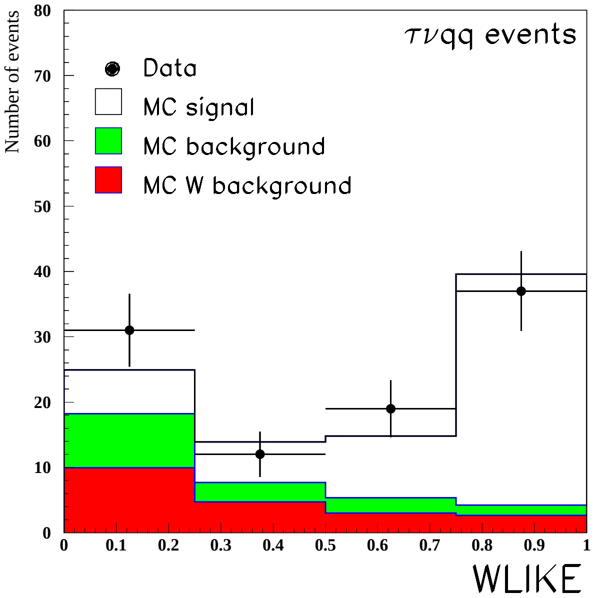

Figure 5.15: WLIKE distribution for the $\mathrm{e^+e^-} \rightarrow \mathrm{WW} \rightarrow \tau\bar{\nu}\mathrm{q\bar{q}}$ semileptonic channel.

Weight w	$=$	0.5	1	3	10
ε	$=$	45.5%	40.1%	35.5%	28.2%
$N_{\mathrm{back}}^{\mathrm{MC}}$	$=$	35.5	17.2	9.6	4.3
$N_{\mathrm{sig}}^{\mathrm{MC}}$	$=$	57.6	50.8	44.9	35.7
N_{DATA}	$=$	99	68	56	37
$\delta\sigma_{\mathrm{stat}}^{\mathrm{exp}}$ (pb)	$=$	0.804	0.786	0.803	0.873
general cuts		cut			
E_{vis}	$\leq$	156.7	154.9	154.5	154.5
E_{vis}	$\geq$	71.6	80.0	80.0	80.0
E_{mis}	$\geq$	6.0	6.0	6.0	6.0
N_{track}	$\geq$	1	10	10	10
$E_{\mathrm{jet}}^{\mathrm{max}}$	$\leq$	99.1	82.7	82.6	79.0
$E_{\mathrm{jet}}^{\mathrm{min}}$	$\geq$	10.6	13.8	13.8	17.1
$M_{\tau\nu}$	$\geq$	2.0	2.0	2.0	2.0
$\tau \to \mathrm{e}$		cut			
$E_{\mathrm{vis}} + E_{\mathrm{mis}}$	$\leq$	206.4	206.4	179.0	176.5
N_{asrc}	$>$	12	12	12	12
$\cos(\vartheta)_{\mathrm{miss}}$	$\leq$	0.957	0.957	0.934	0.887
$\mathrm{p}_{\mathrm{miss}}^{\perp}$	$\geq$	10.0	10.0	10.0	11.0
E_{el}	$\leq$	51.2	45.2	42.0	42.0
E_{el}	$\geq$	5.0	5.0	5.0	5.0
M_{jj}	$\leq$	104.0	104.0	104.0	98.1
M_{jj}	$\geq$	56.9	58.0	59.0	60.0
$M_{\mathrm{e}\nu}$	$\leq$	68.6	64.8	63.5	59.0
$E_{\mathrm{jet}}^{\mathrm{min}}$	$\leq$	56.4	56.3	55.0	55.0
acollinearity	$\geq$	0.76	0.76	1.30	1.30
$\tau \to \mu$		cut			
$E_{\mathrm{vis}} + E_{\mathrm{mis}}$	$\leq$	213.8	201.5	179.0	179.0
$E_{\mathrm{mis}} + M_{jj}^{\mathrm{glob}}$	$\geq$	94.0	95.0	97.0	97.0
N_{asrc}	$>$	11	11	11	11
$\cos(\vartheta)_{\mathrm{miss}}$	$\leq$	0.980	0.980	0.980	0.980
$\mathrm{p}_{\mathrm{miss}}^{\parallel}$	$\leq$	61.7	46.3	42.5	42.5
E_{μ}	$\leq$	44.0	44.0	44.0	40.1
E_{μ}	$\geq$	5.0	5.0	5.0	5.0
M_{jj}	$\leq$	105.0	105.0	102.5	97.2
M_{jj}	$\geq$	49.4	53.8	54.0	60.8
$M_{\mu\nu}$	$\leq$	65.0	64.8	61.5	57.0
acollinearity	$\geq$	1.27	1.39	1.50	1.50
$\cos(\vartheta)_{\mu}$	$\leq$	0.911	0.871	0.811	0.811

Table 5.6: Performances of the 4 selections and values of the used cuts; all energies are supposed to be measured in GeV.

$\tau \rightarrow$ had		cut			
$E_{\text{vis}} - E_{\text{mis}}$	$\leq$	134.0	134.0	132.0	132.0
$E_{\text{mis}} + M_{jj}^{\text{glob}}$	$\geq$	106.6	107.1	107.4	112.3
N_{asrc}	$>$	17	17	18	24
$\cos(\vartheta)_{\text{miss}}$	$\leq$	0.963	0.951	0.944	0.944
$\text{p}_{\text{miss}}^{\perp}$	$\geq$	3.5	6.0	6.5	7.0
E_{τ}	$\geq$	5.0	5.0	6.1	8.2
$M_{\tau\nu}$	$\leq$	130.8	96.0	91.4	90.8
1,3 prongs – no egap		cut			
M_{jj}	$\leq$	104.3	101.7	97.0	97.0
M_{jj}	$\geq$	40.0	51.0	53.8	58.0
acollinearity	$\geq$	1.50	1.81	1.87	1.96
$\alpha_{\tau-\text{jet}}$	$\geq$	0.359	0.410	0.453	0.586
$E_{\text{cone}}^{15^\circ}$	$\geq$	2.2	3.4	4.4	5.6
$N_{\text{clust}}^{20^\circ}$	$<$	6	6	5	5
2 prongs – no egap		cut			
M_{jj}	$\leq$	97.5	96.4	91.1	90.1
M_{jj}	$\geq$	48.0	48.0	66.0	66.0
acollinearity	$\geq$	1.75	2.00	2.00	2.14
τ in egap		cut			
M_{jj}	$\leq$	103.5	99.8	91.7	91.0
M_{jj}	$\geq$	50.0	50.9	51.2	66.2
acollinearity	$\geq$	1.60	2.00	2.00	2.00

Table 5.7: Continuation of the previous table.

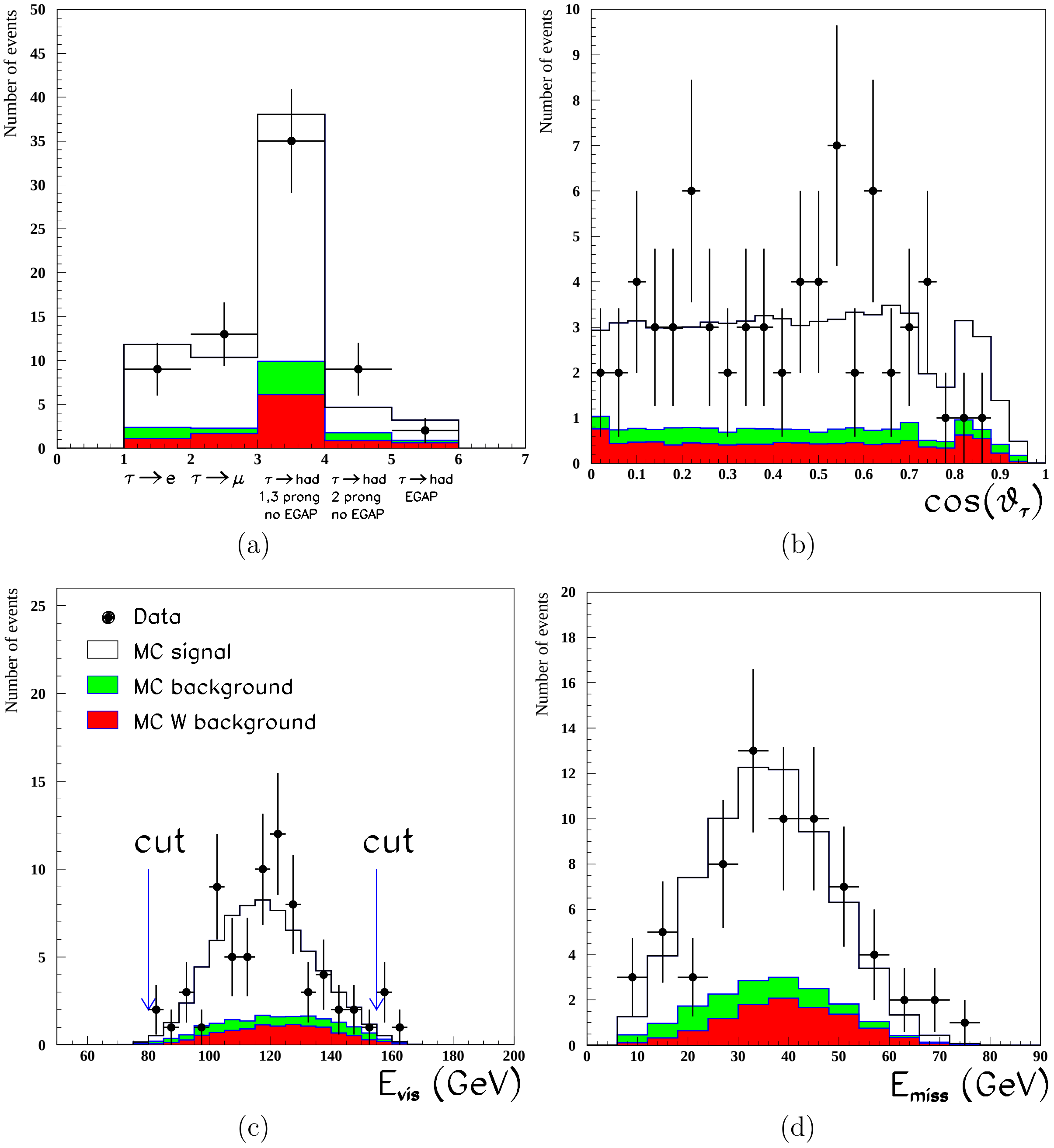

(a) (b)

(c) (d)

Figure 5.16: (a) Selected events for the different five τ selections; (b) cosine of the tau polar angle for all the selected taus events; (c,d) visible and missing energy for the total sample of selected taus.

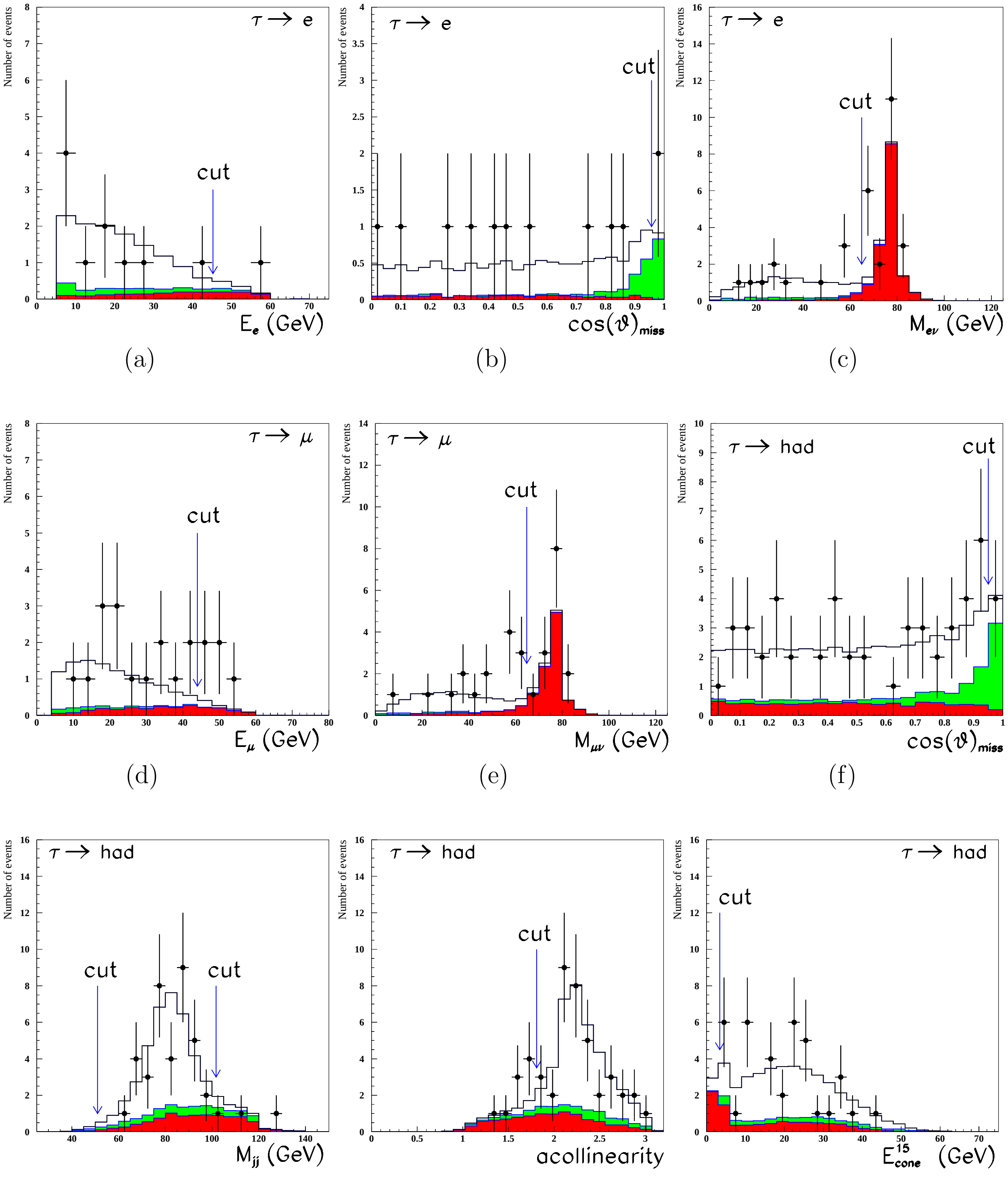

(a) (b) (c)

(d) (e) (f)

(g) (h) (i)

Figure 5.17: “n-1” histograms of some variables used in the analysis.

5.6 Selection of fully leptonic W decays

The selection of events where both the W bosons decay leptonically exploits the large missing energy due to the two high energy neutrinos escaping detection and the very low track multiplicity.

Fig. 5.18 shows a $e^+e^- \rightarrow e^-\bar{\nu}_e e^+\nu_e$ candidate event.

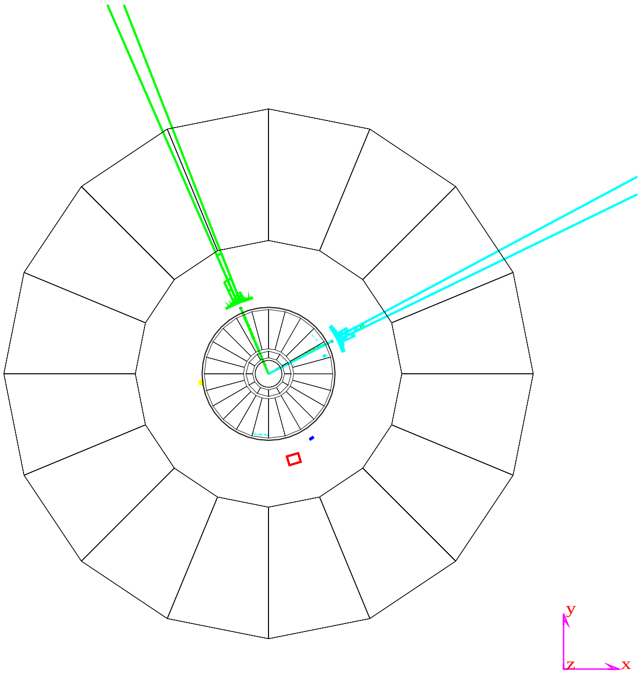

Figure 5.18: $e^-\bar{\nu}_e e^+\nu_e$ candidate event for the semileptonic selection of $e^+e^- \rightarrow WW \rightarrow \ell^-\bar{\nu}\ell^+\nu$ events.

A very simple preselection requiring at most six tracks in the event rejects almost all the hadronic and semileptonic W decays and the $e^+e^- \rightarrow q\bar{q}(\gamma)$ events while keeping all the low multiplicity events including a large background from $e^+e^- \rightarrow \ell^+\ell^-(\gamma)$. This background consists mainly of events with high energy radiative photons that fake a large missing energy if not detected. A large fraction of these events can be rejected by requiring that the energy in the forward detectors (luminosity monitors and ALR) is smaller than 10 GeV. In order to reject the background from cosmic muons, the time of flight of each muon in the event must be within ±3ns of the beam crossing and the distance of closest approach of the muon track to the interaction point must be less than 200 mm.

The event selection then proceeds in two steps; first the leptons in the event are counted, identified and all their kinematical variables are calculated; then a different selection is applied depending on the number of leptons present in the event and on their flavour; only the events with one or two identified leptons are selected.

The events with two identified leptons are divided into six categories, namely ee, eμ, eτ, $\mu\mu$, $\mu\tau$, $\tau\tau$. For each of these categories a different selection is applied which is based essentially on the same set of variables, described in detail in the next section. The events with only one identified lepton are accepted only if the lepton is an electron or a muon and if there is another unidentified particle which is neither a photon nor a minimum ionizing particle; these events are grouped into two categories: eX and μX.

5.6.1 Selection variables and cuts

The variables used in the selection are listed below.

- The visible energy E_{vis}; this variable is used to reject events with low missing energy.
- The residual energy E_{res} in the event after the energy of the two leptons has been subtracted from the total visible energy. Events with radiative photons have a large residual energy; thus this variable can be used very efficiently to reject radiative $e^+e^- \to \ell^+\ell^-(\gamma)$ events.
- The energy E_ℓ^{max} of the most energetic lepton; cutting on this variable, most of the events with low energy leptons like two–photon events are rejected.
- The angle $\alpha_{\ell\ell}$ between the two leptons. This angle is randomly distributed for W events as the two Ws are almost at rest; on the contrary background events tends to be almost back–to–back. The same holds for the next variable.
- The angle $\varphi_{\ell\ell}$ between the two leptons on the transverse plane.
- The polar angle ϑ_{miss} of the missing momentum vector. In radiative background events, the missing momentum is the momentum of the photon which has escaped the detector: its distribution is peaked at low polar angles.
- The transverse momentum $p_{thr}^\perp$ of the two leptons with respect to the thrust built with the lepton momenta projected on the transverse plane. As the leptons produced by the two Ws are generally highly acoplanar and acollinear, their $p_{thr}^\perp$ is large with respect to other background events which are essentially coplanar.
- The number of tracks N_{track} in the event. In most of the event categories mentioned above there are only two charged tracks so that a cut on this number can reduce background events with higher multiplicity.
- The transverse missing momentum $p_{miss}^\perp$.

For the events with one lepton only, the variables are computed using the lepton and the jet associated to the unidentified particle.

The variables used for the different selections are summarized in tab. 5.8.

Tab. 5.9, 5.10 reports the values of the cuts used for the 7 selections which have been found by varying the background weight factor w from 0.5 to 10 in the optimization program; in such a table the results for each selection are also shown. The background

	E_{vis}	E_{res}	E_ℓ^{max}	$\alpha_{\ell\ell}$	$\varphi_{\ell\ell}$	ϑ_{miss}	$p_{thr}^\perp$	N_{track}	$p_{miss}^\perp$
ee	$\surd$	$\surd$	$\surd$			$\surd$	$\surd$		
eμ		$\surd$	$\surd$			$\surd$	$\surd$	$\surd$	
eτ	$\surd$	$\surd$	$\surd$	$\surd$		$\surd$	$\surd$		
$\mu\mu$	$\surd$	$\surd$	$\surd$			$\surd$	$\surd$		
$\mu\tau$		$\surd$	$\surd$	$\surd$		$\surd$	$\surd$		
$\tau\tau$		$\surd$	$\surd$	$\surd$			$\surd$		
eX			$\surd$		$\surd$			$\surd$	$\surd$
μX			$\surd$		$\surd$	$\surd$			$\surd$

Table 5.8: Variables used for the event selections in the various categories; the symbol $\surd$ indicates that the variables is used in the selection.

comes almost equally from $e^+e^- \to \mu^+\mu^-$, $\tau^+\tau^-$, $e^+e^-\mu^+\mu^-$, $e^+e^-\tau^+\tau^-$ and Zee and ZZ processes.

Fig. 5.20 shows the distribution of 4 variables for events selected in the selection with $w = 1$.

The 7 selections used to construct the WLIKE variable are shown in fig. 5.19.

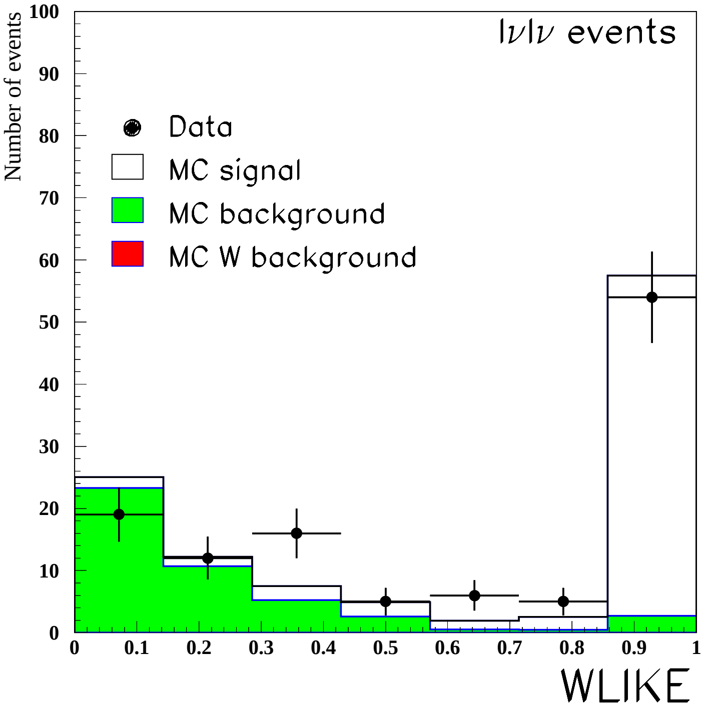

Figure 5.19: WLIKE distribution for the $e^+e^- \to WW \to \ell^-\bar{\nu}\ell^+\nu$ leptonic channel.

Weight w	$=$	0.5	0.1	0.3	1	3	5	10
$\varepsilon^{\text{KORALW}}$	$=$	63.2%	61.8%	60.4%	58.5%	55.9%	54.2%	52.4%
$\varepsilon^{\text{EXCALIBUR}}$	$=$	45.4%	44.1%	42.9%	41.4%	40.0%	38.9%	37.5%
$N_{\text{back}}^{\text{MC}}$	$=$	45.6	22.4	11.6	6.4	3.8	3.2	2.8
$N_{\text{sig}}^{\text{MC KORALW}}$	$=$	57.5	56.2	55.0	53.2	50.8	49.3	47.7
$N_{\text{sig}}^{\text{MC EXCALIBUR}}$	$=$	66.0	64.3	62.8	60.5	58.3	56.8	54.8
N_{DATA}	$=$	116	98	86	70	66	59	54
$\delta\sigma_{\text{stat}}^{\text{exp}}$ (pb)	$=$	0.608	0.547	0.517	0.508	0.510	0.516	0.524
ee		cut						
$E_{\text{vis}}/E_{\text{CM}}$	$\geq$	0.126	0.127	0.127	0.127	0.127	0.127	0.128
$E_{\text{vis}}/E_{\text{CM}}$	$\leq$	0.802	0 .802	0.802	0.802	0.802	0.802	0.757
E_{ℓ}^{max}	$\geq$	20.3	24.4	25.3	25.3	25.3	25.3	26.6
E_{ℓ}^{max}	$\leq$	75.0	75.0	73.7	73.7	70.8	70.8	70.7
$\cos(\vartheta)_{\text{miss}}$	$\leq$	0.999	0.991	0.961	0.954	0.950	0.950	0.950
$\text{p}_{\text{thr}}^{\perp}$	$\geq$	1.50	1.71	1.95	1.95	2.75	2.75	2.75
E_{res}	$\leq$	12.6	11.4	11.4	11.4	15.9	8.9	8.8
eμ		cut						
E_{ℓ}^{max}	$\geq$	22.3	22.3	22.3	22.3	22.3	25.7	29.3
$\cos(\vartheta)_{\text{miss}}$	$\leq$	1.0000	0.984	0.984	0.984	0.984	0.982	0.959
N_{track}	$\leq$	2	2	2	2	2	2	2
$\text{p}_{\text{thr}}^{\perp}$	$\geq$	1.00	1.30	1.30	1.44	2.52	2.72	2.73
E_{res}	$\leq$	20.0	20.0	20.0	20.0	16.9	16.9	15.5
eτ		cut						
$E_{\text{vis}}/E_{\text{CM}}$	$\leq$	0.797	0.766	0.766	0.700	0.700	0.700	0.700
E_{ℓ}^{max}	$\leq$	90.0	90.0	90.0	90.0	90.0	90.0	90.0
E_{ℓ}^{max}	$\geq$	10.4	18.3	18.3	18.3	18.3	18.3	18.3
$\alpha_{\ell\ell}$	$\geq$	0.10	0.12	0.12	0.21	0.21	0.21	0.21
$\alpha_{\ell\ell}$	$\leq$	3.06	3.04	3.01	3.01	3.01	3.01	3.01
$\cos(\vartheta)_{\text{miss}}$	$\leq$	0.994	0.994	0.990	0.979	0.966	0.966	0.966
$\text{p}_{\text{thr}}^{\perp}$	$\geq$	2.08	2.30	2.38	4.44	4.44	4.93	4.93
E_{res}	$\leq$	19.0	19.0	18.0	18.0	6.0	6.0	6.0

Table 5.9: Performances of the 7 selections and values of the used cuts; all energies are supposed to be measured in GeV (continue on next page).

$\mu\mu$		cut						
$E_{\mathrm{vis}}/E_{\mathrm{CM}}$	$\leq$	0.900	0.890	0.890	0.802	0.786	0.785	0.785
E_ℓ^{max}	$\geq$	23.0	23.0	23.0	23.5	23.5	23.5	23.5
$\cos(\vartheta)_{\mathrm{miss}}$	$\leq$	0.963	0.963	0.956	0.955	0.948	0.918	0.908
$\mathrm{p}_{\mathrm{thr}}^{\perp}$	$\geq$	2.25	2.25	2.88	2.88	2.88	3.13	3.15
E_{res}	$\leq$	19.3	16.3	16.3	16.3	16.3	12.9	10.3

$\mu\tau$		cut						
E_ℓ^{max}	$\leq$	90.0	90.0	81.3	77.0	77.0	76.0	76.0
E_ℓ^{max}	$\geq$	13.1	13.1	13.1	13.1	13.2	19.5	19.5
$\alpha_{\ell\ell}$	$\geq$	0.10	0.10	0.10	0.10	0.10	0.16	0.16
$\alpha_{\ell\ell}$	$\leq$	3.00	3.00	3.00	3.00	3.00	3.00	3.00
$\cos(\vartheta)_{\mathrm{miss}}$	$\leq$	0.994	0.994	0.994	0.993	0.993	0.993	0.964
$\mathrm{p}_{\mathrm{thr}}^{\perp}$	$\geq$	2.00	2.28	3.50	4.01	4.02	4.32	4.85
E_{res}	$\leq$	20.0	18.5	15.9	15.9	13.0	11.0	10.8

$\tau\tau$		cut						
E_ℓ^{max}	$\leq$	89.9	89.9	89.9	89.8	81.8	81.8	71.3
E_ℓ^{max}	$\geq$	10.3	11.0	11.0	11.0	11.8	12.2	14.4
$\alpha_{\ell\ell}$	$\geq$	0.32	0.32	0.35	0.35	0.35	0.35	0.35
$\alpha_{\ell\ell}$	$\leq$	3.00	3.00	3.00	3.00	3.00	3.00	3.00
$\mathrm{p}_{\mathrm{thr}}^{\perp}$	$\geq$	3.95	4.48	4.48	4.48	4.75	4.75	5.00
E_{res}	$\leq$	18.1	17.8	17.8	14.4	11.8	11.8	6.9

eX		cut						
N_{track}	$\geq$	2	2	2	2	2	2	2
E_ℓ^{max}	$\leq$	81.9	75.6	75.6	75.6	70.0	69.4	65.1
$\varphi_{\ell\ell}$	$\leq$	3.11	3.08	3.08	3.07	3.00	2.98	2.90
$\mathrm{p}_{\mathrm{miss}}^{\perp}$	$\geq$	28.0	28.0	28.0	30.5	36.0	36.0	37.5

μX		cut						
E_ℓ^{max}	$\leq$	75.6	71.3	71.3	68.0	68.0	68.0	68.0
E_ℓ^{max}	$\geq$	27.0	28.0	28.0	28.0	28.0	29.5	29.5
$\varphi_{\ell\ell}$	$\leq$	3.09	2.95	2.91	2.91	2.91	2.91	2.91
$\cos(\vartheta)_{\mathrm{miss}}$	$\leq$	0.950	0.950	0.950	0.950	0.950	0.950	0.950
$\mathrm{p}_{\mathrm{miss}}^{\perp}$	$\geq$	30.00	31.00	31.5	33.2	34.5	37.0	40.0

Table 5.10: Continuation of previous table.

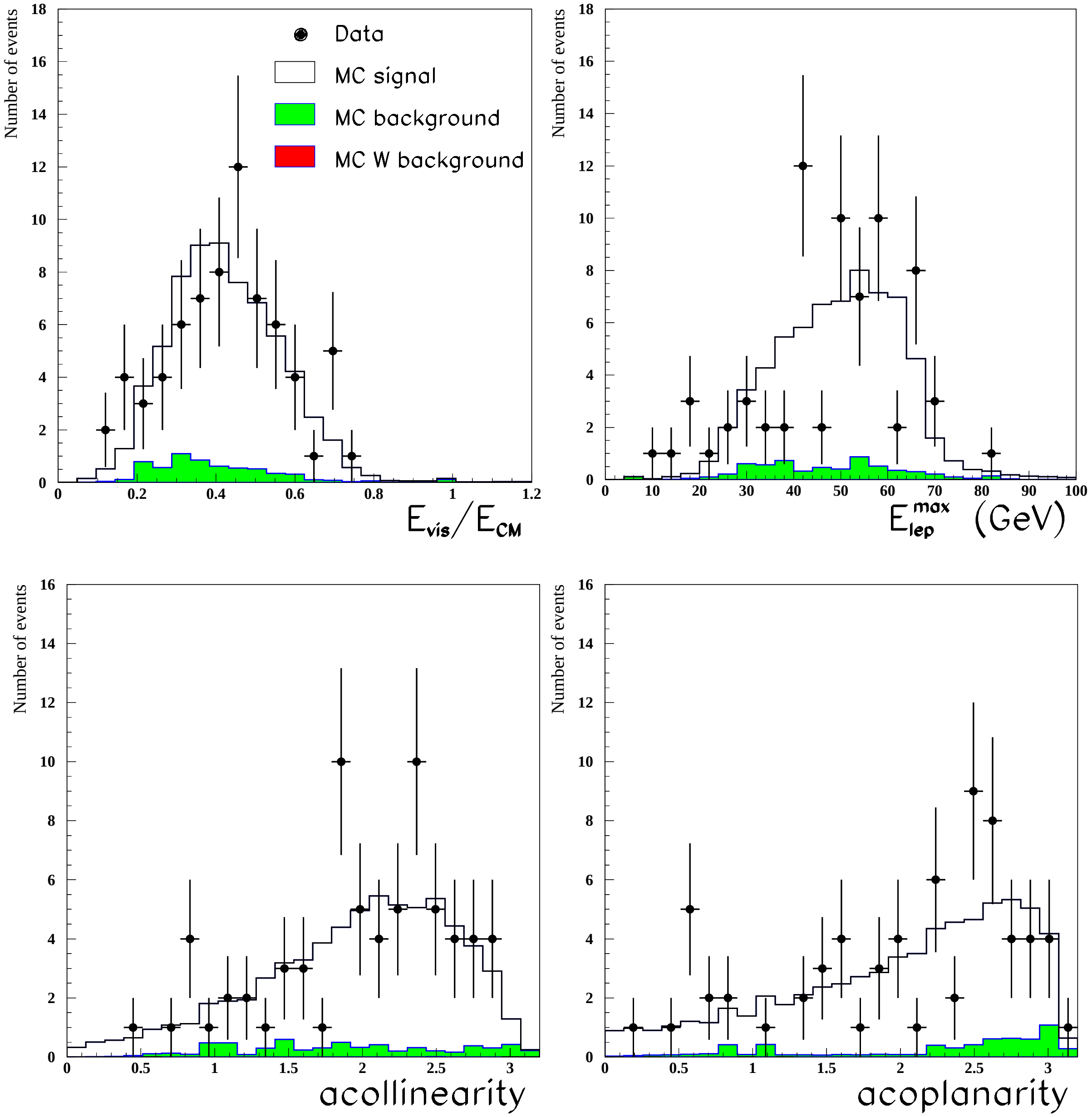

Figure 5.20: Distribution of some variables for selected $\ell^-\bar{\nu}\ell^+\nu$ events.

5.7 Results

Using the WLIKE distributions for the five W pair final states shown in fig. 5.6, 5.8, 5.11, 5.15, 5.19 it is possible to extract the partial cross sections of W pair production in each final state and the total W pair cross section as anticipated in sec. 4.3.

Eq. 4.1 needs to be slightly modified to take into account the presence of all the 4f diagrams in the signal of the WLIKE distributions relative to the $\mathrm{e}\bar{\nu}\mathrm{q}\bar{\mathrm{q}}$ and $\ell^-\bar{\nu}\ell^+\nu$ signals, since for these two channels the signal has been estimated with EXCALIBUR.

The minimization of the likelihood function ℓ (eq. 4.1) gives a measurement of the 4f cross section for the $\mathrm{e}\bar{\nu}\mathrm{q}\bar{\mathrm{q}}$ and $\ell^-\bar{\nu}\ell^+\nu$ channels. Since we want to measure the CC03 cross section, as it has been discussed in sec. 2.1.6, we have to introduce the correction factor described in eq. 2.7 in the likelihood function ℓ in the following way:

$$\begin{aligned} \ell &= -2 \cdot \sum_{i=1}^{5} \sum_{k=1}^{N_i^{\mathrm{bins}}} \ln \frac{e^{-\lambda_{ik}} \, \lambda_{ik}^{N_{ik}^{\mathrm{data}}}}{N_{ik}^{\mathrm{data}}!} \\ \lambda_{ik} &= \sum_{j=1}^{5} \varepsilon_{ijk} \, \sigma_j \, \mathcal{L} \, f_j + N_{ik}^{\mathrm{bkg(no\_W)}} \end{aligned}$$

where the indexes i and j run over the 5 selections and the index k runs over the bins of the WLIKE distribution for each selection, and $f_j = 1$ for the $\mathrm{q}\bar{\mathrm{q}}\mathrm{q}\bar{\mathrm{q}}$, $\mu\bar{\nu}\mathrm{q}\bar{\mathrm{q}}$ and $\tau\bar{\nu}\mathrm{q}\bar{\mathrm{q}}$ selections while

$$f_j = \frac{\sigma_j^{\mathrm{EXCALIBUR}}}{\sigma_j^{\mathrm{KORALW}}}$$

for the $\mathrm{e}\bar{\nu}\mathrm{q}\bar{\mathrm{q}}$ and $\ell^-\bar{\nu}\ell^+\nu$ channels. All the other symbols have the same meaning as in sec. 4.3.

Since the main background source to all the selections comes from the $\mathrm{e}^+\mathrm{e}^- \to \mathrm{q}\bar{\mathrm{q}}(\gamma)$ process, it is interesting to measure its cross section by performing a fit with 6 free parameters: the five W cross sections and $\sigma_{\mathrm{q}\bar{\mathrm{q}}\gamma}$. In such a case:

$$\lambda_{ik} = \sum_{j=1}^{5} \varepsilon_{ijk} \, \sigma_j \, \mathcal{L} \, f_j + \varepsilon_{ik} \, \sigma_{\mathrm{q}\bar{\mathrm{q}}\gamma} \, \mathcal{L} + N_{ik}^{\mathrm{bkg(no\_W,no\_q\bar{q}\gamma)}}$$

The results of the fit with five and six free parameters are shown in tab. 5.11 and are compared to the Standard Model expectations.

From the WLIKE distributions we can also extract the total W pair production cross section σ_{WW} by minimizing the likelihood ℓ with:

$$\lambda_{ik} = \sum_{j=1}^{5} \varepsilon_{ijk} \cdot \mathrm{DF}_j \cdot \sigma_{\mathrm{WW}} \cdot \mathcal{L} \cdot f_j + N_{ik}^{\mathrm{bkg(no\_W)}}$$

where the expression of the Decay Fractions DF have been defined in sec. 2.1.4, and can be expressed as a function of the W partial decay widths in the following way:

$$\mathrm{DF}_{\mathrm{WW}\to\mathrm{qqqq}} = \left(\frac{\Gamma_{\mathrm{W}\to\mathrm{had}}}{\Gamma_{\mathrm{W}}^{\mathrm{tot}}} \right)^2$$

	5 parameter fit	6 parameter fit	Standard Model
$\sigma^{\mathrm{CC03}}_{\mathrm{q\bar{q}q\bar{q}}}$ (pb)	$7.87^{+0.45}_{-0.43}$	$7.79^{+0.48}_{-0.46}$	7.17
$\sigma^{\mathrm{CC03}}_{\mathrm{e}\bar{\nu}\mathrm{q\bar{q}}}$ (pb)	$2.33^{+0.26}_{-0.24}$	$2.33^{+0.26}_{-0.24}$	2.30
$\sigma^{\mathrm{CC03}}_{\mu\bar{\nu}\mathrm{q\bar{q}}}$ (pb)	$2.28^{+0.26}_{-0.24}$	$2.28^{+0.26}_{-0.24}$	2.30
$\sigma^{\mathrm{CC03}}_{\tau\bar{\nu}\mathrm{q\bar{q}}}$ (pb)	$2.56^{+0.38}_{-0.35}$	$2.54^{+0.38}_{-0.36}$	2.30
$\sigma^{\mathrm{CC03}}_{\ell^-\bar{\nu}\ell^+\nu}$ (pb)	$1.75^{+0.24}_{-0.22}$	$1.75^{+0.24}_{-0.22}$	1.67
$\sigma_{\mathrm{q\bar{q}}\gamma}$ (pb)	–	$111.2^{+8.8}_{-8.5}$	107.5

Table 5.11: Measured CC03 and $\mathrm{q\bar{q}}(\gamma)$ cross sections obtained with a five and six free parameters fit; only statistical errors are reported.

$$\begin{aligned}
\mathrm{DF}_{\mathrm{WW}\to\mathrm{e}\nu\mathrm{qq}} &= 2\cdot\frac{\Gamma_{\mathrm{W}\to\mathrm{had}}}{\Gamma^{\mathrm{tot}}_{\mathrm{W}}}\cdot\frac{\Gamma_{\mathrm{W}\to\mathrm{e}\nu}}{\Gamma^{\mathrm{tot}}_{\mathrm{W}}}\\
\mathrm{DF}_{\mathrm{WW}\to\mu\nu\mathrm{qq}} &= 2\cdot\frac{\Gamma_{\mathrm{W}\to\mathrm{had}}}{\Gamma^{\mathrm{tot}}_{\mathrm{W}}}\cdot\frac{\Gamma_{\mathrm{W}\to\mu\nu}}{\Gamma^{\mathrm{tot}}_{\mathrm{W}}}\\
\mathrm{DF}_{\mathrm{WW}\to\tau\nu\mathrm{qq}} &= 2\cdot\frac{\Gamma_{\mathrm{W}\to\mathrm{had}}}{\Gamma^{\mathrm{tot}}_{\mathrm{W}}}\cdot\frac{\Gamma_{\mathrm{W}\to\tau\nu}}{\Gamma^{\mathrm{tot}}_{\mathrm{W}}}\\
\mathrm{DF}_{\mathrm{WW}\to\ell\nu\ell\nu} &= \left(\frac{\Gamma_{\mathrm{W}\to\mathrm{e}\nu}+\Gamma_{\mathrm{W}\to\mu\nu}+\Gamma_{\mathrm{W}\to\tau\nu}}{\Gamma^{\mathrm{tot}}_{\mathrm{W}}}\right)^2
\end{aligned}$$

Fixing all the W decay widths to the values predicted by the Standard Model (tab. 2.2) we are left with only σ_{WW} as free parameter, and we have:

$$\boxed{\sigma_{\mathrm{WW}} = 16.76^{+0.66}_{-0.64}\ \mathrm{pb}}$$

where only statistical errors is reported (the discussion of systematic errors follows in the next chapter).

In Fig. 5.21 and 5.22 the measured total and partial W pair production cross sections are compared to the theoretical predictions made with and without the contribution of the three boson vertices (ZWW and γWW) diagrams (see sec. 2.1). The measured points show a good agreement with the Standard Model predictions, thus constituting a direct evidence of bosonic self-interactions, characteristic signatures of the Standard Model non-abelian nature.

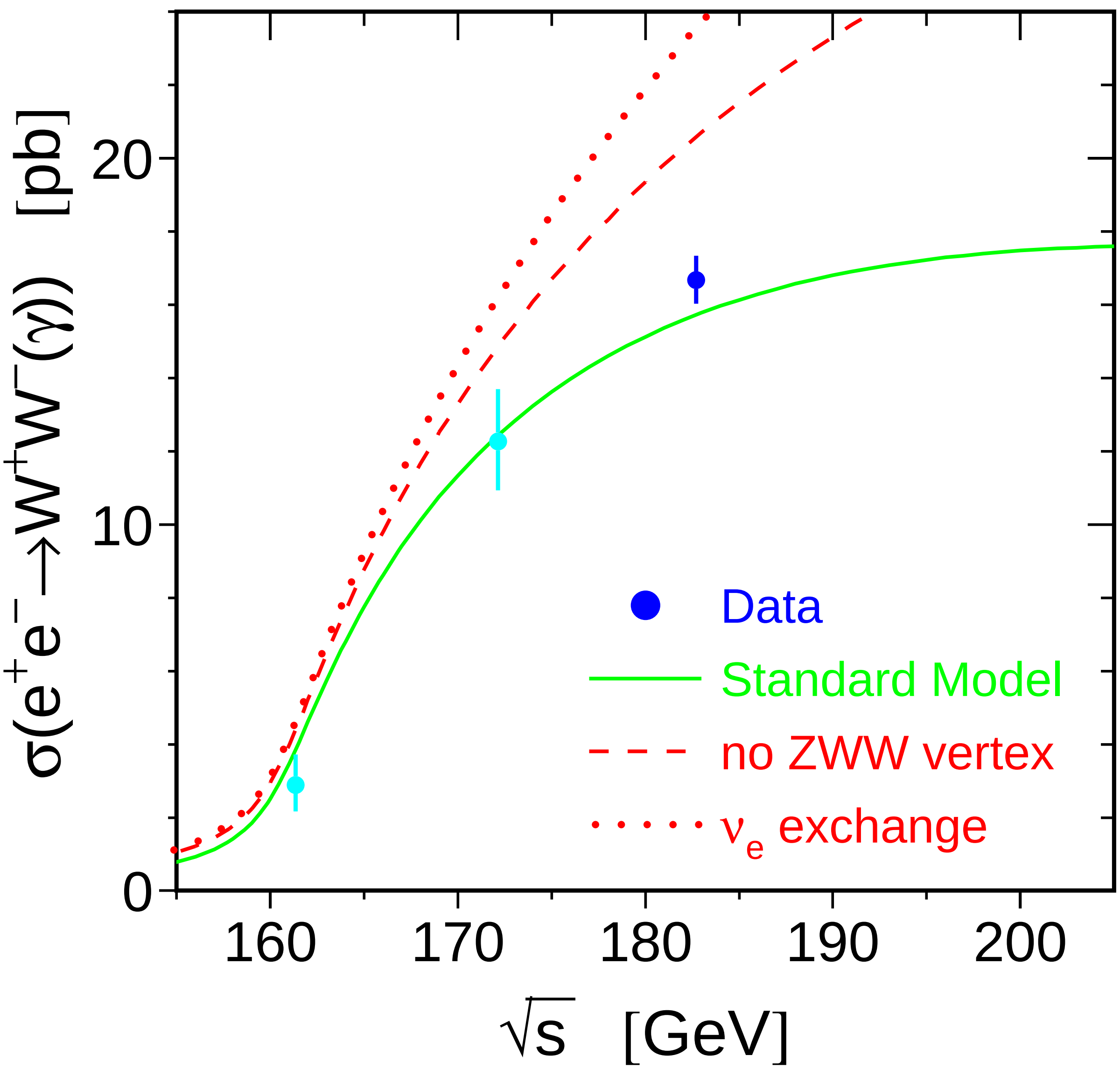

Figure 5.21: W pair production cross section as a function of $\sqrt{s}$; the solid curve shows the Standard Model expectation, the dashed curve shows the expectation if there is no ZWW coupling, the dotted curve shows the expectation if only the t-channel ν_e exchange in W pair production is considered; the error bar represents the statistical errors only. The points at $\sqrt{s}$ = 161 GeV and $\sqrt{s}$ = 172 GeV are the L3 published measurements [67], [68].

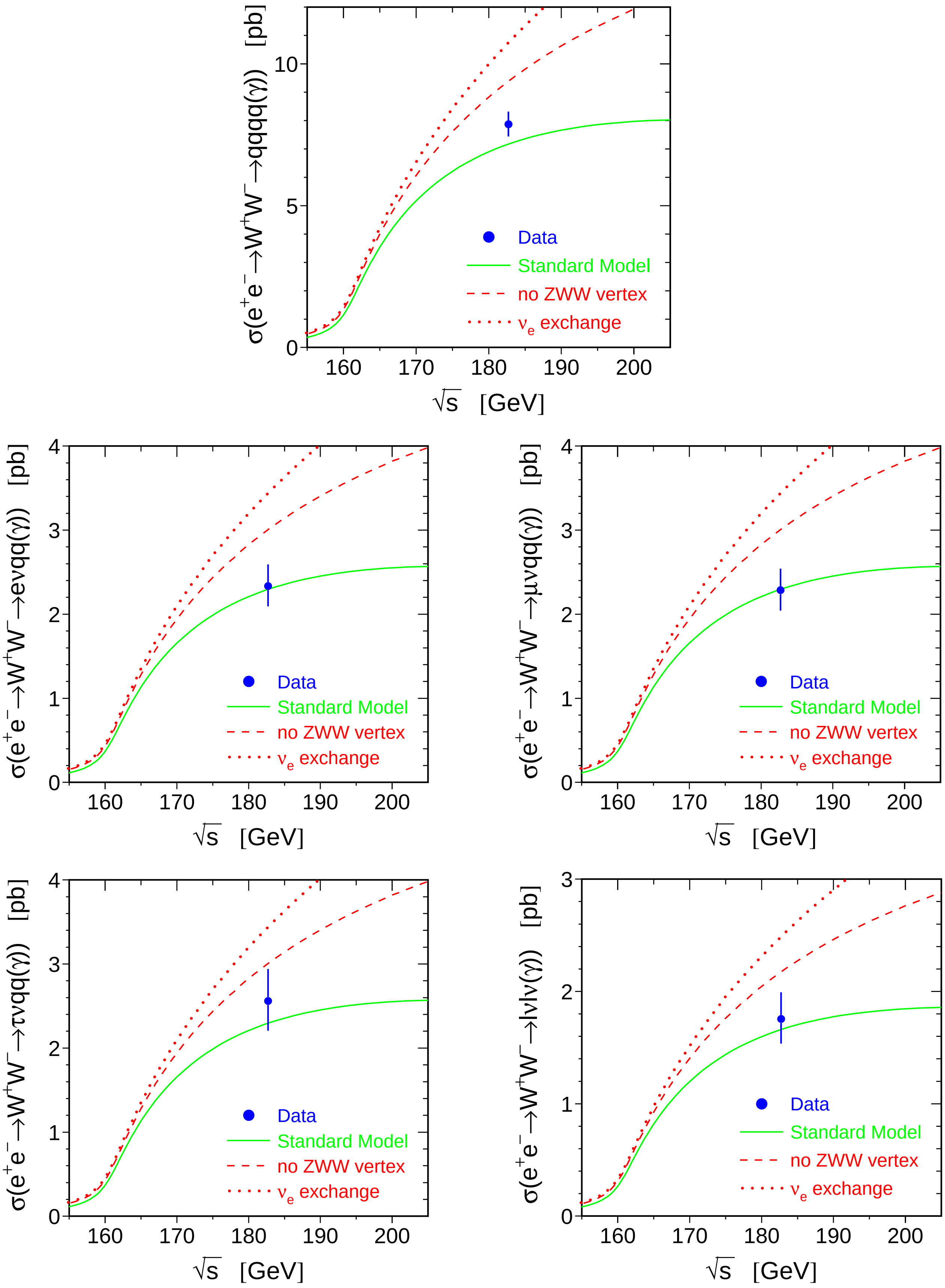

Figure 5.22: W pair production cross sections in the 5 possible final states as a function of $\sqrt{s}$; the error bars represent the statistical errors only.

Chapter 6

Systematics evaluation

6.1 Cross check studies

Before studying the effects of systematic errors to the cross section measurement, it is interesting to compare the results found in the previous chapter with the results obtained without using the multicuts method.

I have performed the cross section measurement using just one selection (the one with w=1) for each channel; thus minimizing the following likelihood function:

$$\begin{aligned} \ell &= -2 \cdot \sum_{i=1}^{5} \ln \frac{e^{-\lambda_i}\,\lambda_i^{N_i^{\rm data}}}{N_i^{\rm data}!} \\ \lambda_i &= \sum_{j=1}^{5} \varepsilon_{ij}\,\sigma_j\,\mathcal{L}\,f_j + N_i^{\rm bkg(no\_W)} \end{aligned}$$

where ε_{ij} is the selection efficiency of the channel j in the selection of the i-th channel, while all other symbols have kept the same definition as before.

The minimization of the ℓ function gives the following results:

channel	$\sigma^{\rm CC03}$ (pb)
$\mathrm{q\bar{q}q\bar{q}}$	$8.02^{+0.47}_{-0.45}$(stat.)
$\mathrm{e\bar{\nu}q\bar{q}}$	$2.32^{+0.26}_{-0.24}$(stat.)
$\mu\bar{\nu}\mathrm{q\bar{q}}$	$2.34^{+0.26}_{-0.24}$(stat.)
$\tau\bar{\nu}\mathrm{q\bar{q}}$	$2.27^{+0.39}_{-0.36}$(stat.)
$\ell^-\bar{\nu}\ell^+\nu$	$1.73^{+0.24}_{-0.22}$(stat.)

Fixing, on the other hand, the W decay widths to the Standard Model values we find:

$$\sigma_{\rm WW} = 16.73^{+0.69}_{-0.67}(\text{stat.})\ \text{pb}$$

First of all we see that these results are, as expected, in agreement with the results obtained with the multicuts method within the statistical errors. These results constitute a cross check of the multicuts results, but since they are obtained using a different sample (only the best selection is used) they cannot be used to derive a systematic error.

As we expected, they have a bigger statistical error respect to multicuts results; from their comparison we can conclude that the multicuts method itself (without considering the optimization) brings about a 5% improvement in the statistical error of a cross section measurement.

6.2 Selection systematics

In this section I will discuss the effects related to a particular choice of the w weight factors, that is the number of selections used to construct the WLIKE function; moreover the effects due to the criteria used for lepton isolation and identification, possible different energy and angular resolutions and a possible jet energy shift between data and Monte Carlo will be taken into account.

To understand the effect of the particular choice of the w weight factors in the multicuts method, that I will improperly call "binning effect", I have constructed for each channel several WLIKE distributions changing the number of selections used and slightly moving the cuts of the "innermost" selections, that is all the selections but the tightest and the largest one. I want to remark that when I change the cuts of an innermost selection, the total number of events in the WLIKE distribution does not change, we only have a migration of events from one bin to another.

For each set of WLIKE distributions I have performed the fit and extracted a cross section measurement. The ideal would be to do a large number of such changes and relative fits, and then to obtain the systematic error as the standard deviation of the results distribution. However, since each step takes a lot of time and work, I have performed it only five times and I have estimated the systematic error from the spread of the results. The systematic estimations due to this effect are (see also tab. 6.1):

Source	$\sigma_{\mathrm{q\bar{q}q\bar{q}}}$	$\sigma_{\mathrm{e\bar{\nu}q\bar{q}}}$	$\sigma_{\mu\bar{\nu}\mathrm{q\bar{q}}}$	$\sigma_{\tau\bar{\nu}\mathrm{q\bar{q}}}$	$\sigma_{\ell^-\bar{\nu}\ell^+\nu}$	σ_{WW}
binning & cuts	1.4%	0.2%	0.3%	1.0%	0.9%	0.8%

This reshuffle of events inside bins takes into account the effect of a particular choice of cuts for each selection, but there are some preselection cuts that are not moved in such way; these are the electron and muon isolation and identification cuts (I note that the tau isolation cuts are moved in the optimization procedure).

Therefore I have loosened and tightened each electron and muon isolation cut (described in Appendix B.1 and B.2) by 20% and I have considered the change in the cross section results as a systematic error:

Source	$\sigma_{\mathrm{q\bar{q}q\bar{q}}}$	$\sigma_{\mathrm{e\bar{\nu}q\bar{q}}}$	$\sigma_{\mu\bar{\nu}\mathrm{q\bar{q}}}$	$\sigma_{\tau\bar{\nu}\mathrm{q\bar{q}}}$	$\sigma_{\ell^-\bar{\nu}\ell^+\nu}$	σ_{WW}
isolation cuts	—	0.09%	0.04%	1.1%	—	0.1%

Looking at several high statistic distributions for each studied channel I have not seen any particular systematic disagreement between data and Monte Carlo except for the N_{ASRC} variable, but all my cuts on such a variable are in a safe region (at low values) where the agreement is excellent.

However to be conservative I have studied the effect of a smearing of energy and angular coordinates both for jets than for leptons, and the effect of a possible shift of jet energies between data and Monte Carlo.

Supposing that the resolution of some Monte Carlo variables is over-estimated I have smeared[1] the MC jet and tau energy by 10% and their angular coordinate by 0.04 rad, while I have smeared the electron and muon energy by 1% and their polar coordinate by 0.009 rad, and the azimuthal coordinate by 0.003 rad (see sec. 3.4). Moreover I have shifted the jet energies by ±2% of their value. The effects of such changes are:

Source	$\sigma_{\mathrm{q\bar{q}q\bar{q}}}$	$\sigma_{\mathrm{e\bar{\nu}q\bar{q}}}$	$\sigma_{\mu\bar{\nu}\mathrm{q\bar{q}}}$	$\sigma_{\tau\bar{\nu}\mathrm{q\bar{q}}}$	$\sigma_{\ell^-\bar{\nu}\ell^+\nu}$	σ_{WW}
smearing & shift	0.3%	1.2%	2.0%	2.1%	—	0.3%

6.3 MC statistics

Since the number of simulated MC signal and background events is finite, we must take into account of the error due to the use of a finite sample of simulated events. In other words each MC bin in each WLIKE distribution has an error that can be evaluated using the Poisson statistics in the following way: the MC content of each bin is replaced by a random number, generated according to a Poisson distribution whose mean is equal to the not-normalized bin content, and then the fit is performed to find the cross section. This procedure is repeated 1000 times, thus producing 1000 results both for each channel cross section than for the total cross section.

Such 1000 cross section measurements are fitted with a gaussian (see fig. 6.1 for the total cross section distribution) and the standard deviation of the gaussian is assumed as systematic error:

Source	$\sigma_{\mathrm{q\bar{q}q\bar{q}}}$	$\sigma_{\mathrm{e\bar{\nu}q\bar{q}}}$	$\sigma_{\mu\bar{\nu}\mathrm{q\bar{q}}}$	$\sigma_{\tau\bar{\nu}\mathrm{q\bar{q}}}$	$\sigma_{\ell^-\bar{\nu}\ell^+\nu}$	σ_{WW}
MC statistics	0.4%	0.7%	0.7%	1.1%	2.1%	0.3%

6.4 Background studies

6.4.1 $\mathrm{q\bar{q}}(\gamma)$ background

Since the $\mathrm{q\bar{q}}(\gamma)$ process constitutes the main background for almost all the W channels, I have selected a sample of $\mathrm{q\bar{q}}(\gamma)$ events and I have compared some distributions (fig. 6.2) with the expected MC ones. The cuts used for the selection are described in Appendix

---

[1] To smear a variable of x% means multiply such a variable for a random number generated according to the normal distribution with a standard deviation equal to x.

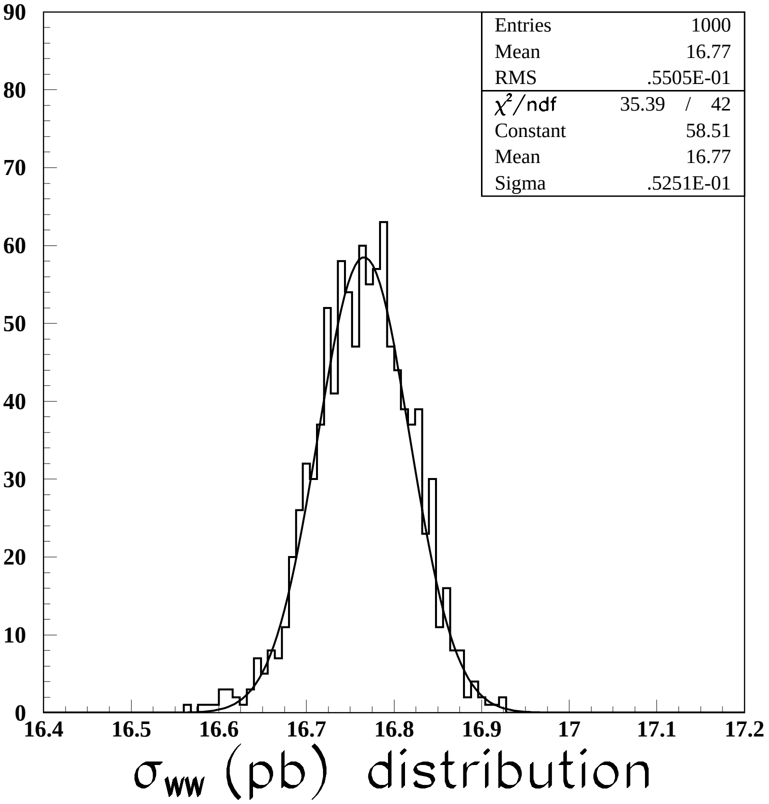

Figure 6.1: Distribution of the 1000 fit results obtained replacing the bin contents with different Poisson generated random numbers.

C. As in sec. 5.2 I have to reduce by hand the $\gamma\gamma$ background generated with PHOJET by a factor 1.7 in order to have agreement with data. Such a factor is different from the factor used in sec. 5.2 because the selection is different; the reason why we have to apply a different factor for each different selection is that such a factor depends on the Q^2 of the emitted photons; otherwise the problem would be simply solved by rescaling the PHOJET cross section once and for all.

Once the $\gamma\gamma$ background has been corrected the results for some variables are shown in fig. 6.2. These distributions show an overall agreement in their shape; maybe only a small shift in the visible energy between data and Monte Carlo is present, but this effect has already been taken into account in the systematic error evaluation by shifting the MC jet energies respect to data.

6.4.2 $\gamma\gamma$ hadronic background

We know from sec. 5.2 and from the previous section that the normalization of the $\gamma\gamma$ background in the WLIKE distributions is wrong, but we do not know the correction factor it should be multiplied since, as we have seen, the correction factor changes from selection to selection. Fortunately this has not a big effect on our results because only a few $\gamma\gamma$ events pass the W selections.

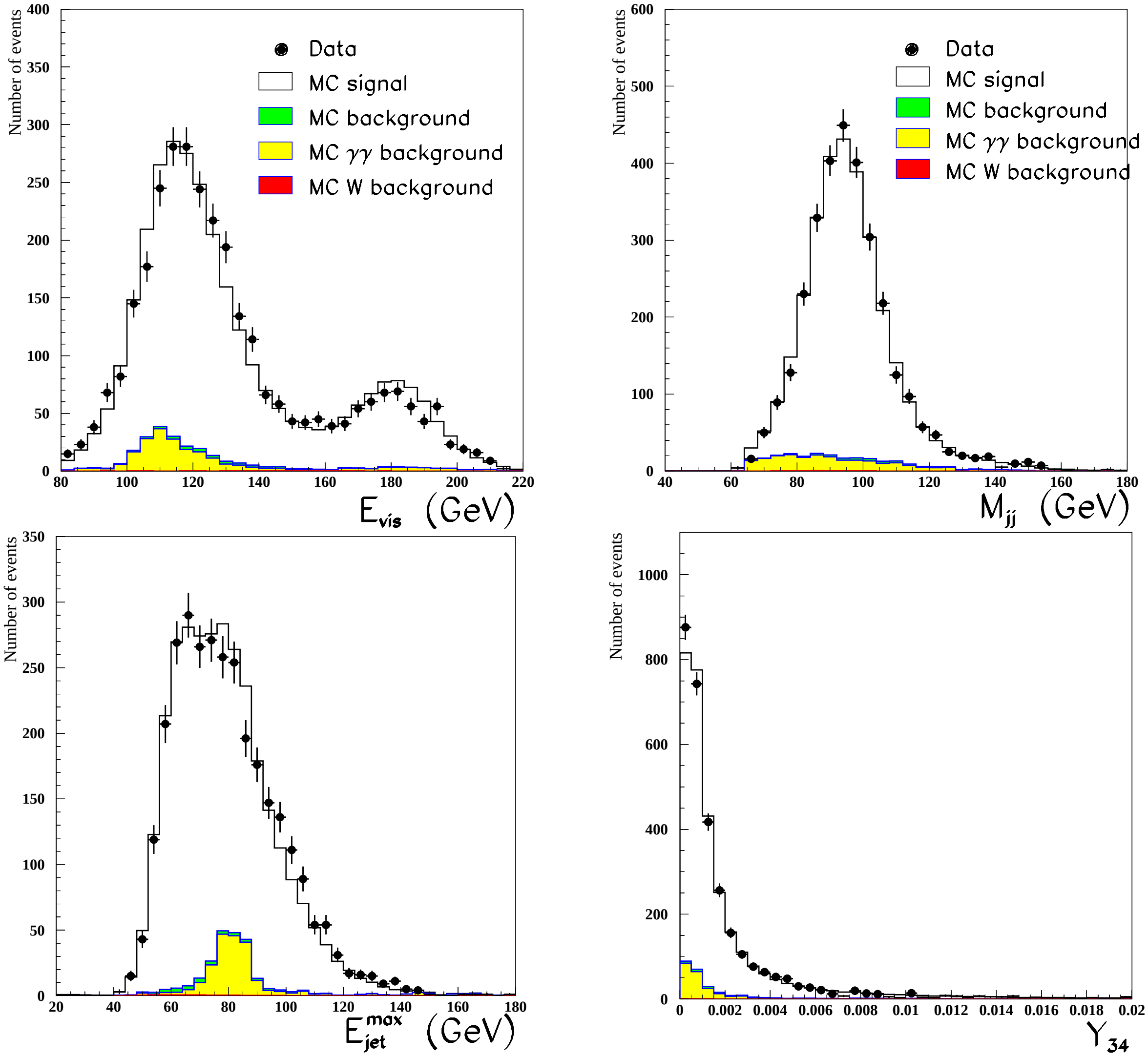

Figure 6.2: Distribution of the visible energy, the jet-jet invariant mass, the energy of the most energetic jet and y_{34} for a sample of selected $q\bar{q}(\gamma)$ events.

In order to be conservative I have multiplied and divided the $\gamma\gamma$ contribution by a factor 5 and I have re-computed the cross sections; the differences are taken as systematic errors:

Source	$\sigma_{q\bar{q}q\bar{q}}$	$\sigma_{e\bar{\nu}q\bar{q}}$	$\sigma_{\mu\bar{\nu}q\bar{q}}$	$\sigma_{\tau\bar{\nu}q\bar{q}}$	$\sigma_{\ell^-\bar{\nu}\ell^+\nu}$	σ_{WW}
$\gamma\gamma$ background	0.3%	0.6%	—	1.4%	—	0.4%

6.4.3 4f background

As explained in sec. 2.1.6 there are two ways one can subtract the contribution of 4f diagrams different from CC03 from the number of observed events: the additive and the multiplicative approach. I have used the multiplicative approach to find the results and therefore I use the additive approach as a cross check; moreover I take the difference of the results as an estimation of the systematic error related to such procedure.

Using the additive approach I find:

channel	σ^{CC03} (pb)
$\mathrm{q\bar{q}q\bar{q}}$	$7.87^{+0.45}_{-0.43}$(stat.)
$\mathrm{e}\bar{\nu}\mathrm{q\bar{q}}$	$2.33^{+0.25}_{-0.23}$(stat.)
$\mu\bar{\nu}\mathrm{q\bar{q}}$	$2.28^{+0.26}_{-0.24}$(stat.)
$\tau\bar{\nu}\mathrm{q\bar{q}}$	$2.56^{+0.38}_{-0.35}$(stat.)
$\ell^-\bar{\nu}\ell^+\nu$	$1.77^{+0.27}_{-0.25}$(stat.)

Fixing, on the other hand, the W decay widths to the Standard Model values we find:

$$\sigma_{\mathrm{WW}} = 16.76^{+0.66}_{-0.64}(\text{stat.})\ \text{pb}$$

All such results are in excellent agreement with the results obtained with the multiplicative approach in sec. 5.7.

Source	$\sigma_{\mathrm{q\bar{q}q\bar{q}}}$	$\sigma_{\mathrm{e}\bar{\nu}\mathrm{q\bar{q}}}$	$\sigma_{\mu\bar{\nu}\mathrm{q\bar{q}}}$	$\sigma_{\tau\bar{\nu}\mathrm{q\bar{q}}}$	$\sigma_{\ell^-\bar{\nu}\ell^+\nu}$	σ_{WW}
4f background	—	0.1%	—	—	0.7%	0.01%

6.5 Other effects

The integrated luminosity measurement has an error of 0.3% (see sec. 1.2.7); the effect of such error on the cross sections measurement has been evaluated by changing the $\mathcal{L}$ value of ±0.3% in the fit procedure and it is reported in tab. 6.1.

Other contributions to the systematic error coming from effects related to the simulation of initial and final state radiation, Bose-Einstein and colour reconnection effects and a shift of the W mass and width, have not been studied in the work for this thesis, but their contribution is taken from [69] since it comes from Monte Carlo studies and does not depend on the details of the selections.

6.6 Final results

Tab. 6.1 summaries the contributions of the different sources to the systematic error in the cross section measurement.

Systematic errors						
Source	$\sigma_{\mathrm{q\bar{q}q\bar{q}}}$	$\sigma_{\mathrm{e}\bar{\nu}\mathrm{q\bar{q}}}$	$\sigma_{\mu\bar{\nu}\mathrm{q\bar{q}}}$	$\sigma_{\tau\bar{\nu}\mathrm{q\bar{q}}}$	$\sigma_{\ell^-\bar{\nu}\ell^+\nu}$	σ_{WW}
binning & cuts	1.4%	0.2%	0.3%	1.0%	0.9%	0.8%
isolation cuts	—	0.09%	0.04%	1.1%	—	0.1%
smearing & shift	0.3%	1.2%	2.0%	2.1%	—	0.3%
MC statistics	0.4%	0.7%	0.7%	1.1%	2.1%	0.3%
$\gamma\gamma$ background	0.3%	0.6%	—	1.4%	—	0.4%
4f background	—	0.1%	—	—	0.7%	0.01%
Luminosity	0.4%	0.3%	0.3%	0.4%	0.4%	0.4%
Other effects	2.0%	1.0%	0.9%	1.3%	0.8%	1.0%
Total	2.5%	1.8%	2.3%	3.4%	2.5%	1.5%

Table 6.1: Summary of the contributions to the systematic error in the cross section measurement.

Tab. 6.2 shows the partial cross sections with statistic and systematic errors, compared to the Standard Model expectations.

channel	$\sigma^{\mathrm{CC03}}_{\mathrm{measured}}$ (pb)	$\sigma^{\mathrm{CC03}}_{\mathrm{SM}}$ (pb)
$\mathrm{q\bar{q}q\bar{q}}$	$7.87^{+0.45}_{-0.43}(\text{stat.}) \pm 0.20(\text{syst.})$	7.17
$\mathrm{e}\bar{\nu}\mathrm{q\bar{q}}$	$2.33^{+0.26}_{-0.24}(\text{stat.}) \pm 0.04(\text{syst.})$	2.30
$\mu\bar{\nu}\mathrm{q\bar{q}}$	$2.28^{+0.26}_{-0.24}(\text{stat.}) \pm 0.05(\text{syst.})$	2.30
$\tau\bar{\nu}\mathrm{q\bar{q}}$	$2.56^{+0.38}_{-0.35}(\text{stat.}) \pm 0.09(\text{syst.})$	2.30
$\ell^-\bar{\nu}\ell^+\nu$	$1.75^{+0.24}_{-0.22}(\text{stat.}) \pm 0.04(\text{syst.})$	1.67

Table 6.2: Final results of the W pair production cross sections for the different final states, compared to the Standard Model expectations.

Fixing the W decay widths to the Standard Model values we find (see also fig. 6.3):

$$\boxed{\sigma_{\mathrm{WW}} \quad = \quad 16.76^{+0.66}_{-0.64}(\text{stat.}) \pm 0.25(\text{syst.})\ \text{pb}}$$

to be compared to the Standard Model predicted value $\sigma^{\mathrm{teor}}_{\mathrm{WW}} = 15.72$ pb.

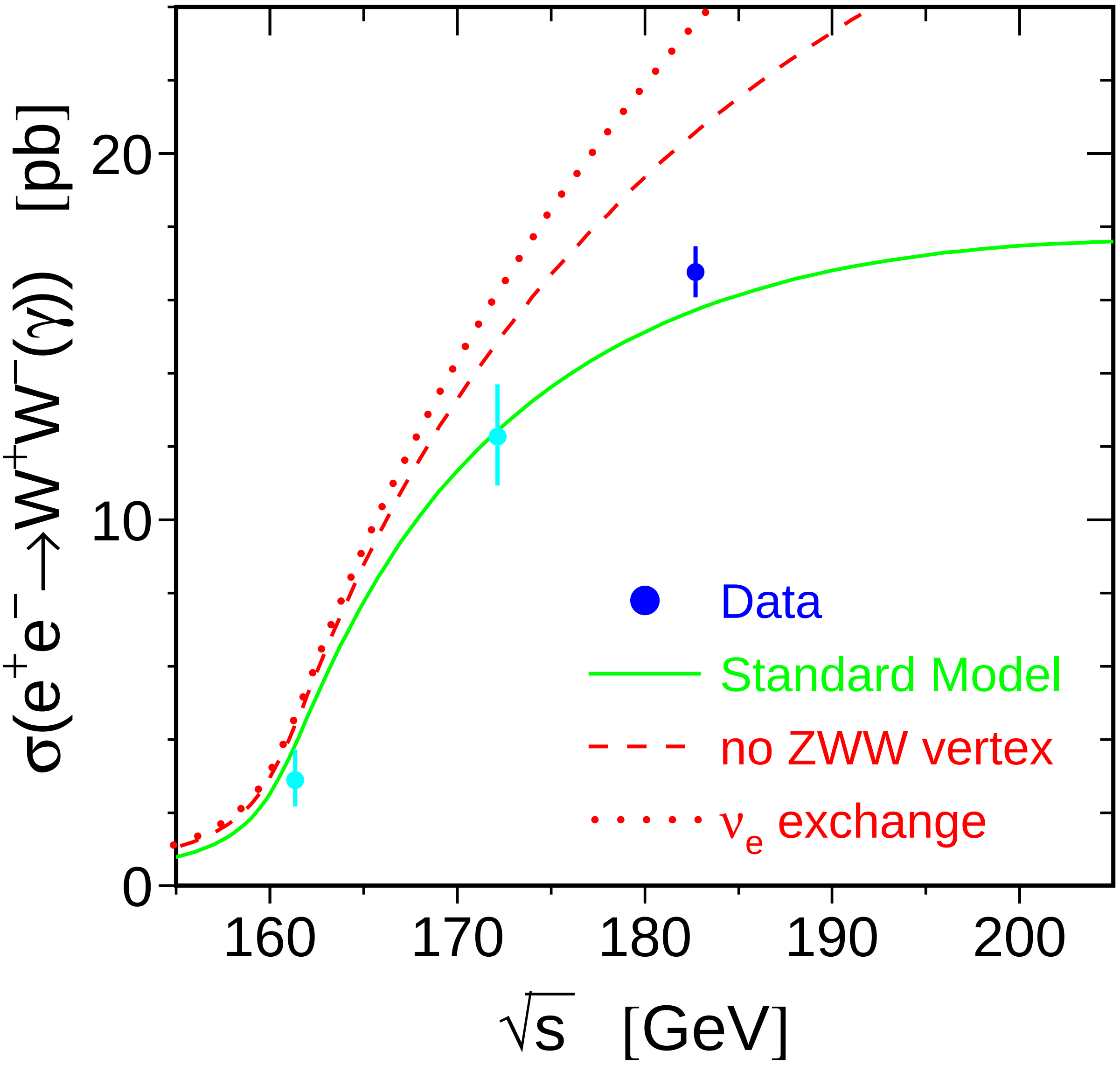

Figure 6.3: W pair production cross section as a function of $\sqrt{s}$; the solid curve shows the Standard Model expectation, the dashed curve shows the expectations if there is no ZWW coupling, the dotted curve shows the expectation if only t-channel ν_e exchange in W pair production is considered; the bar errors represent the statistical and systematic errors added in quadrature. The points at $\sqrt{s} = 161$ GeV and $\sqrt{s} = 172$ GeV are the L3 published measurement [67], [68].

6.6.1 Other experiment results

In order to have a global vision of the results obtained at LEP and to derive future previsions, it is worth to summarize the cross section measurements performed by all the LEP experiments for the data collected in 1997:

experiment	$\sigma_{\mathrm{WW}}^{\mathrm{CC03}}$ (pb)
ALEPH	$15.51 \pm 0.61(\mathrm{stat.}) \pm 0.36(\mathrm{syst.})$
DELPHI	$16.01 \pm 0.71(\mathrm{stat.}) \pm 0.43(\mathrm{syst.})$
L3	$16.53 \pm 0.67(\mathrm{stat.}) \pm 0.26(\mathrm{syst.})$
OPAL	$15.52 \pm 0.62(\mathrm{stat.}) \pm 0.35(\mathrm{syst.})$

From these results we can see that the amount of data collected in 97 allows a cross section measurement with a statistical error about twice the size of the systematic one; we can therefore deduce that in order to have a statistical error comparable with the systematic one we need to quadruple the collected integrated luminosity.

In 1998 an integrated luminosity of about 180 pb^{-1} per experiment was collected; this will allow to almost halve the statistical error; however the limits on the integrated luminosity to be collected are in reality determined by the precision requirement on the measurement of the W mass (30 MeV total error). Such a precise measurement will allow the comparison between the direct W mass measurement and the indirect measurement coming from a global fit to all the electroweak measurements performed at LEP. Since the indirect measurement is strongly dependent on electroweak corrections, a precise direct W mass measurement will accurately precisely verify the Standard Model predictions. The LEP combined W mass measurement has a statistical error of about 90 MeV considering all data collected up to 1997, and to achieve the aforesaid goal we need about nine times such a statistics ($\sim$ 500 pb^{-1} per experiment), which will be provided by LEP in the next couple of years.

Conclusions

In the work for this thesis the data collected by the L3 experiment in 1997 at a centre of mass energy of 183 GeV, corresponding to a total integrated luminosity of 55.5 pb^{-1}, have been analysed and the total and partial W-pair-production cross sections have been measured. The following results, compared to the Standard Model expectations, are found:

channel	$\sigma^{\mathrm{CC03}}_{\mathrm{measured}}$ (pb)	$\sigma^{\mathrm{CC03}}_{\mathrm{SM}}$ (pb)
$\mathrm{q\bar{q}q\bar{q}}$	$7.87^{+0.45}_{-0.43}(\mathrm{stat.}) \pm 0.20(\mathrm{syst.})$	7.17
$\mathrm{e}\bar{\nu}\mathrm{q\bar{q}}$	$2.33^{+0.26}_{-0.24}(\mathrm{stat.}) \pm 0.04(\mathrm{syst.})$	2.30
$\mu\bar{\nu}\mathrm{q\bar{q}}$	$2.28^{+0.26}_{-0.24}(\mathrm{stat.}) \pm 0.05(\mathrm{syst.})$	2.30
$\tau\bar{\nu}\mathrm{q\bar{q}}$	$2.56^{+0.38}_{-0.35}(\mathrm{stat.}) \pm 0.09(\mathrm{syst.})$	2.30
$\ell^-\bar{\nu}\ell^+\nu$	$1.75^{+0.24}_{-0.22}(\mathrm{stat.}) \pm 0.04(\mathrm{syst.})$	1.67

	measured	SM
σ_{WW}	$16.76^{+0.66}_{-0.64}(\mathrm{stat.}) \pm 0.25(\mathrm{syst.})$ pb	15.72 pb

The comparison of the measured W-pair-production cross section with the theoretical predictions with and without the three boson vertices (ZWW and γWW) diagrams (fig. 6.3) constitutes a direct evidence of bosonic self-interactions, which are a characteristic signature of the Standard Model non-abelian nature.

These results have been obtained using a new analysis method, called “multi-cuts optimized method”, that I have developed and tested in the work for this thesis.

In these last years several techniques have been developed and used in order to extract the maximum informations from a sample of data, I refer to multivariate techniques like neural networks or discriminator functions trained on Monte Carlo samples and used to better discriminate signal from background.

The multi-cuts optimized method makes use of traditional cuts on variable distributions, but has about the same performance of a neural network analysis. The method consists mainly of two parts; first an automized procedure that chooses the best variables to be used in a selection and the value of the cuts that have to be applied on them has been developed. This procedure finds the selection criteria that better discriminate signal from background so as to have a cross section measurement with the lowest statistical error. The second part of the method consists in selecting several optimized selections with a different degree of efficiency for each different W pair final state, which are then used through a global likelihood fit to extract the cross section.

Comparing the shown results with the ones obtained using single optimized selections I have found that the multicuts method alone (without taking into account the optimization of the selections) brings an improvement of about 5% in the statistical error of a cross section measurement without increasing the systematic error. Indeed the use of several selections for each W decay channel, instead of a single selection, makes the results less sensitive to possible systematic effects.

The optimization procedure itself further improves the statistical error obtained, although in a not easily quantifiable way; moreover it also reduces considerably the time needed to efficiently select events from the data.

Appendix A

A.1 Electron and photon identification in BGO

In the BGO, we look for ASRCs that satisfy the following criteria:

- Bump energy greater than 1 GeV;
- $\sum_9 / \sum_{25}$ greater than 0.93;
- the ratio between the HCAL and the BGO contribution to the ASRC energy less than 0.2.

For the matching of a track with a bump we require that the track fulfils the following requests:

- transverse momentum $p_\mathrm{T}^\mathrm{track} \geq 100$ MeV;
- momentum $p^\mathrm{track} \geq 500$ MeV;
- DCA ≤ 10 mm;
- TEC hits number $N_\mathrm{hits} \geq 5$;
- $|\varphi_\mathrm{BGO} - \varphi_\mathrm{TEC}| \leq 0.05$ rad, where φ_BGO and φ_TEC are respectively the BGO bump and TEC track azimuthal angles (φ_TEC takes into account the curvature of the track due to the magnetic field and therefore represents the φ of the impact point of the track on the BGO surface);
- the criteria regarding the ϑ_BGO and ϑ_TEC BGO bump and TEC track polar angles matching depend on the resolution of the ϑ_TEC measurement and are summarized in the following table:

SMD hits	TEC Z hits	flange inform.	selection criterion
x	x	o	$\|\vartheta_{\rm BGO} - \vartheta_{\rm TEC}\| \leq 0.05$ rad
x	o	o	$\|\vartheta_{\rm BGO} - \vartheta_{\rm TEC}\| \leq 0.1$ rad
x	o	x	$\|\vartheta_{\rm BGO} - \vartheta_{\rm TEC}\| \leq 0.1$ rad
o	x	o	$\|\vartheta_{\rm BGO} - \vartheta_{\rm TEC}\| \leq 0.2$ rad
o	o	x	$\|\vartheta_{\rm BGO} - \vartheta_{\rm TEC}\| \leq 0.2$ rad
o	o	o	$\|N_{\rm hits}^{\rm expected}(\vartheta_{\rm BGO}) - N_{\rm hits}\| < 5$

As mentioned in sec. 3.2 the ϑ track can be extracted from the hit SMD strips, from hit TEC wires, from the flange informations, or from their combination. The “x” symbol is for used information, the “o” for not used; $N_{\rm hits}^{\rm expected}(\vartheta_{\rm BGO})$ is the expected number of TEC hits as a function of $\vartheta_{\rm BGO}$;

- if $N_{\rm hits} \geq 30$ and $({\rm E} \cdot \sin\vartheta)_{\rm ASRC} \geq 5$ GeV and $p_{\rm T}^{\rm track} \leq 1$ GeV I reject the event; this drops events where a weak track is matched to an ASRC with a high transverse energy $({\rm E} \cdot \sin\vartheta)_{\rm ASRC}$.

If in a $\Delta\varphi$ window of 10 mrad around the bump there are more than 1 track, it is important to match the bump with the most likely right track if we want to use the track variables for the subsequent event selection. I cannot simply take the one with lowest $\Delta\varphi$ because there are events with an energetic bump and whose nearest track in φ has a very low momentum, while the second nearest track has a momentum of the same order of the bump energy. In most of these events the weak near track belongs to a jet, but has a badly reconstructed ϑ.

Moreover the informations of the second track are equally important to allow the identification of photon conversion events, that is events where an original photon, after having interacted with the beam pipe or other detector materials produces two collinear electrons that are seen in the electromagnetic calorimeter as an only bump.

For this purpose if the bump energy is greater than 5 GeV and there are more than 1 track in $\Delta\varphi = 10$ mrad I sort the tracks following these 3 possibilities:

1. if there are at least two tracks with momentum greater than 5 GeV I sort the tracks in order of their energy, the first being the one that is matched to the bump;
2. if just one track has a momentum greater than 5 GeV, I take this as the one to match to the bump, and I leave as second chance the one with lower $\Delta\varphi$;
3. if all tracks have a momentum lower than 5 GeV, I sort them $\Delta\varphi$ wise.

The informations relative to the first two tracks are stored together with the calorimetric informations and are used at the event selection level. At this preselection level we require that $|\varphi_{BGO} - \varphi_{TEC}| \leq 0.05$ rad; however electrons at low polar angle ($\vartheta \leq 15°$), that cannot have a TEC track, are labelled as photons.

Moreover we ask that the electron-photon is “isolated” from the hadronic jets. If the bump energy is lower than 10 GeV or if it has no matched track I use tighter isolation cuts; on the other hand the isolation cuts are loosened for electrons with an energy greater than 10 GeV so as not to lose good events at the preselection level. The isolation criteria are[2]:

- number of charged tracks in a 20° half-cone around the electron-photon direction less than 7 (9);
- number of calorimetric clusters in a 20° half-cone around the electron-photon direction less than 7 (13);
- calorimetric energy in a 10° half-cone around the electron-photon direction less than 5 GeV (15 GeV);
- ratio between the calorimetric energy in a 10° half-cone and the electron-photon energy less than 0.2 (0.4).

A.2 Electron and photon identification in EGAP

For each EGAP cluster, the raw energy is corrected for the energy loss on its border and the energy deposited on the surrounding BGO and HCAL; then we require that such corrected energy, $E^{\mathrm{corr}}_{\mathrm{EGAP}}$, is greater than 10 GeV, and that the initial EGAP cluster energy, $E^{\mathrm{raw}}_{\mathrm{EGAP}}$, is greater than $0.5 \cdot E^{\mathrm{corr}}_{\mathrm{EGAP}}$.

The electromagneticity of the cluster can be inferred by the following parameter:

$$\rho = \frac{E^{20^\circ}_{\mathrm{HCAL}}}{E^{\mathrm{raw}}_{\mathrm{EGAP}} + E^{20^\circ}_{\mathrm{BGO}} + E^{20^\circ}_{\mathrm{HCAL}}}$$

where $E^{20^\circ}_{\mathrm{HCAL}}$ and $E^{20^\circ}_{\mathrm{BGO}}$ are the energy deposited, respectively, in the HCAL and BGO in a 20° cone around the EGAP cluster; an electromagnetic particle delivers almost entirely its energy in the EGAP while a hadronic particle is more penetrating and produces a larger shower, therefore we accept events as electron-photon candidate only if $\rho \leq 0.2$. Finally we impose isolation requiring that the number of calorimeter clusters in a 20° half-cone around the direction of the electron-photon is less than 3 and the number of charged tracks in a 20° half-cone around the direction of the electron-photon is less than 4.

This electromagnetic cluster is then labelled as an electron if there is a track that fulfils the following requests:

- momentum greater than 0.5 GeV;
- DCA $\leq$ 10 mm;
- $N_{\mathrm{hits}} \geq 10$

---

[2] The numbers in parenthesis represent the loosened cuts.

- $|\vartheta_{\mathrm{EGAP}} - \vartheta_{\mathrm{TEC}}| < 0.1$ rad or $|N^{\mathrm{expected}}_{\mathrm{hits}}(\vartheta_{\mathrm{EGAP}}) - N_{\mathrm{hits}}| < 5$, where $\vartheta_{\mathrm{EGAP}}$ is the polar angle of the EGAP cluster;
- $|\varphi_{\mathrm{EGAP}} - \varphi_{\mathrm{TEC}}| < 0.1$ rad, where φ_{EGAP} is the azimuthal angle of the EGAP cluster.

A.3 Muon identification criteria

For each reconstructed AMUI, defined in section 3.2, in the barrel region we reject AMUI with only 1 P segment; also depending on the muon momentum we apply looser or tighter cuts as in the electron case; this is to avoid having on one hand too many low energy muons while on the other hand trying to keep as many energetic muons as possible. If the muon momentum is lower (greater) than 15 GeV we ask that the DCA is lower than 10 (15) mm, lower than 6 (9) standard deviation in the r-φ plane and 7 (10) standard deviation in the r-z plane.

We besides require that the muon is enough isolated from hadronic jets through the following cuts:

- number of charged tracks in a 20° half-cone around the muon direction less than 3 (7);
- number of calorimetric clusters contained between a 5° and a 20° half-cone around the muon direction less than 4 (10);
- calorimetric energy contained between a 5° and a 10° half-cone around the muon direction less than 5 (15) GeV.

To avoid that a TEC track produced by a muon will be subsequently used for reconstructing another lepton, the track is dropped from the event. If the AMUI has been reconstructed using also some TEC hits, I drop the corresponding track. In case there are no used TEC tracks I match the muon track with the nearest TEC track that satisfy the following conditions:

- transverse momentum greater than 0.5 GeV;
- DCA ≤ 10 mm;
- $N_{\mathrm{hits}} \geq 10$;
- same $\Delta\vartheta$ matching as for electron case;
- $|\varphi_{\mathrm{track}} - \varphi_{\mathrm{AMUI}}| \leq 0.1$ rad.

A.4 MIP identification criteria

For the MIP calorimetric cluster we require either a bump with at least 8 crystals and an energy between 150 MeV and 1 GeV, or a hadronic cluster with energy between 1

GeV and 6 GeV; in this second case we also require that the hits number of the hadronic cluster is greater than 60% of the hits number expected from an ideal MIP.

The matched track has to fulfil the following requests:

- track momentum greater than 8 GeV;
- DCA $\geq$ 20 mm;
- same $\Delta\vartheta$ matching as for the electron case;
- $|\varphi_{\mathrm{track}} - \varphi_{\mathrm{MIP}}| \leq 0.05$ rad.

A.5 Tau identification criteria

The criteria used to identify and isolate taus with hadronic decay are:

- τ energy greater than 2 GeV
- number of clusters in 10° half-cone around the direction of the τ between 1 and 8
- no track between a 10° and 30° half-cone around the τ direction;
- number of calorimetric clusters between a 10° and 30° half-cone around the τ direction less than 6;
- calorimetric energy contained in a 10° and 30° half-cone around the τ direction less than the τ energy.

Appendix B

B.1 Electron identification criteria in $\mathrm{e}\bar{\nu}\mathrm{q}\bar{\mathrm{q}}$ selection

The electron in BGO selection criteria obtained after the first steps optimization are:

- if the bump has a $\vartheta, \pi - \vartheta > 46.6^\circ$ then the matching bump-track has to fulfil $|\varphi_{\mathrm{BGO}} - \varphi_{\mathrm{track}}| \leq 0.019$ rad;
- if $26.6^\circ < \vartheta, \pi - \vartheta < 46.6^\circ$ the matching bump-track has to fulfil $|\varphi_{\mathrm{BGO}} - \varphi_{\mathrm{track}}| \leq 0.026$ rad;
- for bump with $\vartheta, \pi - \vartheta < 26.6^\circ$ I do not ask anymore the matching with a track, because of the low TEC efficiency at low polar angles, but I require that the sum of the 3 space angle between jet-jet and jet-electron is less than 6.28 (this sum equalizes 2π for $\mathrm{q}\bar{\mathrm{q}}(\gamma)$ events);
- in order to reject converted electrons, that is electron pairs produced by the interaction of a photon with the beam pipe or some detector, I reject bumps with the second nearest matched track within 17 mrad in φ and a momentum greater than 10 GeV;

Moreover the following isolation criteria are requested:

- a calorimetric energy in a 15° half-cone around the direction of the electron less than 15.2% the electron energy;
- an angle between the electron an the nearest jet grater than 11.2°.

The electron in EGAP selection criteria obtained after the first step optimization are:

- $|\varphi_{\mathrm{EGAP}} - \varphi_{\mathrm{track}}| \leq 0.05$ rad;
- minimum angle between electron and jet direction greater 17.2°;
- momentum of the matched track greater than 20 GeV;
- calorimetric energy in a 20° half-cone around the electron direction less than 20% the electron energy;
- number of tracks in a 20° half-cone around the electron direction less than 5.

B.2 Muon identification criteria in $\mu\bar{\nu}q\bar{q}$ selection

An AMUI is identified as a muon if:

- the sum of the energy deposited in the BGO and in the HCAL in a 7° cone around the direction of the muon is less than 30 GeV;
- the number of calorimetric clusters between a 5° and a 20° half-cone around the direction of the muon is less than 9;
- the angle between the muon and the nearest reconstructed jet is less than 0.12 rad.

The MIP selection has to fulfil the following requests:

- the MIP must have a calorimetric energy between 0.5 GeV and 6 GeV or an energy in the BGO between 0.25 GeV and 1 GeV with a maximum of 5 BGO crystals fired;
- number of tracks in a 10° half-cone around the muon direction less than 2;
- number of calorimetric clusters in a 10° half-cone around the muon direction less than three;
- number of tracks between a 10° and a 30° half-cone around the muon direction less than 5;
- number of calorimetric clusters between a 10° and a 30° half-cone around the muon direction less than 5;
- angle between the MIP direction and the nearest jet greater than 0.28 rad.

Appendix C

Selection cuts for $q\bar{q}(\gamma)$ events

In order to select a sample of $q\bar{q}(\gamma)$ events I have first applied the following set of general cuts:

- visible energy between 80 GeV and 220 GeV;
- $N_{\text{track}} \geq 5$;
- $N_{\text{ASRC}} \geq 15$;
- $E_{\text{miss}} \cdot |\cos\vartheta_{\text{miss}}| \leq 0.8 \cdot E_{\text{vis}}$

For the selection of $q\bar{q}(\gamma)$ events where the emitted photon is detected I require:

- one isolated photon with an energy greater than 50 GeV;
- minimum angle between photon and jet greater than 0.3 rad;
- $M_{jj}^{-\gamma} > 0.7 \cdot M_{\text{Z}}$;
- $E_{\text{miss}} < 35$ GeV.

Events where the photon escapes in the beam pipe are selected by requiring:

- $E_{\text{miss}} > 35$ GeV;
- $|\cos\vartheta_{\text{miss}}| > 0.98$;
- $M_{jj} > 0.7 \cdot M_{\text{Z}}$
- jet-jet acollinearity between 1.5 rad and 2.9 rad;
- jet-jet acoplanarity greater than 3 rad.

Bibliography

[1] S.L. Glashow, Nucl. Phys. 22 (1961) 579;
S. Weinberg, Phys. Rev. lett. 19 (1967) 1264;
A. Salam, "Elementary Particle Theory", Ed. N. Svartholm, Stockholm, "Almquist and Wiksell" (1968) 367.

[2] F.J. Hasert et al., Phys. Lett. B 46 (1973) 121.

[3] F.J. Hasert et al., Phys. Lett. B 46 (1973) 138.

[4] UA1 Collaboration, G. Arnison et al., Phys. Lett. B 122 (1983) 103.

[5] UA2 Collaboration, M. Banner et al., Phys. Lett. B 122 (1983) 476.

[6] ALEPH Collaboration, D. Decamp et al., Nucl. Inst. Meth. A 294 (1990) 127.

[7] DELPHI Collaboration, P. Aarnio et al., Nucl. Inst. Meth. A 303 (1991) 233.

[8] L3 Collaboration, B. Adeva et al., Nucl. Inst. Meth. A 289 (1990) 35.

[9] OPAL Collaboration, K. Ahmet et al., Nucl. Inst. Meth. A 305 (1991) 275.

[10] The LEP Energy Working Group, "LEP energy calibration above the W pair production theshold", LEP ECAL/98-02, ICHEP-98/352.

[11] A.A Zholentz et al, Phys. Lett. B96 (1980) 214;
A.S. Artamonov et al., Phys. Lett. B 118 (1982) 225;
A.N. Skrinskii and Yu.M. Shatunov, Sov. Phys. Usp. 32(6) (1989) 548:
ARGUS Collaboration, D.P. Barber et al., Phys. Lett. B 135 (1984) 498;
CUSB Collaboration, W.W. McKay et al., Phys. Rev. D 29 (1984) 2483.

[12] L. Arnaudon et al., "The Energy Calibration of LEP in 1991", Preprint CERN-SL/92-37(DI)nand CERN PPE/92-125, CERN, 1992;
L. Arnaudon et al., "The Energy Calibration of LEP in 1992", Preprint CERN-SL/93-21(DI), CERN, 1993;
L. Arnaudon et al., "Accurate Determination of the LEP Beam Energy by Resonant Depolarization", Preprint CERN-SL/94-71(BI), CERN, 1994;
L. Assmann et al., "The Energy Calibration of LEP in 1993 Scan", Preprint CERN-SL/95-02, CERN, 1995.

[13] A. Blondel et al., “Beam Measurement At LEP2” in “Physics at LEP2”, ed. G. Altarelli, CERN Report 96-01.
The LEP Energy Working Group, “LEP Energy Calibration in 1996”, LEP Energy Group/97-01.

[14] M. Acciarri et al., “The L3 Silicon Microvertex Detector”, Preprint CERN-PPe-94-122, CERN, 1994.

[15] B. Beissel et al., Nucl. Inst. Meth. A 332 (1993) 33.

[16] A.H. Walenta, IEEE Trans. Nucl. Sci. NS-26, No. 1 (1979(73.

[17] G. Basti et al., Nucl. Inst. Meth. A 374 (1996) 293.

[18] M. Chemarin et al., Nucl. Inst. Meth. A 349 (1994) 345.

[19] M. Merk, in “XXIX Rencontre de Moriond, France”, Moriond (1994).

[20] U. Uwer, “The L3 Scintillation Counter System”, Internal Report L3 Note 1400, CERN, 1993.

[21] O. Adriani et al., Nucl. Inst. Meth. A 302 (1991) 53.

[22] P. Bagnaia et al., Nucl. Inst. Meth. A317 (1992) 463;
P. Bagnaia et al., Nucl. Inst. Meth. A324 (1993) 101.

[23] The BHLUMI version 4.03 is used.
S. Jadach et al., Comp. Phys. Comm. 70 (1992) 305;
S. Jadach et al., Phys. Lett. B 353 (1995) 349;
S. Jadach et al., Phys. Lett. B 353 (1995) 362.

[24] M. Böhm, A. Denner and W. Hollik, Nucl. Phys. B 304 (1988) 687;
F.A. Berends, R. Kleiss and W. Hollik, Nucl. Phys. B 304 (1988) 712.

[25] The L3 Collaboration, I.C. Brock et al., Nucl. Instr. and Meth. A 381 (1996) 236.

[26] The L3 Collaboration, M. Acciarri et al., “Measurement of Hadron and lepton-Pair Production at $161 < \sqrt{s} < 172$ GeV at LEP”, CER-PPE/97-52.

[27] F. James, CERN Program Library Long Writeup D506 MINUIT, CERN, 1993

[28] W. Beenakker et al.,“WW cross sections and distributions”, in Physics at LEP2, CERN Report CERN 96-01, eds G. Altarelli, T. Sjöstrand and F. Zwirner, (CERN, Geneva, 1996) Vol. 1, p. 79.

[29] W. Beenakker and A. Denner, Int. J. Mod. Phys. A9 (1994) 4837.

[30] D. Bardin, A. Leike, T. Riemann and M. Sachwitz, Rys. Lett. B206 (1988) 539.

[31] B. Bardin et al., “Semi-Analytical Approch to Four Fermion Production in e^+e^- Annihilation”. CERN-TH-7295-94 (1994).
D. Bardin et al., “GENTLE/4fan: a package of Fortran programs for the description of e^+e^- annihilation into four fermions”. DESY-ZEUTHEN-96-05 (March 1996).

[32] M. Skrzypek, S. Jadach, W. Placzek and Z. Wąs. “Monte Carlo program Koralw-1.02 for W pair production at LEP2/NLC energies with Yennie-Frautschi-Suura exponentiation”, in Comp. Phys. Comm. 94 (1996) 216.

[33] F.A. Berends, R. Pittau and R. Kleiss. “EXCALIBUR a Monte Carlo program to evaluate all four fermion processes at LEP200 and beyond”, INLO-PUB-12/94 (1994).

[34] L3 Collab., M. Acciarri et al., Z. Phys. C 62 (1994) 551-573.

[35] M. Böhm et al., Nucl. Phys. B 304 (1988) 463;
W. Beenakker, K. Kolodziej and T. Sack, Phys. Lett. B 258 (1991) 469;
W. Beenakker, F.A. Berends and T. Sack, Nucl. Phys. B 367 (1991) 287.

[36] J. Fleischer, F. Jegerlehner and M. Zralek, Z. Phys. C42 (1989) 409;
K. Kolodziej and M. Zralek, Phys. Rev. D43 (1991) 3619;
J. Fleisher, F. Jegerlehner and K. Kolodziej, Phys. Rev. D47 (1993) 830.

[37] V.C. Spanos, W.J Stirling, DTP-96-54 (1996), hep-ph/9607420

[38] E.A. Kuraev and V.S. Fadin, Sov. J. Nucl. Phys. 41 (1985) 466;
G. Altarelli and G. Martinelli, in Physics at LEP, eds. J. Ellis and R. Peccei (CERN-86-02, Geneva, 1986), Vol. 1, p. 47.

[39] F.A. Berends, R. Pittau, Ronald Kleiss, Nucl. Phys. B426 (1994) 344.

[40] D.R. Yennie, S.C. Frautschi and H. Suura, Ann. of Phys. 13 (1961) 379.

[41] E. Barberio, B. van Eijk, Z. Wąs, Comp. Phys. Comm. 79 (1994) 291.

[42] S. Jadach, W. Placzek, M. Skrzypek and B.F.L. Ward, Phys. Rev. D54 (1996) 5434.

[43] Z. Kunszt et al., “Determination of the mass of the W boson”, in Physics at LEP2, CERN Report CERN 96-01, eds G. Altarelli, T. Sjöstrand and F. Zwirner, (CERN, Geneva, 1996) Vol.1., pag. 141.

[44] T. Sjöstrand and V.A. Khoze, Z. Phys. C62 (1994) 281;
T. Sjöstrand and V.A. Khoze, Phys. Rev. Lett. 72 (1994) 28.

[45] R.M. Barnett et al., Physical Review D54 (1996) 1.

[46] T. Sjöstrand, Comp. Phys. Comm. 39 (1986) 347;
T. Sjöstrand and M. Bengtsson, Comp. Phys. Comm. 43 (1987) 367.

[47] U. Petterson, LU TP 88-5 (1988);
U. Petterson and L. Lönnblad, LU TP 88-015 (1988);
L. Lönnblad, LU TP 88-10 (1989).

[48] G. Marchesini and B.R. Weber, Nucl. Phys. B 310 (1988) 461;
G. Marchesini et al., Comp. Phys. Comm. 67 (1992) 465;
R.B. Webber, Nucl. Phys. B 330 (1990) 492.

[49] T. Sjöstrand, PYTHIA 5.7 and JETSET 7.4 Physics and Manual, Preprint CERN-TH.7112/93, CERN, 1993; revised August 1995.

[50] J.H. Field, Phys. Lett. B 323 (1994) 432;
J.H. Field and T. Riemann, Comp. Phys. Comm. 94 (1996) 53.

[51] S. Jadach and Z. Wąs, Comp. Phys. Comm. 36 (1985) 191.

[52] S. Jadach and B. Ward, Comp. Phys. Comm. 56 (1990) 351.

[53] S. Jadach et al., Comp. Phys. Comm 64 (1991) 275.

[54] F.A. Berends, P.H. Daverfeldt and R. Kleiss, Nucl. Phys. B 253 (1985) 441.

[55] R. Engel, Z. Phys. C 66 (1995) 203;
R. Engel and J. Ranft, Phys. Rev. D 54 (1996) 4244.

[56] R. Brun et al., “GEANT 3”, CERN DD/EE/84-1 (Revised), September 1987.

[57] H. Fesefeldt, RWTH Aachen Preprint PITHA 85/02 (1985).

[58] JADE Collaboration, W. Bartel et al.,Z. Phys. C33 (1986) 235;
S. Bethke, Habilitation thesis, LBL 50-208 (1987).

[59] T. Sjöstrand, Computer Physics Commun. 28 (1983) 227.

[60] S. Catani, Yu. L. Dokshitzer, M. Olsson, G. Turnock and B.R. Webber, Phys. Lett. B269 (1991) 432.

[61] A. Favara and M. Pieri, L3 Internal Note 1728, March 1995.

[62] Official program of the “New particle analysis group” of the L3 Collaboration.

[63] J.D. Bjorken and S.J. Brodsky, Phys. Rev. D1 (1970) 1416.

[64] H. Georgi and M. Machcek, Phys. Rev. Lett., 39, 1237 (1977).

[65] S. Brandt and H.D. Dahmen, Z. Physik, C1, 61 (1979).

[66] Subroutine PUJ5KF, Author: N.J. Kajaer (Delphi Collaboration).

[67] L3 Collab., M. Acciarri et al., Phys. Lett. B 398 (1997) 223.

[68] L3 Collab., M. Acciarri et al., Phys. Lett. B 407 (1997) 419.

[69] L3 Collab., M. Acciarri et al., Phys. Lett. B 436 (1998) 437.

Acknowledgements

For the work reported in this thesis I have benefitted from the help of several persons which I would like now to acknowledge.

I am grateful to Marco Pieri and Alvise Favara for having provided me with some of the software tools used in this thesis.

I wish to express my gratitude to Giovanni Passaleva who has spent a lot of his time looking at and trying to solve several problems I have met during the work for this thesis.

I also wish to thank Anna Maria Cartacci and Guy Coignet for their careful reading of this thesis and their fruitful comments.